Impedance Analysis of Narrowband Power Line Communication Channels

Von der Fakultät für Ingenieurwissenschaften
Abteilung Elektrotechnik und Informationstechnik
der Universität Duisburg-Essen

zur Erlangung des akademischen Grades

Doktor der Ingenieurwissenschaften (Dr.-Ing.)

genehmigte Dissertation

von

George Hallak
aus
Aleppo, Syrien

Gutachter: Prof. Dr. A. J. Han Vinck
Gutachter: Prof. Dr. Gerd Bumiller
Tag der mündlichen Prüfung: 05.11.2018

Abstract

Power line communication (PLC) stands for a type of communication technology that aims to exploit the power delivery network for data transmission. Since the power grid was not originally conceived for data communication purposes, the transmission line is hostile and exhibits high attenuation, various types of noise, and frequency selectivity, which are caused by the presence of branches and unmatched impedance. For the efficient design of the next generation of smart metering and PLC applications, perfect knowledge of the PLC channel is fundamental. To enhance this knowledge, the influence of the low access impedance of the power line channel on PLC systems from a telecommunications point of view is studied in this work.

Due to the increasing use of switched-mode power supplies with EMI filters inside electrical devices on the power grid, the situation of PLC transmitters has worsened and known concepts have lost their efficiency. In particular, the low access impedance at narrowband frequencies has changed the characteristics of the power line channel dramatically. As a result, the signal level permitted in the European standard EN 50065-1 cannot always be reached and the reliability of the transmission systems has deteriorated significantly.

In this thesis, we present a comprehensive overview of PLC channel access impedance. First, we investigate the effects of low access impedance on narrowband-PLC applications with limited power consumption in terms of the achievable data rate. We show that the performance of the transmission system has been reduced for different access impedance scenarios.

Then we develop an accurate access impedance measurement system in the frequency range of 30- 500 kHz to analyze the impedance behavior with respect to time and frequency. In this context, we carried out experimental impedance measurement campaigns on different power outlets at the university laboratory. Furthermore, this access impedance measurement system was extended to measure equipment load impedances during their operation mode on the power grid. The measured access and load impedances were also evaluated and verified according to their time and frequency characteristics. This evolution task represents the core objective of this thesis.

Finally, we introduce an optimization method to improve the transmission performance of narrowband-PLC systems in the case of low access impedances. In this regard, we present a method for modeling the voltage transmitted by PLC applications corresponding to time-variant access impedances. We show that we were able to increase the achievable data rate and the packet error rate over the signal to noise ratio compared to the state of the art transmission for measured low access impedances.

Zusammenfassung

Die Power-Line-Communication (PLC) steht für die Kommunikationstechnologie, die darauf abzielt, das Stromnetz für die Datenübertragung zu nutzen. Da das Stromnetz nicht für Datenkommunikationszwecke konzipiert wurde, ist die Übertragungsleitung feindselig und weist eine hohe Dämpfung, verschiedene Rauscharten und eine Frequenzselektivität auf, die durch das Vorhandensein von Verzweigungen und unerreichten Impedanz verursacht wird. Für ein effizientes Design der nächsten Generation von Smart Metering und PLC-Anwendungen ist, die perfekte Kenntnis des PLC-Kanals von grundlegender Bedeutung. Insofern wird in dieser Arbeit der Einfluss der niedrigen Anschlussimpedanz des Stromleitungskanals auf PLC-Systeme aus Telekommunikations- Sicht untersucht.

Durch den zunehmenden Einsatz von geschalteten Netzteilen mit EMV-Filtern in elektrischen Geräten im Stromnetz verschlechtert sich die Situation für die PLC Sendern und bekannte Konzepte verlieren dramatisch an Effizienz. Insbesondere niedrige Anschlussimpedanzen in bestimmten Frequenzbereichen führen dazu, dass die erlaubten Grenzwerte der EN 50065-1 immer öfter nicht mehr erreicht werden können und als Folge sich die Zuverlässigkeit der Übertragung deutlich verschlechtert, dies kann zum totalen Systemausfall führen.

In dieser Arbeit geben wir einen umfassenden Überblick über die Anschlussimpedanz des PLC-Kanals. Zunächst untersuchen wir die Auswirkungen der niedrigen Anschlussimpedanz auf schmalband PLC-Anwendungen mit begrenztem Stromverbrauch in Bezug auf die erreichbare Datenrate. Es wurde gezeigt, dass die Leistungsfähigkeit des Übertragungssystems für verschiedene Anschlussimpedanzszenarien reduziert wurde.

Anschließend entwickeln wir ein präzises Anschlussimpedanzmesssystem im Frequenzbereich von 30-500 kHz, um das Impedanzverhalten in Bezug auf Zeit und Frequenz zu analysieren. In diesem Kontext haben wir experimentelle Impedanzmessungen an verschiedenen Steckdosen des Universitätslabors durchgeführt. Außerdem wurde das Anschlussimpedanzmesssystem erweitert, um die Lastimpedanzen während des Betriebs am Stromnetz zu messen. Die gemessenen Anschluss und Lastimpedanzen werden ebenfalls nach ihrem Zeit- und Frequenzverhalten bewertet und verifiziert. Diese Entwicklungsaufgabe stellt das Kernziel dieser Arbeit dar.

Schließlich führen wir eine Optimierungsmethode ein, um die Übertragungsleistung von schmalband PLC-Systemen bei niedrigen Anschlussimpedanzen zu verbessern. Insoweit stellen wir ein Verfahren vor, um die übertragene Spannung durch PLC-Anwendungen nach zeitvarianten Anschlussimpedanzen zu modellieren. Es wird gezeigt, dass die erreichbare Datenrate und die Paketfehlerrate gegenüber dem Signal-Rausch-Verhältnis erhöht wurde, im Vergleich zu der Übertragung nach dem Stand der Technik für die gemessenen niedrigen Anschlussimpedanzen.

Acknowledgments

Undertaking this PhD has been a truly life-changing experience for me and it would not have been possible to do without the support and guidance that I received from many people.

First of all, I would like to express my special appreciation and thanks to Prof. Dr. Gerd Bumiller, for the guidance and great support he has given me during over six years, and not just for the scientific matters. He spent countless hours discussing my research and evaluating contemporary topics for me to investigate. I thank him for encouraging me to participate and present our research papers in international conferences, which not only improved my confidence but also gave me an opportunity to get feedback from the leading researchers in the world.

Next, I am deeply grateful to Prof. Dr. Han Vinck for his co-supervision, constant support, valuable comments, and being always there for great discussions. His hints helped me in all the time of research and writing of this thesis. I immensely enjoyed and learned from every meeting I had with him, where, besides research, we discussed a variety of things in life. I could not have imagined having a better mentor for my PhD thesis.

I would also like to thank my colleagues at the Hochschule Ruhr West who made a warm environment for me and supported this thesis in many ways. A special thanks to Christoph for a great cooperation in completing the fourth chapter of this thesis and to Sven for proofreading my abstract in German. I would also like to thank Babak, Stefan, Hongjian, Jan, and my colleague at the digital communication group, Yanling, Victor, and Thokozani for all the good times that we spent together.

I would like to express my heartfelt gratitude to my family and relatives in Germany, in the US, and in Syria. Thank you for your endless love and endless support. They had always been my well wishers, prayers and constant enthusiasm.

Last but not the least, I would like to declare my wholehearted appreciation and love toward my wife for her relentless love and support throughout my PhD work and life in general. Without her, I doubt that I would be in this place today. This thesis is heartily dedicated to my wife and our upcoming baby.

Contents

List of Figures

List of Tables

List of Acronyms

AC	Alternating Current
AFE	Analog Front End
AGC	Automatic Gain Control
AIMS	Access Impedance Measurement System
AMN	Artificial Mains Network
ARIB	Association of Radio Industries and Businesses
AWGN	Additive White Gaussian Noise
BB	Boradband
BPSK	Binary Phase Shift Keying
CENELEC	Comité Européen de Normalisation Électrotechnique
CEPRI	China Electrical Power Research Institute
CP	Cyclic Prefix
D/A	Digital to Analog or Analog to Digital Converter
DBPSK	Differential Binary Phase Shift Keying
DDS	Direct Digital Synthesizer
DFT	Discrete Fourier Transform
DQPSK	Differential Quadrature Phase Shift Keying
DUT	Device Under Test
ECB	Equivalent Complex Baseband
EMC	Electromagnetic Compatibility
EMI	Electromagnetic Interference
EN	European Norm
ETSI	European Telecommunications Standards Institute
FCC	Federal Communications Commission
FCH	Frame Control Header
FFT	Fast Fourier Transform
FOH	First Order Hold
HV	High Voltage
ICI	Inter Carrier Interference
IDFT	Inverse Discrete Fourier Transform
IEC	International Electrotechnical Commission
IEEE	Institute of Electrical and Electronic Engineers
IFFT	Inverse Fast Fourier Transform

IIR	Infinite Impulse Response
ISI	Inter Symbol Interference
ISO	International Organization for Standardization
IT	Isolation Transformer
ITU-T	International Telecommunication Union-Telecommunication Sector
LISN	Line Impedance Stabilization Network
LLR	Log-Likelihood Ratio
LP	Low Pass
LPTV	Linear Periodically Time-Variant
LTI	Linear Time-Invariant
LTV	Linear Time-Variant
LV	Low Voltage
MSE	Mean Square Error
MV	Medium Voltage
NB	Narrowband
NLS	Nonlinear System
OFDM	Orthogonal Frequency Division Multiplexing
PA	Power Amplifier
PER	Packet Error Rate
PHY	Physical Layer
PLC	Power Line Communication
QPSK	Quadrature Phase Shift Keying
SDO	Standards Developing Organization
SNR	Signal to Noise Ratio
SMPS	Switched-Mode Power Supply
RMS	Root Mean Square
RS	Reed-Solomon
RX	Receiver
TS	Technical Specification
TX	Transmitter
UNB	Ultra Narrowband
USB	Universal Serial Bus
V-I	Voltage-Current
VNA	Vector Network Analyzer

Chapter 1

Introduction

The communication technology that utilizes the power distribution grid to transfer data is commonly called power line communication (PLC). Reusing the PLC infrastructure for data communication purposes enables communications within smart grid applications such as automatic meter management and home automation and entertainment. However, the power line channel is considered as a harsh channel for data communication since it is subject to frequency- and time-varying behavior. It suffers from very low access impedances, attenuation, and different types of noise. Therefore, a lot of research, including our work, has been done to improve the knowledge of the PLC channel in the range of the frequencies of interest for communication purposes.

This thesis reports our investigation of the influence of low access impedances of the power line channel that reduces the performance of current narrowband PLC technologies such as PRIME and IEEE 1901.2. This investigation includes accurate access impedance measurements, load impedance measurements under the power of the mains voltage, and optimization procedures to increase the performance in the case of low access impedances.

In this chapter, we establish the background of this thesis and provide an overview of its organization. More precisely, in Section 1.1, we discuss current PLC systems with respect to their frequency range. Section 1.2 presents the problem statement of this thesis together with the state of the art. Finally, we list the contributions of this thesis and present a brief outline in Section 1.3.

1.1 The PLC Technology

PLC technology has experienced several developments and different implementations over the past years, depending on the use it was designed for. The first developments of PLC technology go back to the early 1900s, where it was used by power utilities for voice communications, control, and automation [1]. Since then, the application areas have expanded significantly because of the use of advanced modulation schemes, orthogonal frequency division multiplexing (OFDM), and the extension of digital signal processing [2].

1.1.1 Situation of PLC systems

The diversity of grid applications where PLC systems can be used has led to a multitude of specifications that have to be adopted during the development of standards. Regulatory activities are focused on coexistence with other systems that operate on the same medium or in the same frequency bands as PLC. A helpful classification of PLC systems with respect to frequency ranges is presented in [3] and is demonstrated in Fig. 1.1; it differentiates between ultra narrowband, narrowband, and broadband PLC systems, operating at about 125-3000 Hz, 3–500 kHz, and 1.8–250 MHz, respectively. Most recent developments in standardization and regulation activities over the past twenty years apply to narrowband and broadband PLC systems. This thesis focuses on narrowband PLC systems. A brief discussion of all three types of systems is presented in the following.

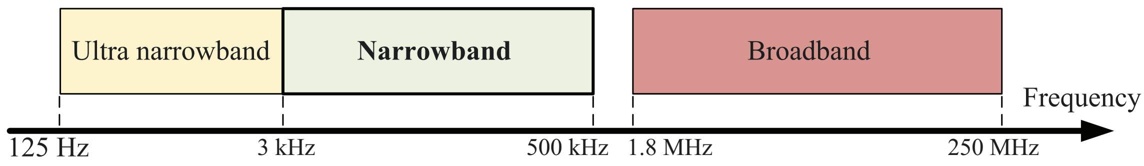

FIGURE 1.1: Frequency range classification of PLC systems

Ultra narrowband PLC (UNB-PLC) systems

UNB-PLC systems operate at a very low data rate, about 100 bps. They have a very large operational range (150 km or more). As far as PLC is concerned, the first deployments involved UNB-PLC technologies like the Turtle System [4] and TWACS [5], [6]. Although the data rate per link is low, deployed systems use various forms of efficient addressing that support good scalability possibilities. Despite the fact that these UNB-PLC solutions are proprietary, they are mature and have been used in the field for at least two decades.

Narrowband PLC (NB-PLC) systems

There are plenty of specifications for NB-PLC systems that support relatively low data rates (tens to hundreds of kbps) and are used in home and industry automation [7]. Several of these have been adopted as international standards and will be described in the next chapter.

For the European Union, the European standard (EN) 50065 (EN 50065-1:2011) [8]] was issued by the European committee for electrotechnical standardization (CENELEC) (3–148.5 kHz). It specifies four frequency bands for PLC systems: The A-band (3–95 kHz) is reserved exclusively for power utilities, the B-band (95–125 kHz) can be used for any application, the C-band (125–140 kHz) is specified for home network systems, and the D-band (140–148.5 kHz) is reserved for alarm and security systems. In the United States, NB frequencies are regulated by the federal communications commission (FCC), Title 47, Part 15 (9–490 kHz)

[9], and in Asia by the Japanese association of radio industries and businesses (ARIB) (10–450 kHz) [10]. Fig. 1.2 summarizes the frequency regulations of NB-PLC systems.

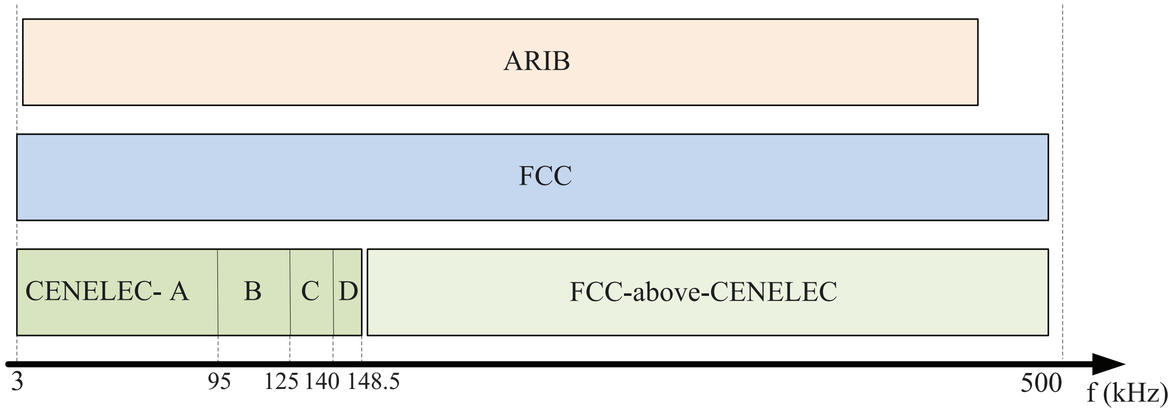

FIGURE 1.2: Frequency regulation of NB-PLC systems

Broadband PLC (BB-PLC) systems

BB-PLC systems support high data rates, with hundreds of Mbps. BB-PLC are applied in access and in-home domain solutions [11]. Generally, the access carries broadband internet using power lines and allows power companies to monitor power systems where in-home is used to network machines within a building. Different industry specifications are found as part of the development, mainly the HomePlug Powerline Alliance, the Universal Powerline Alliance, and the High-Definition Power Line Communication Alliance. They also test for interoperability and certify products based on the IEEE 1901 standards.

1.2 State of the Art and Current Problems

Smart meters are very important applications within the smart grid. They are usually connected to the power grid and able to communicate with each other using NB-PLC [12]. The implementation of more than 100 million PLC modems will be expanded worldwide in the next few years. However, the impedance on the power grid is a key aspect affecting the efficient development of PLC modems and its value has to be considered carefully. This impedance is denoted as access impedance and can be seen in power outlets of the low-voltage (LV) grid. In particular, it is a superposition of any appliances that are online and their connecting lines.

Recently, the energy consumption of new equipment and modems has been improved because of new energy efficiency regulations. In the beginning, this improvement was made possible through passive activities, e.g., better insulation of cooling units. However, more intelligent systems with switched-mode power supply (SMPS) are now being used. An SMPS unit is often equipped with an electromagnetic interference (EMI) filter to suppress noise and to be compliance with the electromagnetic compatibility (EMC) requirements. Fig. 1.3

depicts a block diagram of the input stage of typical electrical devices. They are usually equipped with an electrical plug and with a power cord. As many appliances connected to the grid are currently being replaced by devices with SMPS, the existing body of knowledge about access impedance on the power grid has to be updated.

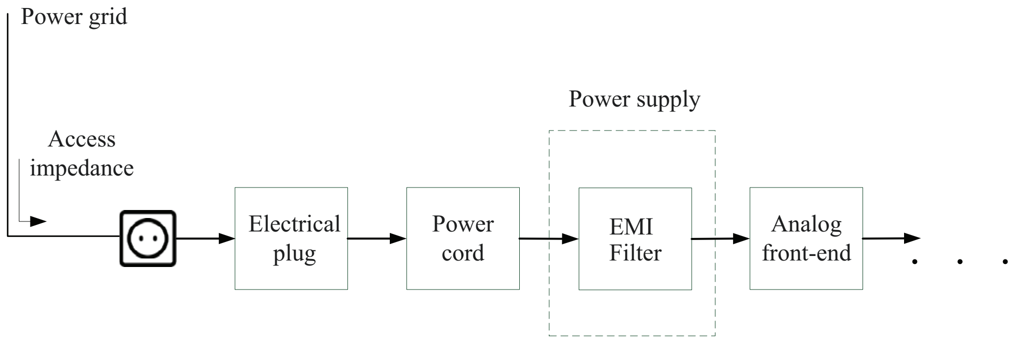

FIGURE 1.3: Input stage of a typical electrical device

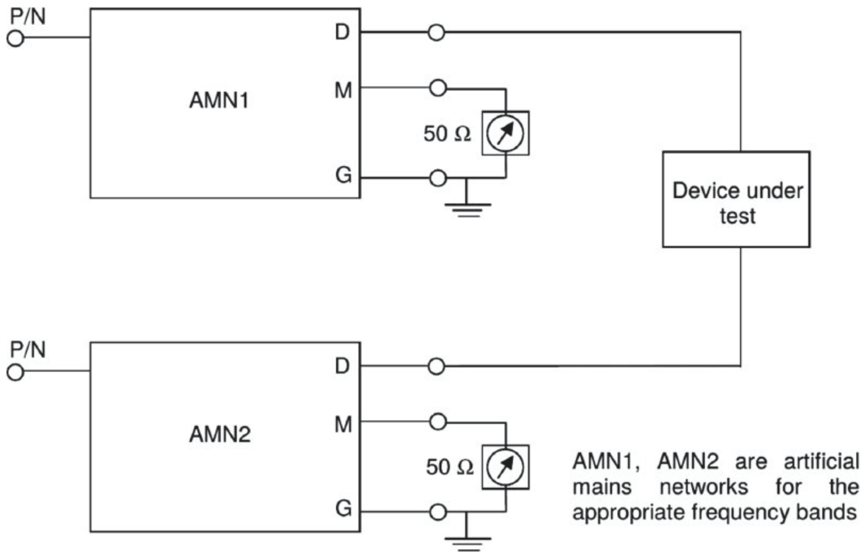

FIGURE 1.4: Line impedance stabilization network (LISN) for measurement of the output voltage, (from [8], Figure 4)

The output voltage level of the signal transmitted by PLC devices is measured via a line impedance stabilization network (LISN), as shown in Fig.1.4, which depicts Figure 4 of EN 50065-1 [8]. The artificial mains network (AMN) is specified in Figure 5 of EN 50065-1 [8]. In the context of this principle, the transmitted output voltage of PLC devices can only be reached if the termination impedance of the LISN is comparable to the actual impedance on the power grid. Fig. 1.5 shows the impedance response of AMN as a function of frequency.

Although there exist several types of EMI filters, they all use at least one line-to-line capacitor, also known as X-cap [13], whose goal is to suppress differential mode currents that flow along the line (hot) conductor and return through the neutral one. The magnitude of the impedance of the line-to-line capacitor is relatively small compared to the impedance of the device without the noise suppression capacitor within narrowband frequencies. As a consequence, it imposes a low impedance to the input of the circuit. Various results reported in the last few years regarding access impedance measurements in narrowband frequencies show very low impedances, below 1Ω [14], which differ from the specified termination impedance of the LISN (50Ω || 5Ω & 50mH) shown in Fig. 1.5.

Furthermore, the signals transmitted by PLC devices are limited due to technical reasons (e.g., waste heat) and energy efficiency reasons. The power consumption of the power amplifier of PLC devices is usually proportional to the transmitted current. This behavior is realized by a current measurement of the transmitted signal and a voltage reduction of the transmitted signal using a programmable amplifier. Thus the current threshold/power consumption is not exceeded. Therefore, the transmitted signal output voltage level according to EN 50065-1 is reduced in the case of low access impedances. Hence, the power amplifier loses efficiency and the internal thermal losses increase as well.

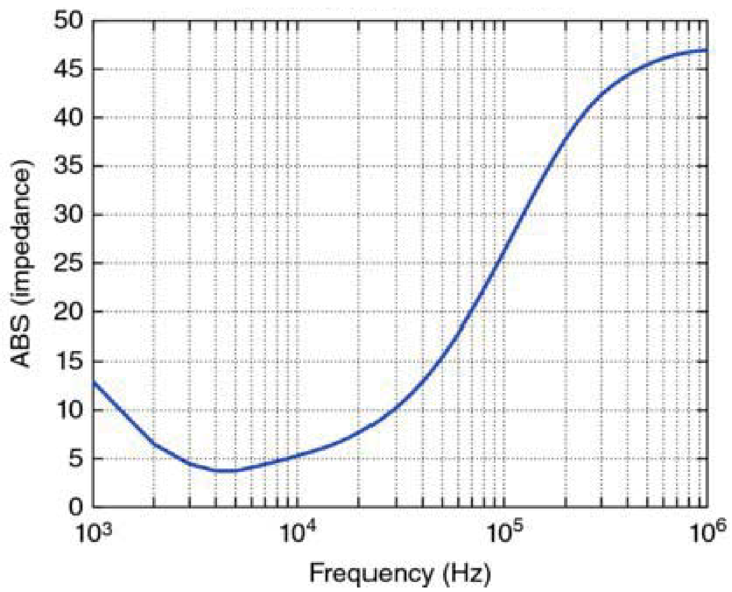

Figure 1.5: AMN impedance response as a function of the frequency, (from [8], Figure 5)

ETSI TS 103 909 [15] has been used lately to determine the quality of PLC devices with low access impedances since old measurements using the LISN cannot be considered realistic anymore. In [16], the measurement and evaluation of the notch depth achievable by PLC devices in narrowband frequencies with respect to ETSI TS 103 909 is presented. However, this platform cannot be assumed as a generally valid model as long as there are no approved models of access impedance behavior on the power grid. Therefore, standardization bodies will not address this issue and real access impedance measurements are necessary to specify the output voltage level of the signal transmitted by PLC devices.

Commercial equipment for measuring the access impedance on the power network is not available yet. In fact, carrying out such measurements is challenging since they have to be done under the power of the mains voltage. Power disturbances from the power grid cannot be easily separated from the measurement inputs. Standard galvanic isolation procedures cannot be applied because of the very low impedances and the availability for narrowband frequencies. Thus, classical measurement approaches for impedance measurement at the mains voltage cannot be used.

1.3 Thesis Contributions and Outline

In this work, we provide several scientific contributions that go beyond the current state of the art in the PLC environment, highlighting the transmission scenario in the case of low access impedances. We extend the body of knowledge about PLC channel access impedance in narrowband frequencies and its effects on PLC systems. It is known that the access impedance of the PLC channel exhibits a time- and frequency-variant behavior, but the mismatch between assumed and real access impedances is often not considered. This behavior has been confirmed by our practical observations. Furthermore, we exploit our own research results to enhance the transmission of NB-PLC systems in the case of low access impedances. In order to investigate the research problems, four research questions are formulated:

(i) What is the influence of low access impedances on transmission over the PLC under the condition of limited power consumption of the transmitters?

(ii) What are the constraints and specifications for developing an accurate access impedance measurement system for NB frequencies?

(iii) How can load impedances be separated from the measured access impedances and how can they be analyzed?

(iv) How can the transmission of NB-PLC systems be improved in the case of very low access impedances and limited power consumption?

All of the above-listed questions will be examined in detail and answered. In the following, an outline of the structure of this thesis is provided, summarizing the main contents and the concepts that will be detailed throughout this work. Fig. 1.6 illustrates the structure of the thesis including the main points and results.

Chapter 2 discusses different aspects of NB-PLC. It provides important information for the characterization and implementation of NB-PLC applications. This study investigates PLC channel modeling according to a linear time-variant system. We also present an overview of available NB-PLC standards and technologies. Two of these standards will be implemented in this thesis.

Chapter 3 focuses on the effects of low channel access impedance, which reduces the performance of NB-PLC transmission systems under the condition of the power consumption limitation of PLC modems. As shown in Fig. 1.6 (related to Chapter 3), the signal to noise ratio (SNR) has been decreased for subcarriers with low access impedances, which results in a reduction of the achievable data rate by 55-90% for different impedance scenarios. In addition, we show the coexistence problem caused by changing the impedance values between the transmitting and the receiving state of smart grid applications.

Chapter 4 presents the main part of this thesis, where we introduce a description of an accurate access impedance measurement system in the frequency range of 30-500 kHz. This measurement system applies signal processing in order to remove all parasitic effects that affect the measurement. We determined the accuracy of the measurement system based on offline measurements. Finally, the results of access impedance measurements performed on different power outlets at the university laboratory will be presented. The variable characteristics of the network impedance over time and frequency caused by the devices connected to the grid will be presented, as shown in Fig. 1.6 (related to Chapter 4).

Chapter 5 makes a contribution by extending the access impedance measurement system presented in Chapter 4 to enable measuring the impedance of electrical equipment in operation mode. We carried out a measurement campaign on a representative set of devices that can be found in a house, office, or laboratory. We will show very low access impedances and strong time variation within the frequency range of 30-500 kHz, as presented in Fig. 1.6 (related to Chapter 5). The measured load impedances will finally be evaluated and verified with respect to time and frequency.

Chapter 6 presents a modeling method for the transmitted voltage and current of PLC devices corresponding to the measured time- and frequency-variant access impedances introduced in Chapter 4. The modeling method is based on the impulse response of RLC filters that simulate the behavior of the measured access impedances. The investigated voltage and current models will be evaluated and verified using simulation results. These models will then be used in Chapter 7 to improve the transmission scenario presented in Chapter 3. We will then show the effects of low access impedances on the signal transmitted by and the current flowing through PLC devices as shown in Fig. 1.6 (related to Chapter 6), where the behavior of the shape of the transmitted chirp signals depends on the low access impedance.

Chapter 7 introduces an optimization algorithm for improving the signal transmitted by PLC devices in the case of low access impedances and limited power consumption of the transmitters. The optimization method on the transmitter side is realized by switching off subcarriers in frequencies with low access impedances and high current, which increases the SNR level on the other subcarriers with suitable access impedances, as shown in Fig. 1.6 (related to Chapter 7). The achievable data rate has been increased compared to the state of the art transmission presented in Chapter 3 for the same access impedances. We will also determine the optimal number of suppressed subcarriers that delivers the maximum benefit. The performance of the optimization method will finally be examined with respect to the packet error rate.

Chapter 8 is the last chapter of this thesis. It contains a summary of our contributions reported in this thesis and sketches an outlook on possible future work.

1.4 Related Publications

The main results of the work presented in this thesis have been published in high-quality international academic papers in the form of journal papers and conference papers. The following is a list of these publications with a reference to the part of the thesis where their contents are discussed.

1.4.1 Journal paper

1. George Hallak, Christoph Nieß, and Gerd Bumiller, "*Accurate Low Access Impedance Measurements with Separated Loads Impedance Measurements on the Power Line Network*", IEEE Transactions on Instrumentation and Measurement. 2018 March 29. [The contents of this paper can be found in Chapters 4 and 5].

1.4.2 Conference papers

1. George Hallak and Gerd Bumiller, "*Coexistence Analysis of Impedance Modulating Transmitters*", In International Symposium on Power Line Communications and Its Applications (ISPLC), Johannesburg, South Africa, 2013 IEEE. [The contents of this paper can be found in Chapter 3.]

2. George Hallak and Gerd Bumiller, "*Throughput Optimization Based on Access Impedance of PLC Modems with Limited Power Consumption*", In Global Communications Conference (GLOBECOM), Austin, USA, 2014 IEEE. [The contents of this paper can be found in Chapter 3.]

3. George Hallak and Gerd Bumiller, "*Data Rate Optimization on PLC Devices With Current Controller for Low Access Impedance*", In International Symposium on Power Line Communications and its Applications (ISPLC), Bottrop, Germany, 2016 IEEE. [The contents of this paper can be found in Chapter 3.]

4. George Hallak, Gerd Bumiller, and Christoph Nieß, "*Accurate Access Impedance Measurements on the Power Line with Optimized Calibration Procedures*", In International Instrumentation and Measurement Technology Conference (I^2MTC), Turin, Italy, 2017 IEEE. [The contents of this paper can be found in Chapter 4.]

5. George Hallak and Gerd Bumiller, "*Impedance Measurement of Electrical Equipment Loads on the Power Line Network*", In International Symposium on Power Line Communications and its Applications (ISPLC), Madrid, Spain, 2017 IEEE. [The contents of this paper can be found in Chapter 5.]

6. George Hallak and Gerd Bumiller, "*Time Variant Voltage and Current Modeling Corresponding to Access Impedance Measurements*", In International Symposium on Power Line Communications and its Applications (ISPLC), Manchester, UK, 2018 IEEE. [The contents of this paper can be found in Chapter 6.]

7. George Hallak and Gerd Bumiller, "*TX-Signal Optimization in Current Control State of PLC Transmitter by Low Access Impedance*", In International Symposium on Power Line Communications and its Applications (ISPLC), Manchester, UK, 2018 IEEE. [The contents of this paper can be found in Chapter 7.]

1.4.3 Other contributions

1. George Hallak and Gerd Bumiller, "*PLC for Home and Industry Automation*", Power Line Communications: Principles, Standards and Applications from Multimedia to Smart Grid (2016), p.449. [**Book Chapter**.]

2. George Hallak, Christoph Nieß, and Gerd Bumiller, "*Measurement Setup for Notch Evaluation of Narrowband PLC Devices*", In Global Communications Conference (GLOBECOM), Singapore, 2017 IEEE.

1.4.4 Copyright information

Parts of this thesis have already been published as a journal article and in conference proceedings as listed in the publication list. These parts, which are, apart from minor modifications, identical with the corresponding scientific publication, are © 2013-2018 IEEE.

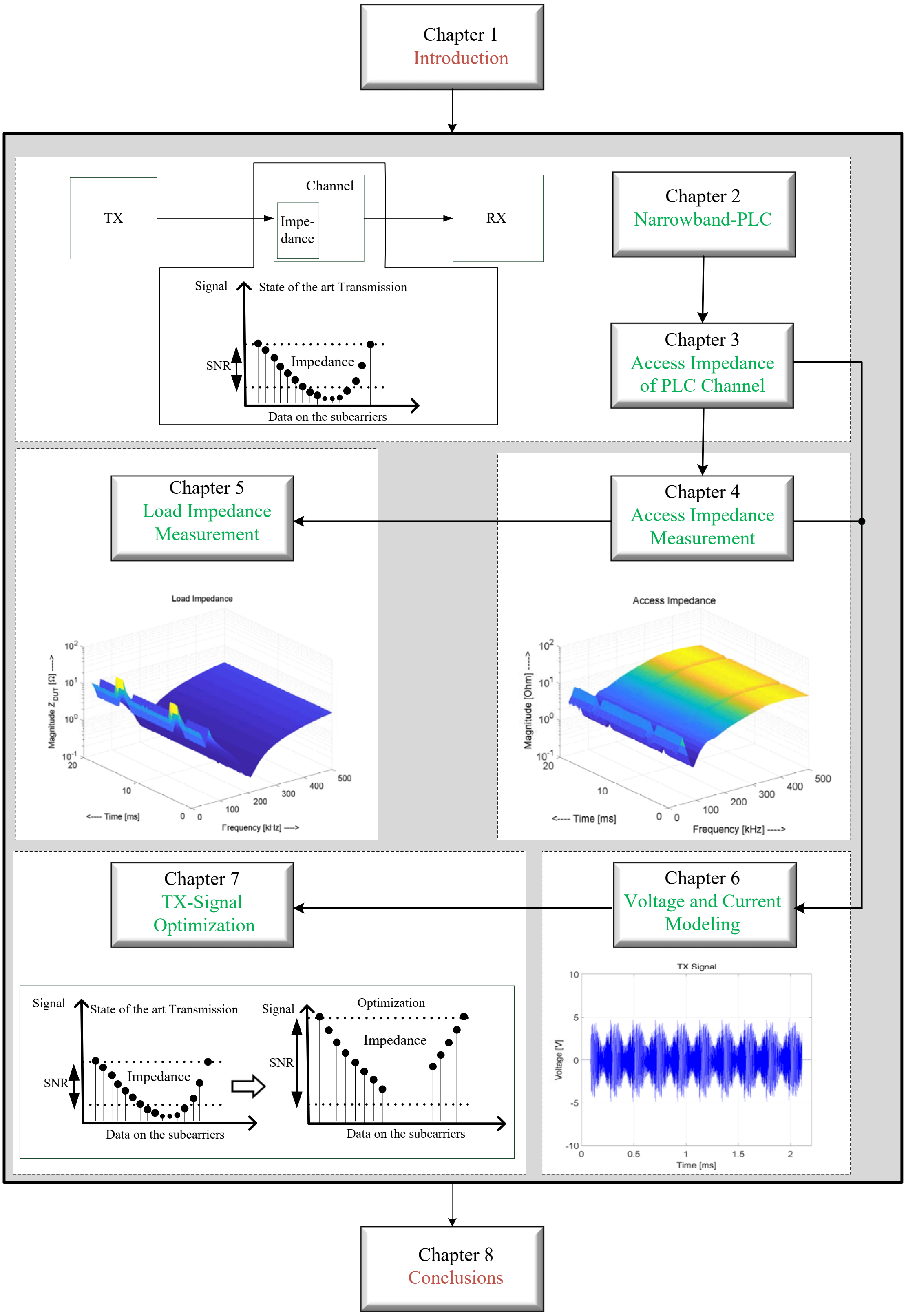

FIGURE 1.6: Thesis structure

Chapter 2

Narrowband-PLC

This chapter discusses different aspects of narrowband-PLC. It is intended to provide necessary information from a communication system's point of view, so that the characterization and implementation of NB-PLC applications can focus on the channel properties that are relevant for communications. Thus the channel modeling and characteristics will be studied. A typical structure of PLC systems will be presented. The used digital modulation technique OFDM for NB-PLC applications will be also discussed. Finally, An overview of available NB-PLC communication standards and systems will be given.

2.1 Introduction

The collaboration between channel characterization and systems development is a prerequisite for a successful design of any communication system. The main technical challenge in PLC is the modeling of the power line channel. The power line channel is a very harsh environment, frequency- and time-variant, and impaired by different noise types. In addition, the structure of the power grid varies from country to country and even within the same country which leads to difficulties by modeling the power line transfer function [17].

Traditional models for PLC channel assume a linear time-invariant (LTI) behavior where changes in the response can be only represented by long-term variations. However, the channel transfer function of the PLC channel changes when the topology varies, i.e. when devices are switched on or off, resulting in a time-varying behavior. Objectively, the power line channel presents a short-term variation caused by the high frequency parameters of loads, which can transpose in periodic variations of load impedances. Interesting works on PLC channel modeling are presented in [18]–[22].

In PLC technologies, the real world noise and attenuation are different from the additive white Gaussian noise (AWGN). The non-Gaussian behavior of the PLC channel is mostly considered to be the reason of the low performance of PLC [2]. PLC noise can be viewed as a combination of various types of noise [23], [24]. NB-PLC noise characterization and measurement are considered in [22], [25], [26]. The PLC transfer function characteristics are studied in [26], [27] and measured in [28], [29]. However, the PLC access impedance is often neglected and its influences is not considered. The already done access impedance measurements in narrowband frequencies are very less such as [14], [30].

The OFDM modulation scheme is considered as one of the best candidates for PLC applications [31], [32], because of its excellent bandwidth efficiency and possibilities to handle multipath propagation. The OFDM technique can control independently each subcarrier and the transmitted power because of the orthogonal subcarriers arrangement. However, the performance of OFDM with its large number of parallel subcarriers can be affected by the time-variant behavior of PLC systems.

At the same time, there is no public regulation or standardization body that evaluates and certifies the technology available in the market. Customers need to trust technology providers, which is difficult regarding to the high investment cost. The main available OFDM NB-PLC standards are the published recommendations of ITU-T and IEEE [3]. Frequency band plans for these standards and specifications for NB-PLC systems are discussed in [33].

This chapter is organized as follows: The PLC channel modeling is described in Section 2.2. This model will be used in Chapter 3 to investigate the influence of the access impedance of the power line. The general structure of PLC systems is introduced in Section 2.3. The multi-carrier modulation technique OFDM used by most NB-PLC technologies is explained in Section 2.4. An overview of the available NB-PLC standards for smart grid applications is given in Section 2.5. Finally, the chapter is concluded in Section 2.6.

2.2 PLC Channel Modeling and Characterization

The analysis of the PLC channel requires a simplification, since this environment exhibits a complex behavior. Due to the time-varying nature of the real world channel, the channel model can be extended from a simplified linear time-invariant (LTI) over linear time-variant (LTV) and linear periodically time-variant (LPTV) descriptions.

A PLC channel can be considered as a nonlinear system (NLS) because it contains some nonlinear devices. At the input of the channel, two signals can be seen: the communication signal with high frequency and low level, and the mains signal with very low frequency and large level, as depicted in Fig. 2.1. Transmitters and receivers are equipped with high pass filters that prevent the mains voltage from entering the communication equipment. Therefore, all components that do not contain the communication signal are filtered because of their low frequency. As a result, the simplification complies with a quasi-linear but periodically time-varying system [34]. Hence, their response can be calculated from a sequence of states in which the system behaves as a linear time-invariant. The mathematical model for a PLC channel is investigated in (2.2.2).

2.2.1 State of the art in channel modeling

The channel modeling approaches available in the PLC literature, can be generally divided into two methodologies, namely the statistical approach and the deterministic approach, as illustrated in Fig. 2.2. The statistical approach is based on preliminary measurements and statistical analysis methodologies. The channel influence on the transmitted signal can

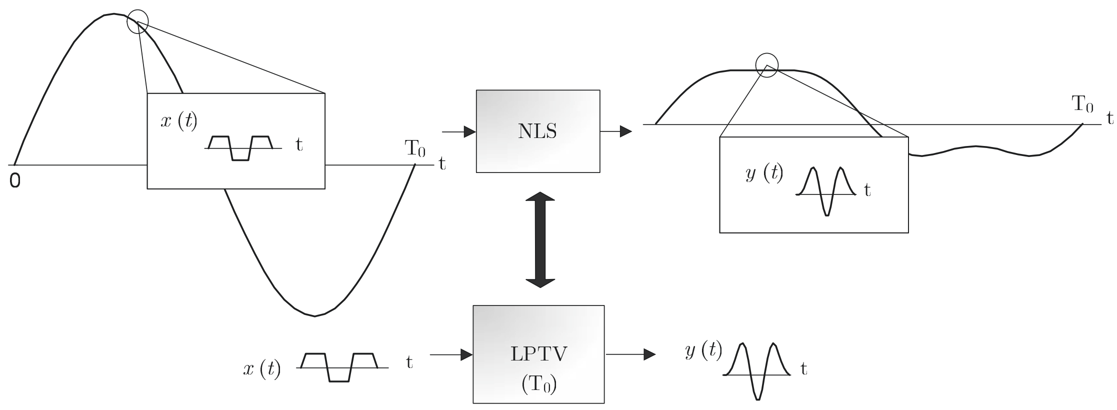

FIGURE 2.1: Diagram of the origin of the LPTV behavior, (from [2], Figure 2.59

be modeled using a filter. The deterministic approach develops a closed-form expression under consideration of detailed network knowledge, such as network topology, cable material, connected appliances, etc. Both approaches have their advantages and disadvantages, as investigated in details in [2].

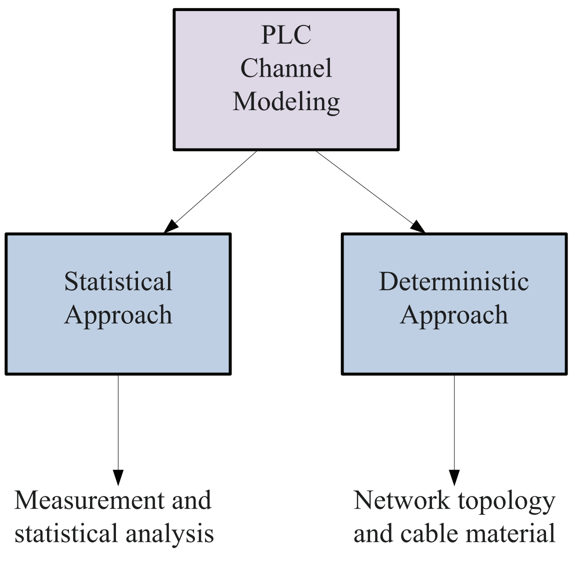

FIGURE 2.2: PLC channel modeling approaches

In addition to the two fundamental approaches to PLC channel modeling, namely the deterministic approach and the statistical approach, there exists numerous efforts in the literature in order to accurately model the PLC channel in different scenarios. It has been recently proposed to combine these two approaches to give rise to hybrid models which indeed offer advantages [35]. In hybrid models, one can define a set of topologies that can be considered as representative of the majority of topologies which can be found in the field for a specific scenario or by generating randomly a set of statistically relevant transfer functions. These models can be categorized as low-voltage (LV, 230/400 V), medium voltage (MV, between 1 and 35 kV), and high voltage (HV, 110 kV and above) channel models. A typical structure of the European 50 Hz power distribution grid is shown in Fig. 2.3. In the following we briefly describe the state of the art in LV, MV, and HV channel modeling.

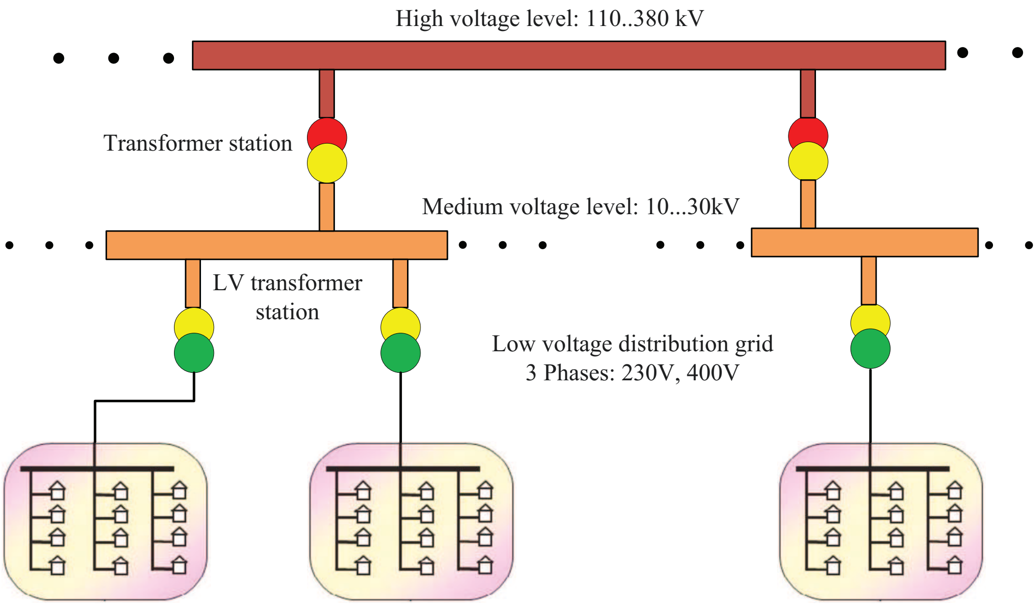

FIGURE 2.3: The European power supply network structure

The LV channel models are used for the access domain, which indicates the low-voltage power distribution grid between the transformer stations and home connections, as well as the in-home communications. For indoor LV channels different models have been proposed. The most important feature of the indoor LV channel is the strong sensitivity in the frequency domain due to the impedance mismatch problems and their time variation. A deterministic bottom-up approach has been introduced in [35], [36], which presents a model based on the transmission line model in terms of cascaded two-port networks. Another bottom-up approach is the statistical model, which defines the channel parameters from the physical network features [37]–[40]. Other proposed models for the indoor channel adopt a top-down approach, which use measurement campaigns in order to model the channel in such way, that it corresponds to the real measurements [41]–[43].

The MV channel models are used for the part of the power line, which connects the distribution substations that terminate the HV transmission network to the LV distribution transformers. The channel impairments encountered in MV lines are usually intermediate between those impairments encountered in LV and HV lines. Measurement based characterization of the MV channels is done in two different levels. In particular, the component level and the network level [44]–[47]. Another approach for MV channel modeling is the theory based characterization or physical approach that seeks to predict channel characteristics strictly from detailed knowledge of the scenario geometry [48]. The HV channel models are used for the part of the power line between the generating power plants and the remote electrical substations. Some efforts for HV channel modeling can be found in [49], [50].

2.2.2 Theoretical basis for PLC channel modeling

The PLC channel can be generally described as a linear time-variant system due to the multipath propagation of the transmitted signal. The multipath nature of the power line channel arises from the presence of several branches and impedance mismatches that cause multiple reflections. A mathematical representation of an LTV system by its input-output relation is given as in [51] by

$$s_{out}(t) = \int_{-\infty}^{\infty} h_{sys}(t,\tau) s_{in}(t-\tau) d\tau, \tag{2.1}$$

where $h_{sys}(t,\tau)$ is the time-variant impulse response of the system, which represents the response at the instant t, and τ denotes the time delay of the system input signal. The additive noise is ignored for clarification.

The LTV channel model in (2.1) is illustrated in Fig. 2.4 using input-delayline-structure.

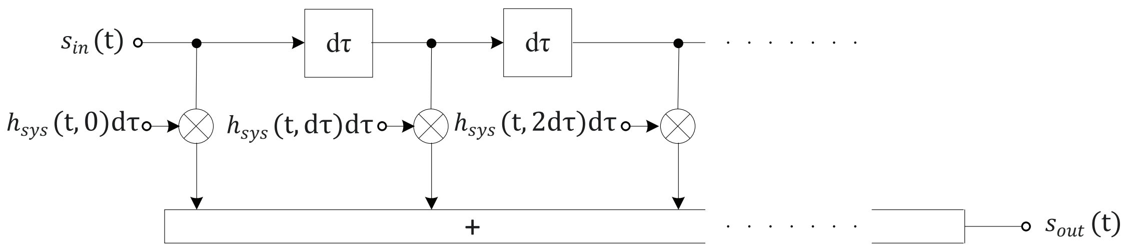

FIGURE 2.4: LTV system modeling using input-delayline-structure

The transfer function of the LTV system is obtained after applying the Fourier transform, to the impulse response, in the τ variable as in [51] by

$$H_{sys}(t,f) = \mathfrak{F}_{\tau}\{h_{sys}(t,\tau)\} = \int_{-\infty}^{\infty} h_{sys}(t,\tau) e^{-j2\pi f\tau} d\tau, \tag{2.2}$$

where $\mathfrak{F}_{\tau}\{\cdot\}$ stands for the functional relationship between input and output, and f stands for frequency.

The Fourier transform with $S_{in}(f) = \mathfrak{F}_t\{s_{in}(t)\}$ of the input signal $s_{in}(t)$ obeys the principle of superposition [52]. Thus, the relation between the input and output signal can be presented from (2.1) and (2.2) as

$$s_{out}(t) = \int_{-\infty}^{\infty} H_{sys}(t,f) S_{in}(f) e^{j2\pi ft} df. \tag{2.3}$$

The time-varying characteristic of the system response is only related to the mains signal which is periodic in time and so the system is LPTV and can be described as in [53] by

$$h_{sys}(t, t-\tau) = h_{sys}(t - \nu T_0, t - \nu T_0 - \tau), \tag{2.4}$$

with T_0 the fundamental period equal to 20ms and $\forall \nu \in \mathbb{Z}$.

Since the channel response $h_{sys}(t, t-\tau)$ is periodic in time t with period T_0. This periodicity also appears in the frequency domain as

$$H_{sys}(t,f) = H_{sys}(t - \nu T_0, f). \tag{2.5}$$

Nevertheless, the LPTV model for PLC channels admits an additional simplification to be considered as LTI. The channel variation is quite slow, that is, the time duration which the channel properties can be considered invariant is several orders of magnitude above the duration of the impulse response. The duration of the former is about hundreds of µs [20] while the latter is only of some µs [54]. For this reasons, it is possible to make a locally invariant approximation of the channel response and to represent the LPTV system as a collection of successive LTI states that appear periodically. In other words, the mains period can be divided into a series of shorter invariance intervals, at which a snapshot of the channel response is taken. Then, the channel can be represented by a periodical series of such invariant responses that represents a sampled version of its time-variant response. This study is investigated in detail in [20].

2.2.3 Signal processing channel model

In order to provide a full description of the PLC channel properties for test and verification of PLC devices, we need to distinguish between physical channel properties and channel properties related to signal processing.

The channel model with respect to signal processing is proposed in Fig. 2.5. The transmitted signal $x(t)$ is affected by the channel impulse response $h(t,\tau)$ that is generally time-variant. The received signal is then obtained by adding time-variant noise signals $n(t,\tau)$ to the modified transmitted signal $x(t) * h(t,\tau)$. The relation between the transmitted signal and the received signal is given with respect to (2.1) by

$$y(t) = x(t) * h(t,\tau) + n(t,\tau), \tag{2.6}$$

where (*) represents the convolution operation.

Equation (2.6) is the most fundamental equation that describes a PLC transmission channel and can be digitally implemented.

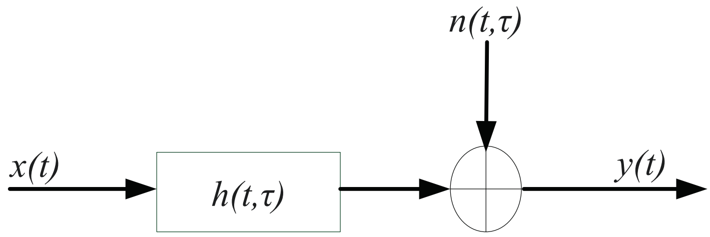

FIGURE 2.5: Signal processing model of a PLC channel

2.2.4 Physical channel model

The effects of the PLC channel on the transmitted signal is considered so far only from a signal theoretic perspective. However, the physical properties of the mains grid have a significant influence on the PLC transmitted signals at narrowband frequencies. The physical PLC channel consists typically of:

- Access impedance: The access impedance is presented at the output of the PLC modem at the transmitter side. It is usually time-variant and frequency-dependent instead of being flat, which causes a nonlinear behavior. Its value observed to be complex and very low at the narrowband frequencies, in some cases below 1Ω [14].

- Transfer function: The signal propagation in NB-PLC is frequency-dependent and has a large attenuation in low frequency range as shown in [28], [55], [56]. Narrowband frequency selective fading can occur depending on the load. Deep notches and large attenuation have been observed for models described in [57]. In contrast to broadband PLC where the frequency response is dominated by a multipath propagation, the frequency dependency of NB-PLC channels is basically caused by appliances connected to the grid. In addition, the transfer function is also time-variant due to the time-variant behavior of loads.

- Noise: NB-PLC noise differentiates between several kinds of additive noise, i.e. periodic impulsive noise produced by power supplies and synchronous with the mains frequency, periodic impulsive noise asynchronous with the mains frequency formed by periodic impulses, asynchronous impulsive noise caused by connection and disconnection electrical devices, and colored background noise with a relatively low power spectral density which results from the contribution of multiple noise sources of unknown origin [58]–[61].

The transmitted information into the power grid depends on the used coupling approach. The capacitive coupling is typically used on LV grid, whereas the inductive coupling is used in MV grid. Therefore, the transmitted signals on LV grid are represented by voltage signals. Current and power signals are results out of the time-variant coupling impedance. Furthermore, the analog to digital converter at the receiver side measures also voltages. As a consequence, the voltage signal is used as a characteristic value for the channel modeling.

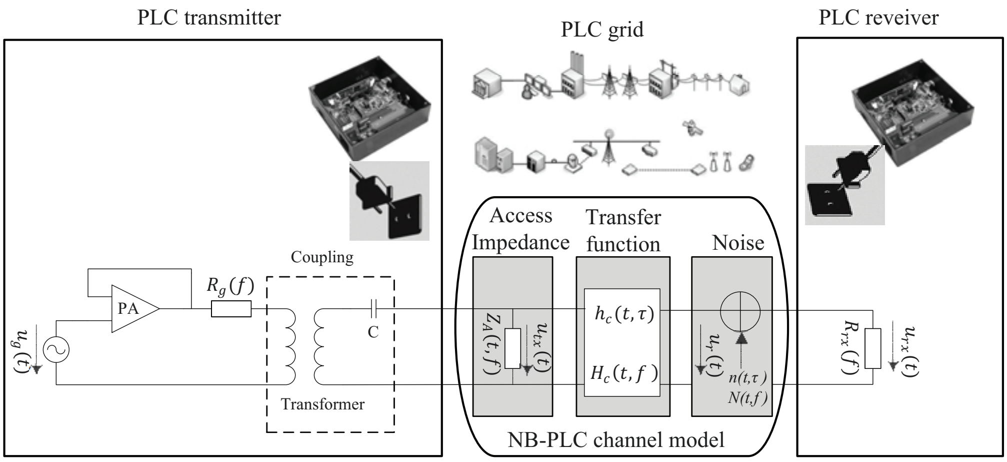

FIGURE 2.6: Physical channel model of NB-PLC

The physical channel model of NB-PLC is presented in Fig. 2.6. The two indexes t and f represent the time and frequency domain indexes, respectively. The signal $u_g(t)$ is generated by a signal generator at the transmitter and then amplified by a power amplifier (PA). The coupling circuit of the transmitter is represented by the transformer with the capacity and its influence can be simplified by the time-invariant internal impedance $R_g(f)$ at the output of the transmitter. The impedance $R_g(f)$ is given as a resistor because the behavior of the coupling is dominated by the ohmic part in the narrowband frequency range. The time-variant access impedance $Z_A(t, f)$ is the impedance observed at the power outlet. Together with the resistor $R_g(f)$ of the transmitter, it determines the transmitted signal level that can be injected into the power line network $u_{tx}(t)$. The signals $U_g(f)$ and $U_{tx}(t, f)$ represent the same signals in the frequency domain. The ratio between the two signal $U_g(f)$ and $U_{tx}(t, f)$ is time- and frequency-dependent and subject to coupling loss [62] caused by the impedance mismatch. This ratio has to be compensated in the channel modeling. The magnitude ratio of $u_{tx}(t)$ to $u_g(t)$ can be obtained by

$$H_A(t, f) = \frac{Z_A(t, f)}{Z_A(t, f) + R_g(f)}, \tag{2.7}$$

where the magnitude of $H_A(t, f)$ is smaller than 1 [62].

The transfer function of the channel $H_c(t, f)$ describes the relation between the signals $U_{tx}(t, f)$ and $U_r(t, f)$ in the frequency domain and the $h_c(t, \tau)$ is the impulse response at the time t caused by an impulse excitation applied at the time $t - \tau$ [63]. The PLC receiver is simplified by the passive resistor R_{rx}. It is typically high impedance and its influence on the parallel access impedance $Z_A(t, f)$ can be ignored. The received signal $u_r(t)$ represents the attenuated signal from the transmitted signal. Thus, the signal $u_r(t)$ can be given with respect to the model in (2.1) as

$$u_r(t) = \int_{-\infty}^{\infty} h_c(t,\tau) \cdot u_{tx}(t-\tau)d\tau. \tag{2.8}$$

The relation between the transfer function $H_c(t,f)$ and the impulse response $h_c(t,\tau)$ can be found similar to the model in (2.2). The combination of all interference at the receiver side is denoted by $n(t,\tau)$. Therefore, the received signal at the receiver side can be found in the time domain as

$$u_{rx}(t) = u_g(t) * h_A(t,\tau) * h_c(t,\tau) + n(t,\tau), \tag{2.9}$$

or in the frequency domain as

$$U_{rx}(t,f) = U_g(f) \cdot H_A(t,f) \cdot H_c(t,f) + N(t,f). \tag{2.10}$$

2.3 PLC System Structure

Most NB-PLC systems have mutual system structure although they have different implementations. Typical NB-PLC devices and modems have usually a power supply, a line driver, an analog front end (AFE), layers controllers, and coupling circuit. The power supply supplies the transmitter circuit with suitable power and considers the electromagnetically compatibility regulations. However, the power supply and the signal generator of the transmitter are operating on the same path to the PLC channel. Thus, a high impedance has to be seen at the transmitter circuit and the transmitted signal should not be affected by the power supply. A Typical structure of PLC modem is shown in Fig. 2.7

The AFE operates usually in the transmit and receive path. It converts the digital values to an analog signal and samples the received signal into digital values using a digital to analog (or analog to digital) converter (D/A). Typical AFEs are equipped with an analog filter. The TX filter is located just after the D/A in the TX signal path and the RX filter is located just before the D/A in the RX signal path. A line driver is usually used in the transmit path to insert the transmitted signal into the power line and set a high current to drive the low impedance of the power line in a correct way. The line driver is not directly connected to the mains because it damages the circuit. A coupling circuit is needed to galvanic isolate the circuit from the mains and blocks the mains voltage.

The physical layer of most PLC systems based OFDM encloses channel coding with error detection and correction, modulation and demodulation, and synchronization. Block diagrams of typical OFDM PLC transmitter and receiver are shown in Fig. 2.8 and Fig. 2.9, respectively.

On the transmitter side, the PHY receives the data and send it to a scrambler to avoid the occurrence of long sequences of identical bits. The data bits are then encoded adding redundancy bits in order to be recovered by the receiver to find the error bits. The interleaver

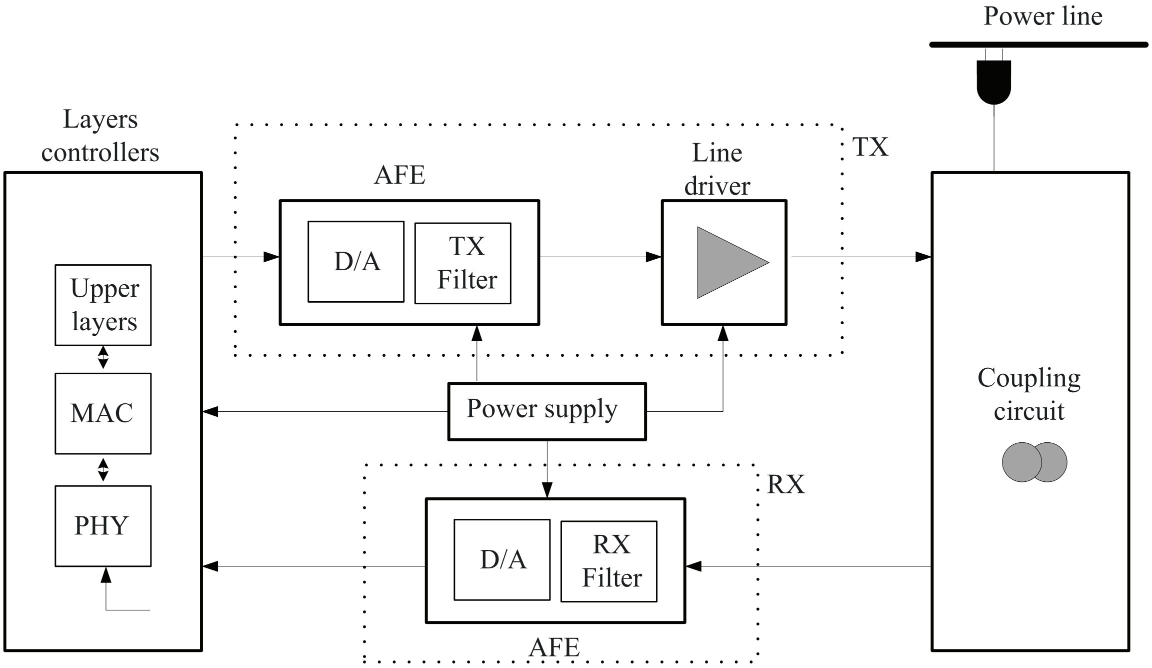

Figure 2.7: Structure of PLC modem

provides protection against burst errors that corrupt a few consecutive OFDM symbols. The interleaved OFDM symbols are modulated in the frequency domain and converted to the time domain using the inverse fast Fourier transform (IFFT). The cyclic prefix is added to the time domain signal and windowing is applied to reduce the out-of-band emission and to reduce the spectral side lobe. On the receiver side, the received signal is synchronized and the cyclic prefix is removed. The signal is converted to the frequency domain using the fast Fourier transform (FFT) and the OFDM symbols are detected and demodulated by the evaluation of log-likelihood ratio (LLR). The LLRs are then deinterleaved, decoded and descrambled. The data bits are finally determined and forwarded to the higher level.

2.4 Digital Modulation Techniques

Digital modulation is the core of any communication system, including PLC. In such of an unreliable channel, the typical modulation techniques may need adaptation and new development. More than one appropriate modulation technique could be applicable under different channel conditions or applications. Therefore, the robustness of modulation techniques for varying PLC channel is an important factor. Single carrier modulation techniques are used in the first NB-PLC systems and multi-carrier modulation techniques are used in the recent NB-PLC systems. Since most of the current NB-PLC technologies are based on OFDM, this technique will be here investigated.

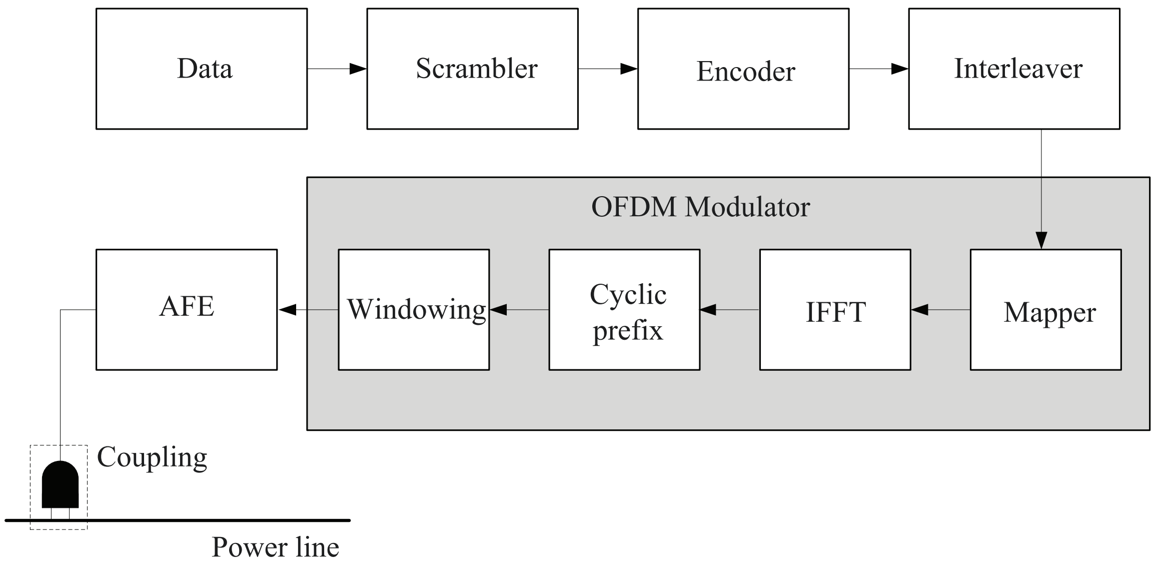

FIGURE 2.8: Block diagram of OFDM PLC transmitter

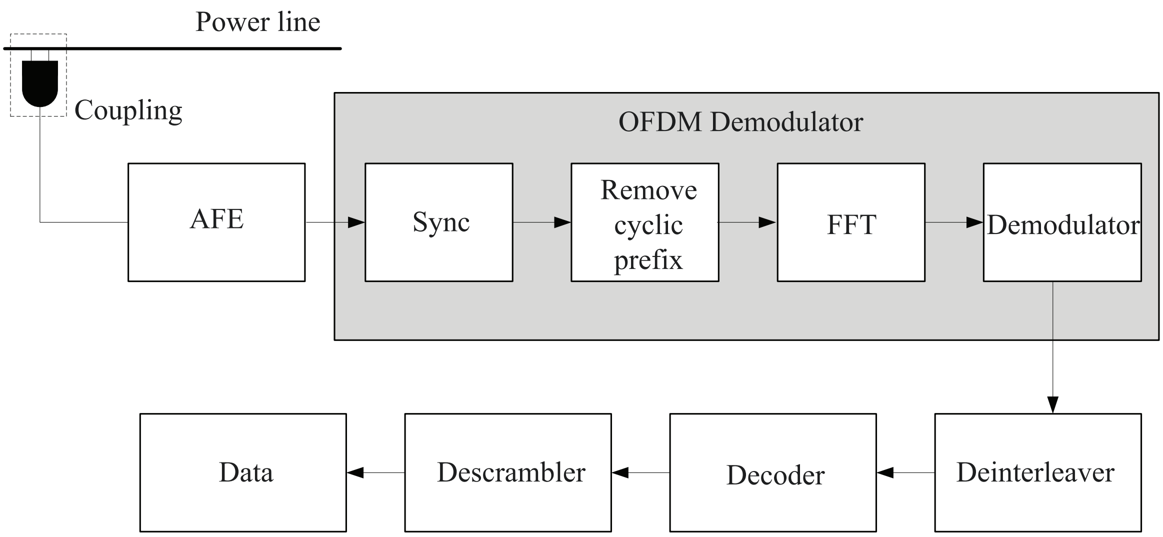

FIGURE 2.9: Block diagram of OFDM PLC receiver

2.4.1 Orthogonal frequency division multiplexing (OFDM)

A multi-carrier transmission is a commonly used communication technology, due to its high data rate and spectral efficiency. It can be implemented in different ways, such as vector coding [64], or orthogonal frequency division multiplexing (OFDM) [65]. These techniques are based on the same principle, which is dividing a wide channel into multiple parallel narrow channels in terms of orthogonal channel partitions. In the PLC systems, OFDM modulation is applied in order to encode orthogonal signals of digital data in multiple subcarriers to be transmitted with different frequencies through the PLC channel. The data signals before being modulated by the OFDM demodulator are orthogonal to each other. This orthogonality prevents interference between subcarriers and facilitates the transmission of subcarriers at the same time [2].

However, OFDM suffers from delay spread caused by traveling symbols one by one from transmit to receive end, which manifests itself as inter symbol interference (ISI) on each subcarrier channel due to pulse overlapping. The ISI is avoided by inserting a guard interval (cyclic prefix), for each OFDM symbol. The guard interval is chosen longer than the expected delay spread, such that multipath components from one symbol cannot interfere with the next symbol. Therefore, it provides robustness against multipath fading [66].

Basics of the OFDM transmission technique

The basic idea of OFDM is to split a high speed serial data stream into a large number of L parallel low speed substreams, so that the symbol duration is L times longer than the original one as shown in Fig. 2.10 for L= 4. The duration of one OFDM symbol T_o is equal to $L \cdot T$.

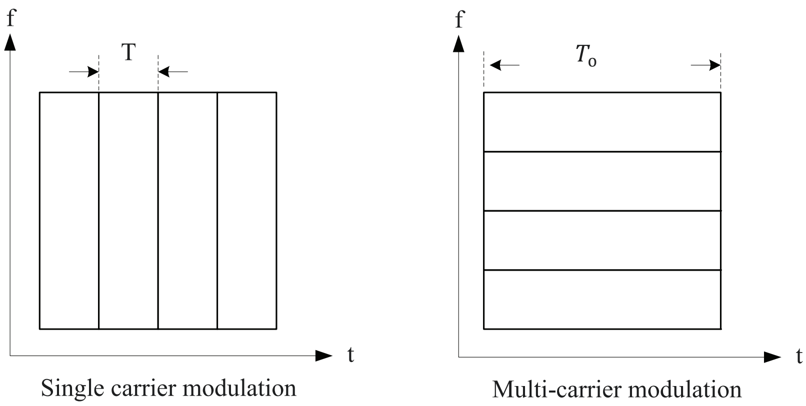

FIGURE 2.10: Single carrier and multi-carrier system over time and frequency

Thus, the transmitted complex base-band signal in the time discrete representation can be denoted as in [67] by

$$s[k] = \sum_{l=0}^{L-1} s_l[k] = \sum_{l=0}^{L-1} \sum_{n} S_l[n] \cdot g_l[k - nL] \tag{2.11}$$

from L substream signals

$$s_l[k] := \sum_n S_l[n] \cdot g_l[k - nL], \tag{2.12}$$

where k is the time discrete index, $S_l[n]$ is the n-th complex data symbol of the l-th subcarrier that formed by the serial to parallel conversion, n is the time discrete index of the reduced symbol rate ($\frac{1}{L \cdot T_o}$), and $g_l[k]$ is the pulse shaping function of the l-th subcarrier, which in OFDM modulation for complex base-band model is defined as

$$g_l[k] = p[k] \cdot \exp(2j\pi f_l T k), \tag{2.13}$$

where $f_l = \frac{l}{T_o}$, and $p[k]$ is a prototype filter defined as

$$p[k] = \begin{cases} \frac{1}{\sqrt{L}} : k = 0, 1, ..., L-1 \\ 0 \quad : \qquad \text{otherwise.} \end{cases} \tag{2.14}$$

It can be realized that the complex signal $s[k]$ of L substream signals $s_l[k]$ are orthogonal to each other. This property allows the parallel transmission of L data streams. The above idea would need L modulators/demodulators, which can be practically implemented via the discrete Fourier transform (DFT) and its inverse (IDFT). The efficient implementation of these two high computational operations would practically realized via FFT and its inverse IFFT.

Cyclic prefix

Applying the FFT results in destroying the orthogonality of the received signal which leads to inter carrier interference (ICI). To maintain orthogonality, the convolution with the channel has to be circular convolution (with only L samples at the receiver output). In order to make the linear convolution pretends to be a circular one, the rear samples (in each OFDM time symbol) have to be copied in front of the time symbol as a cyclic prefix (CP) in time, where $L_{cp} \geq P$; L_{cp} is the length of CP and P is the path delay. As a consequence, the ISI can only affect the corresponding CP part of the received signal, while the data part of the OFDM symbol are not affected as shown in Fig. 2.11. On the other side, the cyclic prefix has also disadvantages. It reduces the bandwidth efficiency and wastes transmit power as this extension does not carry any non-redundant information.

Using this principle, the OFDM symbol duration will be extended from L to $L + L_{cp}$ and the pulse shaping function presented in (2.13) will be modified in the time discrete as

$$\acute{g}_l[k] = \begin{cases} \frac{1}{\sqrt{L}} e^{j\frac{2\pi}{L} l (k - L_{cp})} : & k = 0, 1, ..., L + L_{cp} - 1 \\ 0 : & \text{otherwise.} \end{cases} \tag{2.15}$$

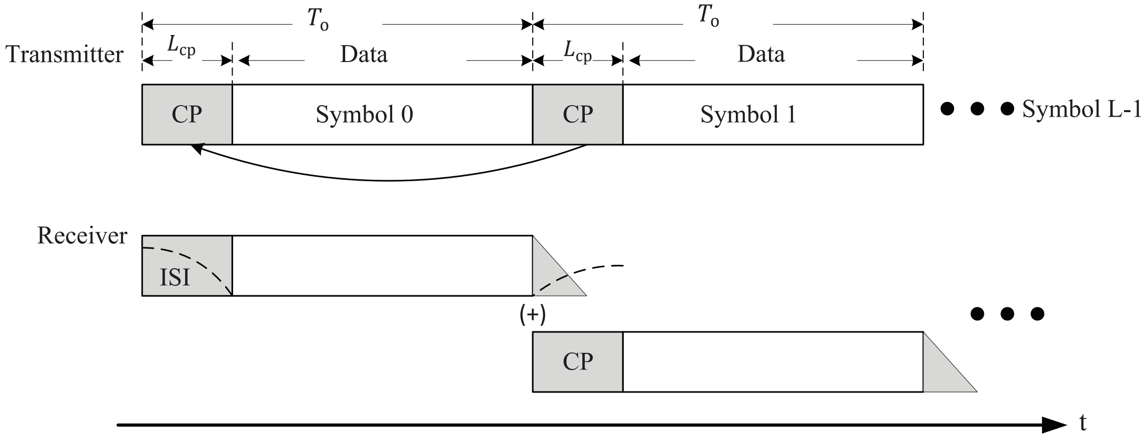

FIGURE 2.11: Advantages of using CP in OFDM

The so-called side-lobes are unwanted and are referred to as out of band radiation. This radiation can be reduced by proper windowing at the transmitter as described in IEEE 1901.2 [68]. The window function is applied to each OFDM symbol separately. This function can be chosen freely based on the out-of-band emission requirements.

The presented investigation of OFDM transmission system are going to be implemented for different NB-PLC standards which allows the evaluation of the PLC system performance.

2.5 Standardization and PLC Systems

The diversity of grid contexts and application domains to which PLC systems can be applied has naturally led to a large ecosystem of specifications, many of those have been adopted by standards developing organization (SDO). In this section, an overview of the available NB-PLC standards for smart grid applications is presented.

Two generations have been developed. The first generation systems are narrowband with low data rate (few hundreds of bps to a few kbps) operating in frequencies up to 500 kHz. These technologies are investigated in details in [69]. Representative standards include x10 [70], KNX (ISO/IEC14543-3-5) [71], and LonWorks® (ISO/IEC14908-3) [72]. They are mainly used for in-home and building automation, controlling, and communication between applications.

Due to the wide demands for an effective smart grid infrastructure [73], the second generation has been driven using OFDM to achieve higher data rates. Within this context, a data rate of tens to hundreds of kbps is achieved using the 3–500 kHz frequency band. An overview of the development of the major industry standardization and specifications for such high data rate NB-PLC systems is provided in Table 2.1. These standards specified for working over low-voltage networks and adapted according to the frequency bands available in different regions of the world (see Fig. 1.2), defining different band plans.

Several organizations started standardizing a new generation of PLC systems operating at narrowband frequencies. In 2011, the international telecommunication union - telecommunication sector (ITU-T) published recommendations, ITU-T G.9955 for the physical layer (PHY) and ITU-T G.9956 for the link layer, which included PRIME and G3-PLC as well as the G.hnem technology [74]. Basically, three separated NB-PLC standards are developed and approved, namely, ITU-T G.9904 (PRIME) [75], ITU-T G.9903 (G3-PLC) [76], and IEEE 1901.2-2013 [68]. These standards have similarities at the physical layer but differentiate in the upper layers supporting. They used differential modulation which avoids the need for channel estimation. Moreover, a convolutional coding is used with an additional repetition coding for robust mode, while G3-PLC and IEEE 1901.2 adds a Reed-Solomon (RS) code. Furthermore, there are common technical properties between G3-PLC and IEEE 1901.2, since the IEEE 1901.2 PLC standard is based on G3-PLC standard.

The influence of the channel access impedance on PLC devices based on PRIME and IEEE 1901.2 will be studied in Chapter 3 and 7. These standards are investigated in details in [53].

2.6 Conclusion

This chapter has introduced an overview of NB-PLC, considering different aspects. The NB-PLC channel modeling and characteristics are presented. The general NB-PLC system structure is described with respect to the physical layer of PLC transmitters and receivers. The OFDM transmission technique of NB-PLC systems is discussed. The available NB-PLC standards and technologies are also summarized.

The presented NB-PLC aspects have provided the essential basis to investigate the effects of the access impedance on NB-PLC systems.

Table 2.1: Time line for the development of NB-PLC standardization

PRIME/G3-PLC	ITU-T	IEEE
Feb. 2008 PRIME specification made public		
May 2009 PRIME Alliance established		
Aug. 2009 G3-PLC specification made public		
	Jan. 2010 ITU G.hnem Start of project	
		Mar. 2010 IEEE 1901.2 Authorization of project
		Jan. 2011 IEEE 1901.2 First draft
Sep. 2011 G3-PLC Alliance established		
	Dec. 2011 ITU-T G.9955 (PHY) ITU-T G.9956 (DLL) G3-PLC & PRIME as annexes	
	Oct. 2012 ITU-T publishes G.9902 (G.hnem) G.9903 (G3-PLC) G.9904 (PRIME)	
		Dec. 2013 IEEE 1901.2 Publication

Chapter 3

Access Impedance of PLC Channel

It is well known that NB-PLC systems for frequencies up to 500 kHz are subject to disturbing channel conditions. The power line channel at narrowband frequencies is characterized by time- and frequency-dependent interference, frequency selective attenuation, and low access impedances. It depends basically on electrical properties of loads at the power grid and in particular at customer buildings. This dependency is a major source of time and frequency variation of the power line channel, which makes the design of a reliable NB-PLC system a challenging task. In this chapter, the influence of low access impedances on NB-PLC applications with limited power consumption will be investigated in terms of the achievable data rate. The coexistence between NB-PLC applications will be also discussed considering the impedance problem of these applications on the transmission system.

3.1 Introduction

NB-PLC technologies are becoming more and more popular. They are frequently used within smart grid applications due to its relatively large coverage. However, the NB-PLC channel exhibits highly dynamic unpredictable characteristics caused by plugging in or turning on/off devices that are connected to the grid. Beyond noise scenarios and frequency selective attenuation, the access impedance of the power line channel is a crucial factor. It is mostly described by frequency selective and time-variant behavior along the transmission frequency range. Therefore, PLC developers must have a good understanding of the access impedance characteristics to design efficient applications in those channel conditions.

The access impedance in narrowband frequencies is strongly related to the connected load equipment to the power grid, while it is dominated by the characteristic impedance of lines in boradband frequencies. Due to the new energy efficiency regulations, the number of switching-mode power supplies has been increased. Hence, the access impedance behavior is extremely changed and is not consistent anymore with the assumed impedance by the EN 50065-1 [8], Fig. 1.5. In particular, access impedances have been observed to be below 1Ω at NB frequencies [14].

Moreover, the PLC transmitter as a modem has the task to inject a voltage into the mains that has to meet the amplitude limits specified in the EN 50065-1 [8]. Therefore, the required transmission power directly depends on the access impedance. The smaller the impedance, the more power is required. In fact, with an impedance less than 1Ω, the injection of a significant signal amplitude causes a large effort due to the reduction of the output voltage level. As a consequence, the transmitted voltage level has to be adapted to match the actual impedances on the power grid.

This chapter is organized as follows: A study about the influence of the low access impedance on the performance of NB-PLC systems is presented in Section 3.2. The physical channel model of PLC is simplified focusing on the access impedance. The achievable data rate by PLC systems is calculated as a performance factor, taking into account the power consumption limitation of the transmitter modem. Furthermore, the coexistence problem caused by changing the impedance values of smart grid applications between transmitting and receiving in different frequency bands is investigated in Section 3.3. Possible solutions to overcome this problem are also introduced.

3.2 PLC Channel Performance

The practical design of the PLC grid is to connect the transmitter and receiver devices to the power network at any socket by means of coupling circuits. Data transmission is always set up between two different connected points. Therefore, the connection between any two access points presents a communication channel that has to be evaluated. To estimate the performance of the PLC channel, the achievable data rate is considered in this section as in [77], [78].

3.2.1 Description of the communication of PLC transmitters

Fig. 3.1 presents a simplified schematic model of the presented one in Fig. 2.6 that describes NB-PLC transmission systems. It can be realized that this model covers the same features as the theoretical model in Fig. 2.5, but extends the channel model by the access impedance $Z_A(t, f)$. This impedance is presented in parallel to the power output stage of a PLC modem at the transmitter side by the mains grid. It is mostly dependent on the load equipment that are connected very close to the PLC modem and takes into account the influence of other loads that are also connected in parallel to the same transmission line. Since the modulus of this impedance can be challenged low, especially at narrowband frequencies, the correct design of a modem's power output level states a crucial design requirement.

The physical signal parameters are presented in Fig. 3.1 in the frequency domain to simplify the analysis of the communication system. However, some signal parameters are also time-variant in the frequency domain and thus are time- and frequency-variant.

The simplified PLC transmitter is described by the signal generator at the channel frequency $U_g(f)$, an automatic gain control (AGC), the supply voltage of the power amplifier (PA) U_{amp}, and the internal impedance of the transmitter which simplified by the resistor $R_g(f)$. The coupling circuit is not denoted since its influence is taken into account of the internal impedance R_g. The integrated power amplifier (PA) provides the output signal of

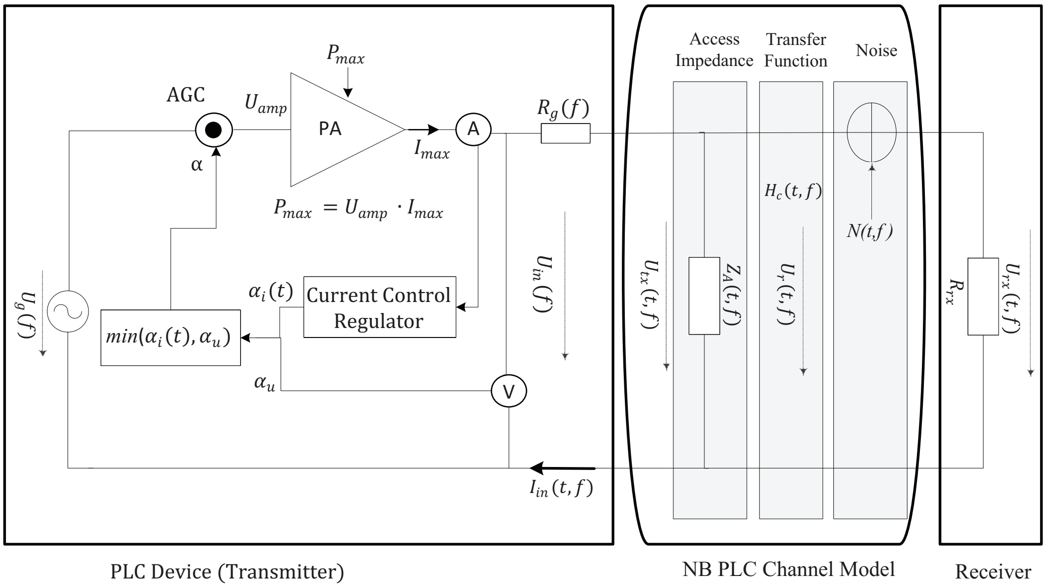

FIGURE 3.1: Simplified NB-PLC transmission system

the transmitter corresponding to the impedance amount on the grid. The output voltage level of the PA is determined using a multiplication factor α based on voltage and current measurements. The factor α is defined as $\alpha = min(\alpha_i(t), \alpha_u)$, where the factor α_u is a constant, while the factor $\alpha_i(t)$ results from the current measurements and will be defined later. The voltage $U_{in}(f)$ represents the voltage at the output of the PLC transmitter. The current $I_{in}(t, f)$ represents the flowing current at the transmitter and the PLC channel. The transmitted signal $U_{tx}(t, f)$ and the current $I_{in}(t, f)$ are time- and frequency-variant and directly affected by the low impedances on the power line. The attenuated signal by the transfer function $H_c(t, f)$ is represented as $U_r(t, f)$ and the signal after the additive noise as $U_n(t, f)$. The received signal at the receiver is represented by the voltage $U_{rx}(t, f)$.

The behavior of the PA output level with respect to the load impedance is described in Fig. 3.2. The requested PA output voltage level is kept constant using the multiplication α_u until the impedance goes under a limit corresponding to the current limit. If the current limit is reached, the PA output voltage level is decreased linearly using $\alpha_i(t)$ factor until the output current is again under the threshold value. Thus, the current is constant in the current control area. This behavior of the output level of the PA leads to a reduction in the transmitted signal and the performance of the PLC systems.

3.2.2 Analysis model

The transmitted signal $U_{tx}(t, f)$ and the current $I_{in}(t, f)$ are time- and frequency-variant and are directly affected by the low impedances on the power line. The calculation of these parameters in context of the multiplication factor α is investigated in the following with respect to the model presented in Fig. 3.1.

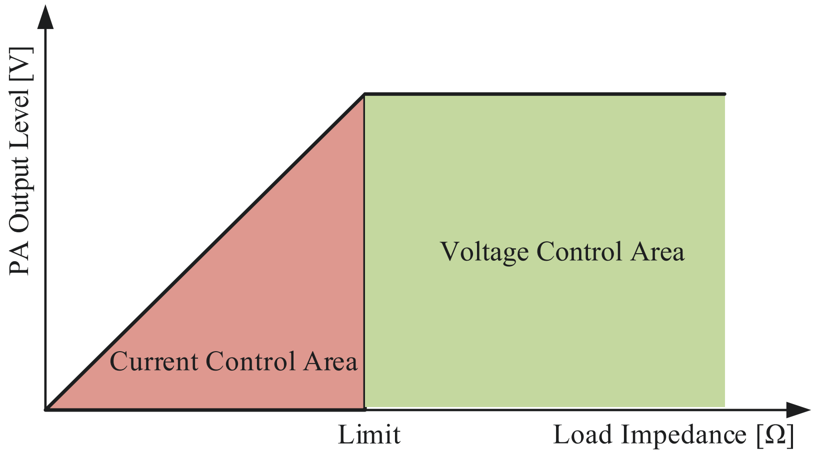

FIGURE 3.2: PA output voltage level vs. load impedance [79]

The relation between the transmitted signal and the received signal in the frequency domain is described as in (2.10) by

$$U_{rx}(t,f) = \underbrace{U_{tx}(t,f) \cdot H_c(t,f)}_{U_r(t,f)} + U_n(t,f). \tag{3.1}$$

In the presented model (3.1), the PLC channel is considered as time- and frequency-variant. Since the channel transfer function $H_c(t,f)$ can be estimated from snapshots of the LTI channel response at different instants of the mains cycle [2], we can usually assume that the channel remains constant during a single OFDM symbol. This assumption is reasonable, since in high-speed data transmissions, the PLC channels vary rather slowly. Furthermore, in contrast to wireless multipath channels, the multipath effect of PLC channels can be analytically calculated [80] with the aid of the channel transfer function between any two outlets. Therefore, the time variance of the channel can be presented by $t := k \cdot T_o$ where k is the OFDM symbol time index and T_o is the duration of the OFDM symbol. Similarly, the frequency dependency of the channel can be represented as $f := l \cdot f_{sub}$, where l is the subcarrier index and f_{sub} is the subcarrier spacing which is given as $f_{sub} = 1/T_d$, where T_d is the duration of the data part of an OFDM symbol. As a consequence, the formula given in (3.1) can be rewritten as

$$U_{rx}[k,l] = \underbrace{U_{tx}[k,l] \cdot H_c[k,l]}_{U_r[k,l]} + U_n[k,l]. \tag{3.2}$$

For each subcarrier l, the transmitted signal U_{tx} can be computed as

$$U_{tx}[k,l] = I_{in}[k,l] \cdot Z_A[k,l]. \tag{3.3}$$

The frequency-dependent current $I_{in}[k,l]$ is calculated as

$$I_{in}[k,l] = \frac{U_{in}[l]}{(R_g[l] + Z_A[k,l])}, \tag{3.4}$$

and it is neglectable at the receiver side because of the high impedance R_{rx}.

The voltage at the output of the PLC transmitter $U_{in}[l]$ is computed as

$$U_{in}[l] = U_g[l] \cdot \alpha. \tag{3.5}$$

The determination of the multiplication factor α is related to the voltage and current measurements as:

- If $\alpha_i[k] \geq \alpha_u$, then $\alpha = \alpha_u$ and the output voltage of the PA is defined using the constant α_u to fulfill the voltage level of the EN 50065-1. This case represents the normal transmission where the access impedance value is above the limit.

- If $\alpha_i[k] < \alpha_u$, then $\alpha = \alpha_i[k]$ and the current control regulator defines the output voltage of the PA. This case represents the interesting situation where the access impedance $Z_A[k,l]$ is very low and affects the transmission performance. The factor $\alpha_i[k]$ is determined as

$$\alpha_i[k] = \frac{I_{max}}{I_{total}}, \tag{3.6}$$

where I_{max} is the maximum current flowing via the PA and defined as $I_{max} = \frac{P_{max}}{U_{amp}}$, and the current I_{total} is the average value of the sum of the superimposition of individual subcarriers, i.e. the squares of the effective values of the currents are added as

$$I_{total} = \sqrt{\sum_l I_{in}[k,l]^2}. \tag{3.7}$$

By substituting (3.5) in (3.4) & (3.4) in (3.7)

$$I_{total} = \alpha_i[k] \cdot \sqrt{\sum_l \left(\frac{U_g[l]}{R_g[l] + Z_A[k,l]}\right)^2}. \tag{3.8}$$

The voltage U_{in} can be found by substituting (3.8) in (3.6) & (3.6) in (3.5) as

$$U_{in}[l] = \frac{I_{max}}{\sqrt{\sum_l \left(\frac{U_g[l]}{R_g[l]+Z_A[k,l]}\right)^2}} \cdot U_g[l]. \tag{3.9}$$

Thus, the signal $U_r[k,l]$ can be found starting from the generator voltage by substituting (3.9) in (3.4) & (3.4) in (3.3) as

$$U_r[k,l] = H_c[k,l] \cdot \frac{I_{max} \cdot Z_A[k,l]}{\sqrt{\sum_l \left(\frac{U_g[l]}{R_g[l]+Z_A[k,l]}\right)^2 \cdot (R_g[l] + Z_A[k,l])}} \cdot U_g[l]. \tag{3.10}$$

Based on the presented PLC channel model, the performance of OFDM NB-PLC systems will be evaluated for different access impedance values.

3.2.3 Data rate calculation

To evaluate the PLC transmission system, the data rate is investigated as a performance factor. The data rate is calculated over all subcarriers in the OFDM system for different access impedances. The maximum achievable data rate is computed based on the Shannon's theorem of a noisy channel with the bandwidth f_{sub} and the signal power to the noise power ratio.

The achievable data rate is estimated with an extra margin of 2dB which accounts for the variability in the SNR measurement. This margin is necessary due to the fact that the code used in reality is worse in performance than the Shannon theoretical limit.

The achievable data rate R is given as

$$R[l] = \sum_k f_{sub} \cdot log_2(1 + (SNR)[k,l] \cdot 10^{\frac{-2dB}{10}}). \tag{3.11}$$

For each subcarrier, the (SNR) is calculated as

$$(SNR)[k,l] = \frac{U_r^2[k,l]}{U_n^2[k,l]}. \tag{3.12}$$

From (3.12), the achievable data rate R can be completely found based on (3.10) as

$$\begin{aligned} R[l] = \textstyle\sum_k f_{sub} \cdot log_2\Big(1 + (H_c[k,l] \cdot \frac{I_{max} \cdot Z_A[k,l]}{\sqrt{\sum_l (\frac{U_g[l]}{R_g[l]+Z_A[k,l]})^2 \cdot (R_g[l]+Z_A[k,l])}} \cdot \\ U_g[l])^2 \cdot \frac{1}{U_n[k,l]^2} \cdot 10^{\frac{-2dB}{10}}\Big). \end{aligned} \tag{3.13}$$

From (3.13), it can be realized that all parameters in the mathematical model are known and the data rate is dependent on the access impedance values. Therefore, the achievable data rate R will be calculated for different access impedance values to analyze its influence on the transmission.

3.2.4 Evaluation by simulation

For the evaluation, the simulation environment considers already done PLC channel measurements. The simulation parameters are given as in [77], [78] and described in the following:

- PRIME Standard:

We consider the transmitted signal by a PLC device with respect to the PRIME standard. The simulation results can be equivalently considered by other PLC standards. The detailed physical layer specification of PRIME is described in [75]. The transmitted signal is located in the range of 42-89 kHz. The FFT size of PRIME is 512 and the subcarrier spacing is 488 Hz. The number of the used subcarriers is 97.

- Transmitter parameters:

  The transmitter circuit parameters are related to the analog front end AFE031 of Texas Instrument and conform the EN50065-1 CENELEC A-band [81]. The voltage U_{amp} is selected to be 10V and the current output of the amplifier is limited to 1.5A. Thus, the power of the amplifier is limited to 15W (10×1.5). The internal impedance R_g is assumed to be 2Ω.

- Channel parameters:

  The achievable data rate is compared for different access impedance measurements with respect to the frequency. First, Z_A is related to the EN50065-1 as shown in Fig. 1.5. Second, Z_A is based on measurements were done by Dostert [28] and shown in Fig. 3.3. Third, Z_A is based on measurements were done by China electrical power research institute (CEPRI) [25], and shown in Fig. 3.4, phase B-N. Finally, Z_A is based on measurements were done in Austria [82] as shown in Fig. 3.5, phase 1 & 3. All these measurements show low access impedance values in the CENELEC A-band.

  In order to realize a realistic simulation environment, the channel attenuation, and the noise are based on the measured values by CEPRI [25], as shown in Fig. 3.6, 26# (L=250m) and Fig. 3.7, phase A-N, respectively. The measured noise power spectrum $U_{n,me}$ in bandwidth of 10 kHz is implemented to fulfill our simulation model as

$$U_n[k,l] = \sqrt{\frac{f_{sub}}{10 \times 10^3}} \cdot U_{n,me}[l]. \tag{3.14}$$

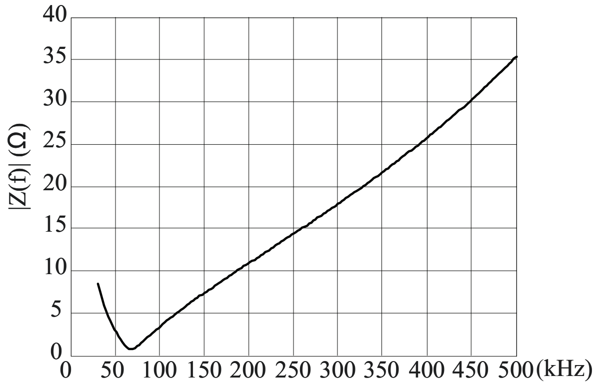

FIGURE 3.3: Access impedance measurement by Dostert

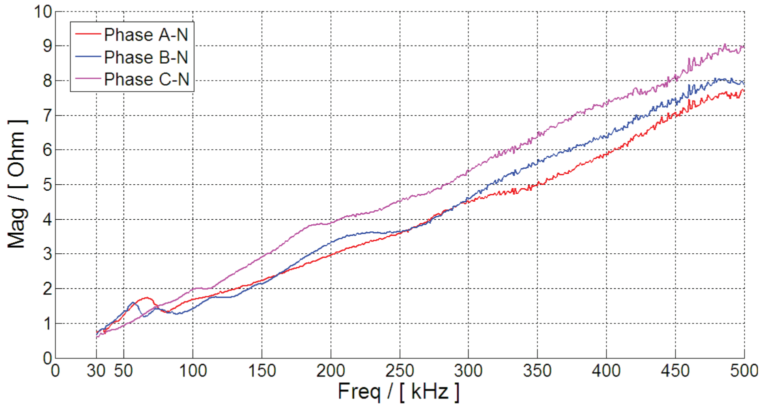

FIGURE 3.4: Access impedance measurement in China- Phase B-N

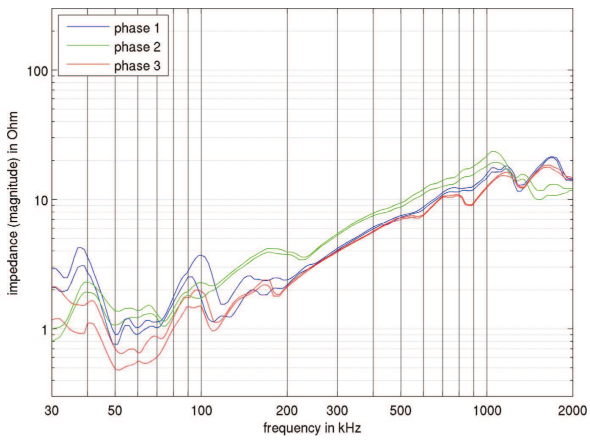

FIGURE 3.5: Access impedance measurement in Austria- Phase 1 & 3

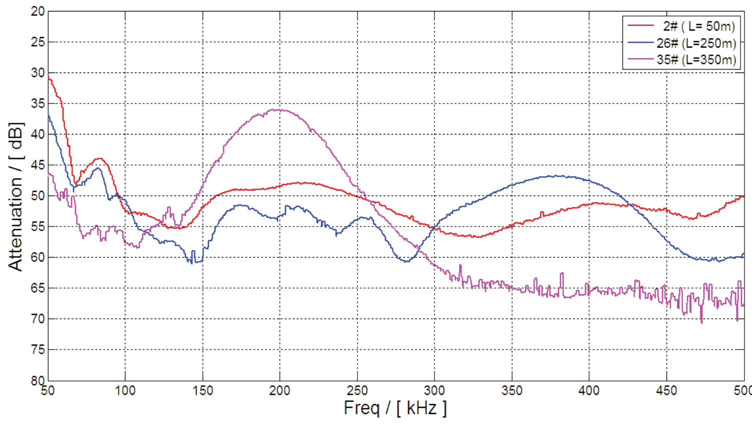

FIGURE 3.6: Attenuation measurement in China- 26# (L=250m)

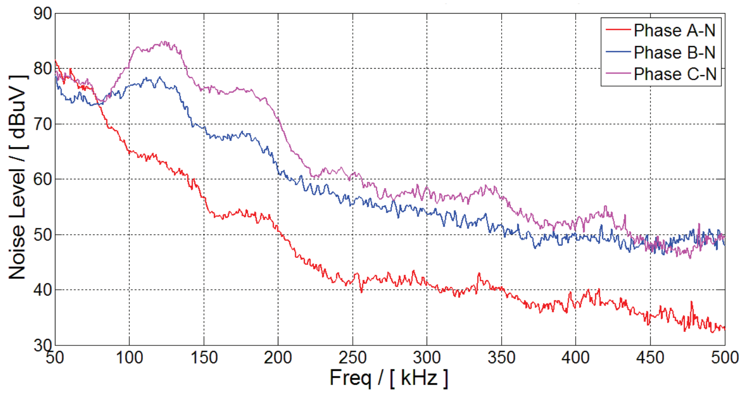

FIGURE 3.7: Noise power spectrum measurement in China- Phase A-N

Evaluation results

The maximum achievable data rate related to the model in (3.13), for the presented simulation parameters in this section is shown in Fig. 3.8. The simulation results show that the access impedance affects the transmission system by reducing the data rate from 41.73 kbps in the case of impedance based on EN50065-1 to 19.61 kbps, 16.41 kbps, 9.04 kbps and 4.21 kbps for access impedances measured by Dostert, in China, and in Austria, respectively. The data rate reduction amount is between 55 to 90% for the different impedance values. It has been observed that the data rate calculation in the case of Z_A based on EN 50065-1 is dependent on α_u and for low access impedance values is dependent on $\alpha_i[k]$.

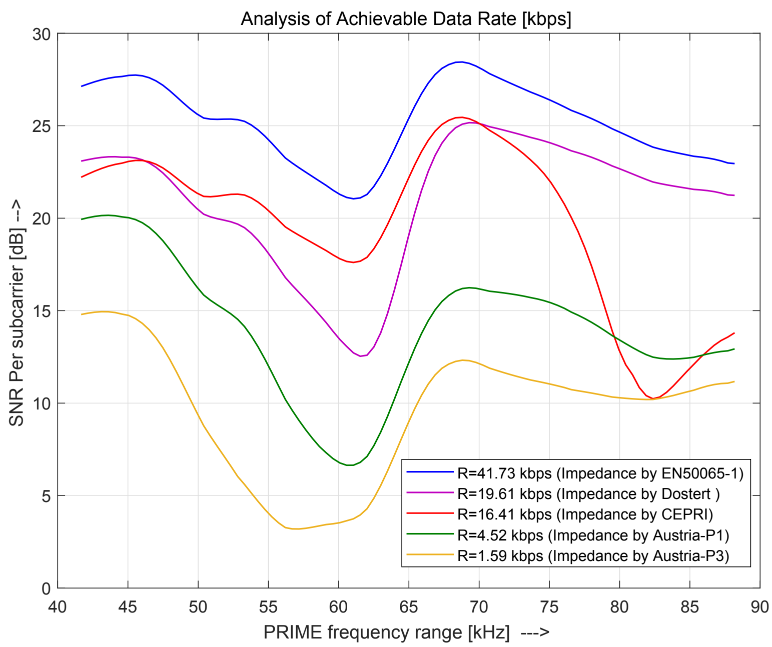

FIGURE 3.8: The achievable data rate of PLC channel for different access impedances

TABLE 3.1: Simulation results for a transmitter in case of low access impedances

$Z_A[\Omega]$	I_{total} [A]	$U_{tx,eff}$ [dBµV]	$P_{in,eff}$ [W]	$P_{tx,eff}$ [W]	R [kbps]
EN50065-1	0.32	133.9	1.63	1.57	41.73
Dostert	1.5	130.2	5.71	3.2	19.61
CEPRI	1.5	129.2	5.11	2.86	16.41
Austria- P1	1.5	126.4	5.10	2.85	9.04
Austria- P3	1.5	123.2	4.24	1.99	4.21

Table 3.1 describes the total current at the transmitter I_{total}, the effective voltage at the output of the transmitter $U_{tx,eff}$ calculated as $\sqrt{\sum_k (U_{tx}[k,l])^2}$, the effective power at the output of the generator $P_{in,eff}$ calculated as $\sum_k |U_{in}[l] \cdot I_{in}[k,l]|$, the effective power at the output of the transmitter $P_{tx,eff}$ calculated as $\sum_k |U_{tx}[k,l] \cdot I_{in}[k,l]|$, and the achievable data rate over all subcarriers for the different values of Z_A. From Table 3.1, we can see that the effective current always reach the limit in case of low access impedance values. The effective voltage at the output of the transmitter conform the level in the EN 50065-1 (134 dBµV) and reduced for the other cases. Moreover, the power requirement for the power amplifier $P_{in,eff}$ is very high in the case of the low access impedance. However, the transmitted power is only between 45 to 55% of the consumed power.

In the next chapters, the access impedance is going to be measured in the laboratory to evaluate its influence on different PLC technologies. Moreover, an optimization method to improve the achievable data rate in the case of low access impedances is going to be introduced.

3.3 Coexistence Analysis of Impedance Modulating Transmitters

Regulation bodies in narrowband frequencies such as CENELEC and FCC do not provide channel access mechanisms in all bands. Carrier sense multiple access with collision avoidance mechanism is only applied for CENELEC C-band and does not work when non-interoperable applications operate on the same wire. Thus, it is necessary to present an additional mechanism for the other frequency bands.

We have seen that the access impedance reduces the transmitted signal and the achievable data rate of PLC systems. An additional problem caused by the low impedance is the coexistence on the physical layer when different PLC applications operate on different CENELEC bands irrespectively of the medium access control coexistence mechanisms [83]. This problem will be investigated in this section based on LTspice simulation.

3.3.1 Measurement circuit

In literature, the methods used to simulate and study the transmission line behavior are discussed in [84]. They are obtained from the time-dependent equations [85] which are for the elementary line transmission cell, where R, L, G and C are per unit length resistance (Ω/m), inductance (H/m), conductance (S/m), and capacitance (F/m), respectively.

Fig. 3.9 shows the simplified transmission model of PLC applications in context of the transmission line theory. The voltage $u_g(t)$ represents the signal generator. The transmission line is presented by the complex impedances Z_1 and Z_2 that represent R, L and G, C, respectively. The resistor R_g represents the simplified internal impedance of the transmitter circuit and $Z_A(t)$ is the complex time-variant access impedance at the output of the transmitter. The PLC application that represents the transmitter circuit could be any smart energy consumption application that changes its impedance suddenly with respect to the time by turning it on and off. The voltages $u_{tx}(t)$ and $u_{rx}(t)$ denote the instantaneous voltages at the transmitter and the receiver. The receiver is simplified as in Fig. 2.6 by the impedance R_{rx} that is assumed to be high.

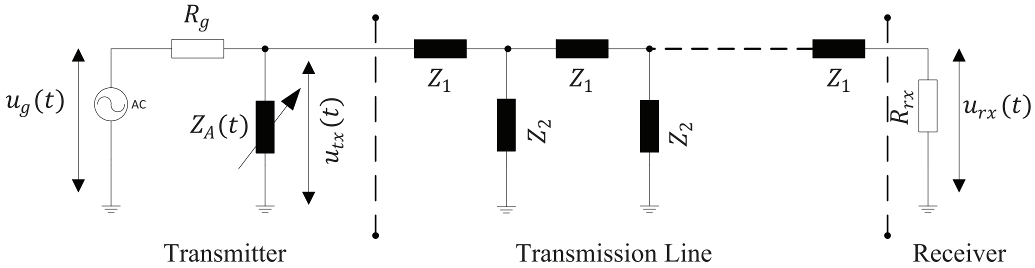

FIGURE 3.9: Simplified transmission model of PLC applications

Based on the transmission model shown in Fig. 3.9 and the linear time-invariant (LTI) system theory, the relation between the transmitter and receiver voltage is given as

$$\frac{u_{tx}(t)}{u_{rx}(t)} = \text{constant}. \tag{3.15}$$

From (3.15), we can realize that the linear behavior of the channel between the transmitter and the receiver should be kept. However, the time-variant access impedance $Z_A(t)$ in parallel to the transmitter circuit can cause a non-linear behavior. Hence, the transmitter voltage can be calculated as

$$u_{tx}(t) = \frac{Z_A(t)}{R_g + Z_A(t)} \cdot u_g(t). \tag{3.16}$$

From (3.16), we can see that the voltage at the transmitter side depends on the transmitter circuit and the changeable access impedance on the PLC channel. As a result, in order to get the same generated signal $u_g(t)$ at the transmitter side $u_{tx}(t)$ that satisfies the linear behavior of the system, the impedance R_g must be very small or in the optimal case equal to zero. Therefore, we present a simulation model for two transmitters connected to the same power line and then discuss the simulation results.

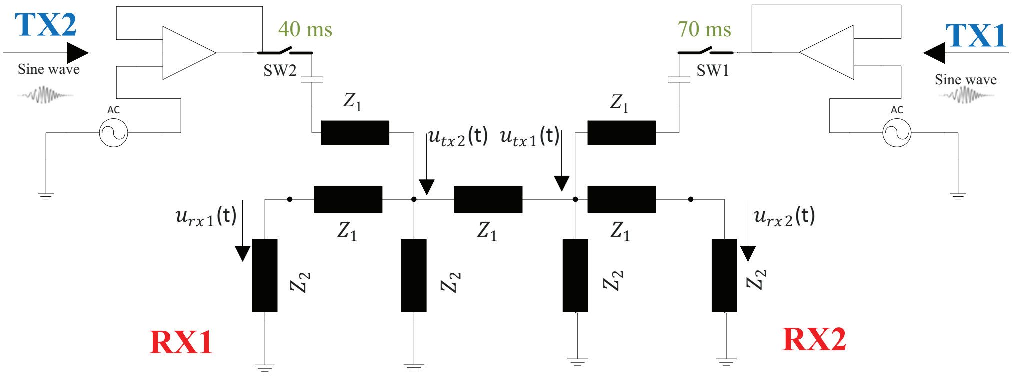

FIGURE 3.10: Measurement circuit for two transmitters on the power line

The measurement model is based on LTspice simulation and described in Fig. 3.10. This model of the power line transmission circuit is related to the principle of the total voltages and currents rather than network characterization. The frequency range of the measurement is related to the CENELEC bands, between 3 kHz and 148.5 kHz. In the measurement circuit, two signal generators with a power amplifier are representing the two transmitters TX1 and TX2, and are responsible for sending the signal to the power line. Two switches (SW1 and SW2) are applied to control the transmitters and to measure the signal at specific time slots; where the switch SW1 of TX1 has a delay of 70 ms and the switch SW2 of TX2 has a delay of 40 ms. The transmission line is represented as in Fig. 3.9. An AC multivoltmeter is used to measure the values of the voltages: $u_{tx1}(t)$, $u_{rx1}(t)$, $u_{tx2}(t)$, and $u_{rx2}(t)$ as shown in the circuit diagram. The voltages $u_{tx1}(t)$ and $u_{tx2}(t)$ represent the transmitted signals before crossing over the shared medium by TX1 and TX2, respectively, where the voltages $u_{rx1}(t)$ and $u_{rx2}(t)$ represent the received signals by the receivers RX1 and RX2, respectively. The resistor element in the complex impedance Z_1 is set too small equal to 1Ω.

This model represents a typical scenario of two different signals that exist on the electrical power line network from two different transmitters. Assuming the two transmitters are different power line applications that use different frequency bands, the simulation results will show the problem of the coexistence between power line applications in practice.

3.3.2 Measurement results

For the simulation test, the frequency of TX1 is set to 110 kHz that is related to the CENELEC B-band and the transmitted signal voltage is 0V. The frequency of TX2 is set to 60 kHz that is related to the CENELEC A-band and the transmitted voltage is 1V.

Fig. 3.11 shows the simulation results for the second transmitter TX2 during time slots of TX2 when the switch SW2 is opened and closed. The transmission problem can be seen where the transmitted signal $u_{tx2}(t)$ is extremely reduced and disappeared due to the low impedance. Thus, it cannot be correctly received by RX2.

Fig. 3.12 shows the simulation results for the first transmitter TX1 during the time slots of TX1 and TX2 when the two switches SW1 and SW2 are opened and closed. It can be seen that the transmitted signal $u_{tx1}(t)$ interfered with the transmitted signal $u_{tx2}(t)$ and appeared in RX1 when the second switch (SW2) is closed.

These simulation results show the problem of using the power line medium from two different PLC applications, where the transmitted signal from TX2 attenuated and absorbed before reaching the receiver RX2, and the transmitted signal from TX1 influenced and interfered with the transmitted signal TX2 when the second switch (SW2) is closed. These signal degradations is caused by the small impedance value at the transmitter in addition to the time-variant behavior of the connected devices to the power network. It has been shown that the medium conditions change, when applications transmit and receive, and switch on and off on the power line medium. As a consequence, the different power line technologies cannot work together and independently from each other because of the impedance requirements at the transmitter side.

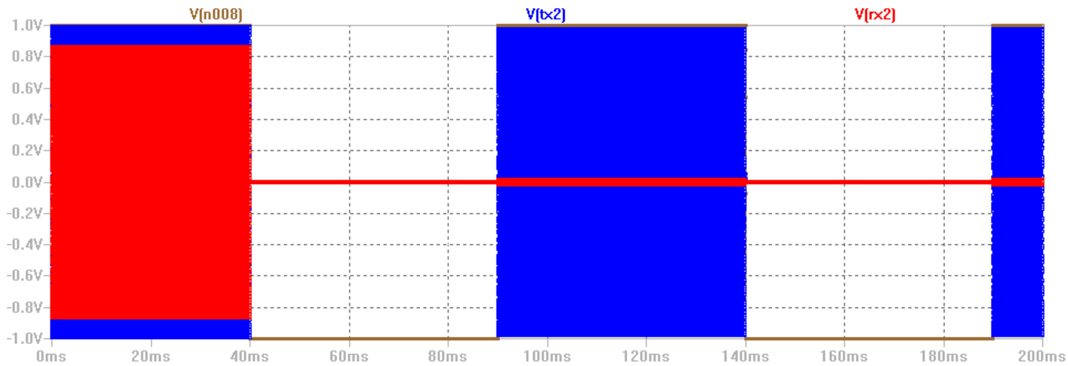

FIGURE 3.11: The transmitted signal $u_{tx2}(t)$ and the received signal $u_{rx2}(t)$ [83]

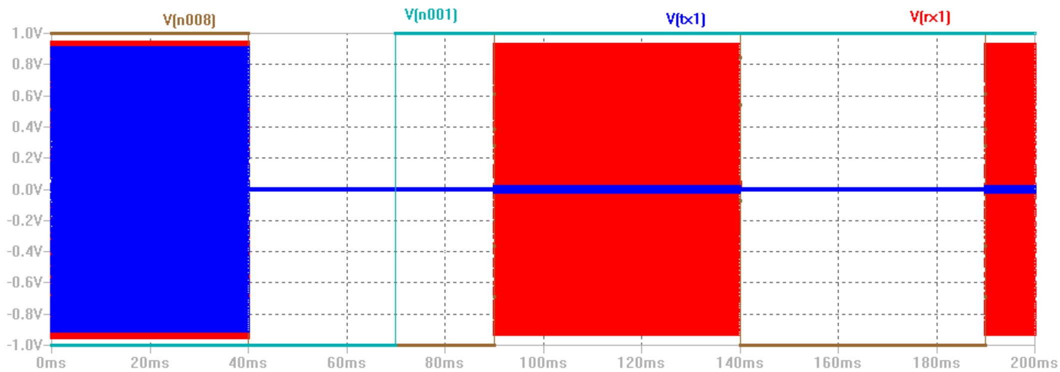

FIGURE 3.12: The transmitted signal $u_{tx1}(t)$ and the received signal $u_{rx1}(t)$ [83]

Table 3.2: Minimum impedance values of smart grid equipment of type-1 in frequency bands from 9-95 kHz related to EN 50065-7:2002 standard

Frequency bands	**3- 9 kHz**		**9- 95 kHz**			**95- 148.5 kHz**	
Operating mode	RX	TX	RX		TX	RX	TX
$\|Z_e\|$	10Ω	Free	Out BW Free	In BW 50Ω	Free	5Ω	3Ω

Table 3.3: Minimum impedance values of smart grid equipment of type-2 in frequency bands from 9-95 kHz related to EN 50065-7:2002 standard

Frequency bands	**3- 9 kHz**		**9- 95 kHz**		**95- 148.5 kHz**	
Operating mode	RX	TX	RX	TX	RX	TX
$\|Z_e\|$	10Ω	10Ω	5Ω	5Ω	5Ω	Free

3.3.3 Possible solutions

EN 50065-7:2002

The problem of the low impedance on the power line can be solved by the old CENELEC standard EN 50065-7:2002 [86], where the input impedance of PLC equipment and applications is specified and restricted. This standard is an active standard and specifies the impedance on the power line when load equipment are plugged on the same wire and operate in different frequency bands, simultaneously.

However, the implementation of the EN 50065-7:2002 standard for the OFDM applications is difficult due to the impedance restriction for each frequency range. For example, the minimum impedance of a transmitter (TX) in frequency bands between 9-95 kHz for equipment of type-1 is given as free, from Table 3.2, but the minimum impedance of an TX in frequency bands between 9-95 kHz for equipment of type-2 is given as 5Ω, from Table 3.3. Therefore, the transmitter impedance values must be restricted to specific values at the given frequency bands for the different equipment types which is very difficult to be implemented, since all PLC technologies develop their equipment irrespectively of the transmitter/receiver input impedance values.

Furthermore, the modification of the analog amplifier of each transmitter node to fulfill the impedance specifications is expensive because of the huge number of nodes and the impossibility to replace it by a software implementation. Therefore, new coexistence requirements, standards, and mechanisms should be considered to overcome the impedance problem and enhance the performance of the power line technologies, since most of the new PLC applications that operate on the CENELEC bands do not consider the impedance requirements addressed by the EN 50065-7:2002 and develop their communication equipment independently.

Operating on different wires

We introduce here a different implementation model of the transmission over the power line for the same transmission scenario shown in Fig. 3.10. A three-phase signal distribution structure is considered. The cable line includes three wires (phases) and neutral wire where each wire is inserted into the insulating sleeve and all wires are insulated with own sheath as shown in Fig. 3.13.

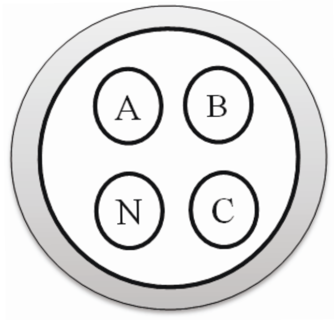

FIGURE 3.13: Cross section of power line [83]

The alternative transmission model is shown in Fig. 3.14. We use the three-phase line described by the three wires L_A, L_B, L_C and neutral wire N instead of transmitting on one wire. Two applications transmitting on different wires of the power line are considered instead of using the same wire. The first transmitter TX1 is allocated on the L_A wire and TX2 on L_B wire. Only two transmitters are implemented to simplify the model. TX1 and TX2 operate on different frequencies of the CENELEC bands. RX1 and RX2 are responsible for receiving the transmitted signal. The capacitive coupling between the wires is used to avoid the interference between the transmitted signals on the different wires. However, parasitic capacitance effects could appear between the parts of the transmission components which becomes a problem for higher frequencies because of the very small distributed capacitances that exist and have lower impedances.

For the LTspice simulation, the transmitted signal $u_{tx1}(t)$ by TX1 is at 110 kHz with 0V amplitude and the transmitted signal $u_{tx2}(t)$ by TX2 is at 60 kHz with 1V amplitude. The capacitances after the transmitters are set to 1µF as implemented in [25] and the other capacities along the cable are given by 1pF.

The simulation result presented in Fig. 3.15 shows how the different smart grid applications that operate on different frequencies can transmit on the power line without affecting the transmitted signal, where the transmitted signal $u_{tx2}(t)$ by TX2 is almost equal to the received signal $u_{rx2}(t)$ by RX2.

From the simulation result in Fig. 3.15, we can conclude that the allocation of different transmitters on different wires of the power line introduces the possibility to solve the impedance problem caused when transmitters with different frequencies transmit on the same wire. The presented model allows the different energy utilities that use the CENELEC A-band to operate together with other PLC applications that use the CENELEC B-band. Therefore, the use of the different wires of the power line from different technologies such as

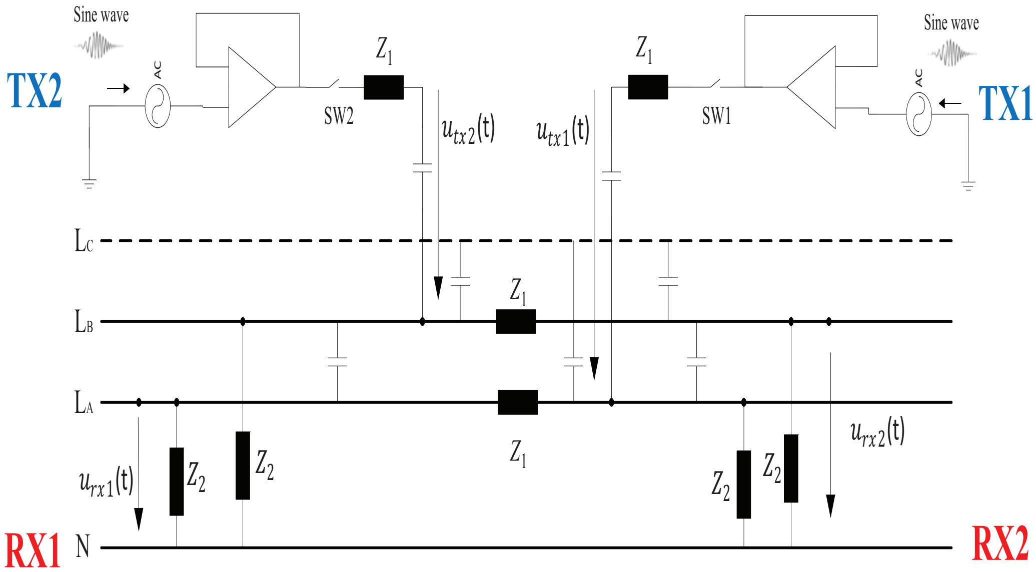

FIGURE 3.14: Transmission circuit of two PLC applications plugged into three-phase cable

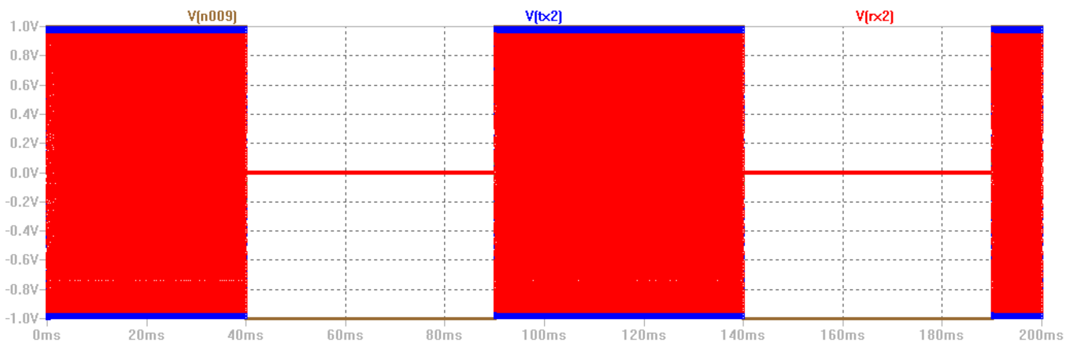

FIGURE 3.15: The transmitted signal $u_{tx2}(t)$ and the received signal $u_{rx2}(t)$ for applications operating on different wires [83]

PRIME and G3-PLC presents a new method and vision to overcome the PLC coexistence problem caused by the low impedance.

3.4 Conclusion

This chapter has presented the influence of the low channel access impedance by reducing the performance of PLC transmission systems based modems with limited power consumption. The achievable data rate of the PLC channel is investigated to evaluate the performance of the PLC systems with respect to the frequency-dependent access impedance. PRIME technology is considered as an example to determine the achievable data rate for different access impedance values. The simulation results showed the effects of the low access impedance of real measurements by decreasing the achievable data rate in amount of up to 90% compared to the assumed impedance by the EN 50065-1.

In addition, the coexistence problem caused by changing the impedance values of the power line between transmitting and receiving state for different smart grid applications is shown. The transmitted signal is disappeared or interfered before reaching the receiver. Two possible solutions to overcome this problem are presented. First, based on the EN 50065-7:2002 standards with defined impedance values for transmit and receive state. Second, by allocating the various PLC applications on different wires.

Chapter 4

Access Impedance Measurement

The precise knowledge of the access impedance on the power line medium enables the optimum design of smart grid applications. The impedance of the PLC channel is strongly affected by the unmatched load impedance and is considered as time- and frequency-dependent. This problem is the main reason of reducing the power amplifier output level of PLC modems and the data rate of the PLC channel. This chapter presents a description of an accurate access impedance measurement system in the frequency range of 30-500 kHz with calibration processes and procedures to remove all parasitic effects that disturb the measurements. This system provides a cancellation of the mains frequency component and enables the analysis of the cyclostationary behavior of the power line access impedance. Off- and online representative impedance measurements on different power outlets will be presented and discussed.

4.1 Introduction

NB-PLC technologies are widely used in smart grid applications, like automated metering infrastructure, controlling and real time analytics, covering the 30-500 kHz frequency band [2], [53]. The power line channel is mostly considered as a harsh environment and presents a highly time-variant behavior. One primary changeable characteristic of the power line channel is the access impedance. This is caused by plugging load equipment into the power grid or turning equipment on and off. Therefore, the accurate measurements of the power line access impedance are an important tool in the development of reliable PLC modems and efficient PLC systems.

Due to the mass adoption of a switched-mode power supply of electrical devices and active power factor correction, the power line impedance characteristic has been changed dramatically. The switching properties of those power supplies show cyclostationary impedance changes and the equipped EMI filters to the power supplies introduce resonances in the frequency bands used for NB-PLC, leading to access impedances lower than 1Ω [14] at some frequencies.

A vector network analyzer (VNA) is generally used with an LISN to measure the network parameters and the impedance between an AC and the device under test (DUT). The VNA is connected to the mains using a coupling circuit. This coupling circuit has to be well characterized and its effects have to be compensated properly. However, there is a huge difference between the expected impedance to be measured and the internal impedance of the VNA which is usually 50Ω. Therefore, we choose a direct measurement of current and voltage with efficient digital signal processing for our measurement system.

Moreover, performing such measurements is problematic since they have to be done under the power of the mains voltage. High-powered disturbances from the power grid cannot be easily separated from the measurement inputs. Standard galvanic isolation procedures either fail at the very low impedances or are not available for this frequency range. Therefore, commercial equipment to measure and analyze the PLC channel impedance and the load impedances on the power grid at specific frequencies is not yet available. Thus, developing and updating of the current measurement systems are needed to deliver accurate impedance measurements.

In this chapter, the existing access impedance measurement system (AIMS) by Sigle *et al.* [14] and Liu [29] has been considered and further developed for accurate impedance measurement results taking into account different error correction steps and another calibration setup. The developed AIMS allows the precise measurements of very low access impedances over time and frequency in operation mode of load equipment for frequencies up to 500 kHz. The applied signal processing has permitted the cancellation of the mains frequency components and all other disturbances on the power line and the synchronization to the zero-crossings to analyze the cyclostationary behavior of the measured impedances [87], [88].

This chapter is organized as follows: The access impedance measurement system is described in details in Section 4.2, including objectives and specifications. The used signal processing for errors correction is presented in Section 4.3. The integral time of the Fourier series calculation is optimized in Section 4.4. A comparison between different calibration setups is introduced in Section 4.5. The measurement results are discussed for online access impedances at different power outlets in a laboratory in Section 4.6. Finally, the chapter is concluded in Section 4.7.

4.2 Access Impedance Measurement System Description

Measuring and analyzing the access impedance behavior is necessary for further development of PLC applications. In this section, the AIMS will be described with its objectives and specifications.

4.2.1 Objectives and specifications of the measurement system

The objective of the measurement system is to measure the access impedance of the low-voltage power grid in the range of 30–500 kHz. This frequency range is related to the currently available PLC standards and technologies presented in [53]. The access impedance is characterized by frequency-dependent resonances, below 1Ω, and cyclostationary behavior over time synchronous to the mains frequency (50 or 60 Hz). This behavior is only measurable during regular operation, which means that the mains frequency component and all disturbances on the power line are included. The combination of very low impedances and the selected frequency range, besides the requirement of a phase-true measurement, eliminates the use of isolation transformers as well as Hall-effect current sensors. Thus, classical measurement approaches for impedance measurements at mains voltages cannot be used. Therefore, a direct measurement of current and voltage over shunt resistor at the primary side of a coupling circuit has been chosen in the presented measurement system.

4.2.2 Measurement system implementation

The configuration options of the PLC AIMS is based on voltage-current (V-I) measurements to measure the time- and frequency-variant impedance on the power grid as shown in Fig. 4.1. The V-I measurement technique uses a 2Ω shunt resistor to determine the current. Other principles to characterize the access impedance using VNA have been reported in [89], [90]. The AIMS applies the current error circuit approach, since the expected measured impedance has to be relatively small.

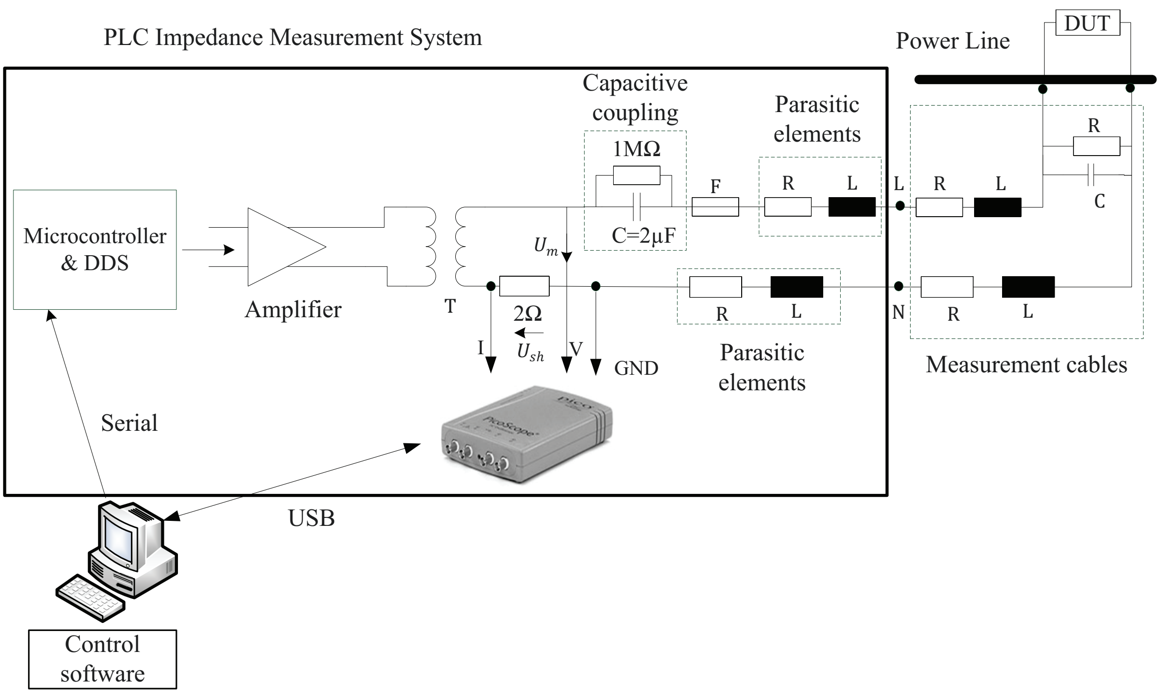

FIGURE 4.1: Access Impedance Measurement System (AIMS) [88]

The PLC AIMS injects a signal into the power line and measures the resulting current and voltage. The 1-500 kHz signal is configured by a microcontroller and generated by a direct digital synthesizer (DDS), then amplified by an analog AB-type amplifier and injected into the power line using a transformer. To avoid short-circuiting the power line through the transformer, a polymer film capacitor of 2μF and 2Ω shunt resistor in series with the transformer is used to form a first order high pass filter. To measure current and voltage of the power line, two channels of a USB oscilloscope (Picoscope 4424) [91] are used to sample the voltage u_m of the power line and the current of the injected signal. Voltage is measured directly, only using the high pass filter to reduce the 50 Hz mains signal to tolerable levels. Current is measured indirectly as a voltage drop u_{sh} over the 2Ω shunt resistor. The measurement software running on a PC controls both the signal injection path and the oscilloscope, and calculates the access impedance from the voltage and current measurements. In the mathematical model, additional coupling elements are added to the system to account as parasitic elements of the coupling circuit model.

The AIMS is connected to the power line with a twisted pair of cables to achieve a maximum of flexibility for different kinds of access points. The DUT in the presented model represents the connected load equipment to the power line near to the measurement point. The impedance of the DUT on the power grid will be measured and analyzed in Chapter 5.

4.3 Signal Processing for Error Correction

The principle of the AIMS is to measure the voltage and current signals $u_x(t)$ from the oscilloscope for each injected signal in the frequency range f_r from 30 to 500 kHz in predefined steps. The index $x = \{m, sh\}$ represents the voltage signal $u_m(t)$ and the current signal as a voltage drop $u_{sh}(t)$. The Fourier series of the measured voltage and current signals $U_x(f_r)$ for each frequency step are then calculated to determine the access impedance of the power line Z_A. The magnitude and phase of the complex signal $U_x(f_r)$ are calculated as $|U_x(f_r)| = \sqrt{Re(U_x(f_r))^2 + Im(U_x(f_r))^2}$ and $\measuredangle U_x(f_r) = \tan^{-1}\left(Im(U_x(f_r))/Re(U_x(f_r))\right)$, respectively. The operations $Re(\cdot)$ and $Im(\cdot)$ represent the real and imaginary parts of the complex signal.

The oscilloscope number of samples is set to 1 million and the sampling frequency to 10 MHz, which enables the implementation of an antialiasing filter and neglects the influence on the frequency band measurement. Hence, each measurement is done for the period of T_p =100 ms over five mains cycles.

The Fourier series of the two measured signals by the oscilloscope for each frequency step is not directly calculated. However, we first take into account the errors that can corrupt the measured signals. After the correction of the measurement errors, the Fourier series is calculated on the corrected signals. The measurement errors and the correction methods are presented in the following.

4.3.1 Mains frequency component rejection and synchronization to the zero-crossings

The high pass filter of the coupling unit is implemented with analog components. It cannot completely reject the mains frequency (50 Hz). The voltage at the output of the high pass filter for the mains frequency is measured and is equal to 440mV_{peak}. Therefore, a digital cancellation will be performed to reject any residual mains components.

For online measurements, the mains frequency component has to be canceled from the two delivered signals of the USB oscilloscope. To do so, the Fourier series of the sampled voltage and current signals $U_{x,s}(f_N)$ for the network frequency f_N= 50 Hz is found as

$$U_{x,s}(f_N) = \frac{1}{T_p} \int_0^{T_p} u_x(t) \cdot e^{(-j2\pi f_N \cdot t)} \cdot dt. \tag{4.1}$$

To synchronize the measurement to the zero-crossings, the time offset t_0 is computed for each frequency step by considering the voltage signal for the 50 Hz frequency $U_{m,s}(f_N)$ as a reference. The time offset t_0 is calculated as

$$t_0 = \frac{1}{2\pi f_N} \cdot \measuredangle U_{m,s}(f_N), \tag{4.2}$$

where $\measuredangle$ represents the angle formed by $U_{m,s}(f_N)$.

From the calculated time offset t_0 in (4.2) and the signal $U_{x,s}(f_N)$ in (4.1), we can determine the synchronized voltage and current signals to the zero-crossings without the mains frequency component $u_{x,ts}(t)$ as

$$u_{x,ts}(t) = u_x(t - t_0) - 2 \cdot |U_{x,s}(f_N)| \cdot \cos(2\pi f_N (t - t_0) + \measuredangle U_{x,s}(f_N)). \tag{4.3}$$

The applied mains frequency rejection method could be influenced by high variations of the mains frequency. However, within the typical mains frequency variations of less than 200 mHz in Europe, this effect can be ignored with respect to other disturbers on the power line.

4.3.2 Frequency offset correction

In the hardware implementation, the transmitter (based on a DDS) and the receiver (based on an oscilloscope) of the AIMS are separate devices. Each device has its own frequency base in the form of an oscillator. The tolerances of both oscillators result in a relative error between the output signal frequency and the input sampling frequency.

For the Fourier series analysis, the output signal frequency of the transmitter f_{tx} is considered to be correct ($f_{tx} = f_r$), and the frequency offset Δf is applied to the reference frequency of the receiver $f_{rx} = f_r + \Delta f$. This frequency offset causes a relative error of $\Delta f_{ppm} = (\Delta f / f_r) \cdot 10^6$ [ppm], which can be expected to be in a range of ±100 ppm, based on the usual specifications of crystal oscillators.

Furthermore, the frequency offset will lead to leakage effects in the Fourier series, spreading the signal's energy over a wider bandwidth and reducing the values at the measurement frequency. To present this influence, an example of the resulting error of the Fourier series calculation for the test signal $u_{test}(t) = e^{(j2\pi(f_w+\Delta f)\cdot t)}$ over the expected range of frequency error Δf_{ppm} is shown in Fig. 4.2. The simulation is done at f_w=500 kHz (worst case frequency) and for different integration periods. The relative error is calculated as $(1 - U_{test}(f)) \times 100\%$.

Table 4.1 shows the allowable frequency error to stay below 1% measurement error with respect to Fig. 4.2. The frequency error Δf_{ppm} is small even for short integration periods

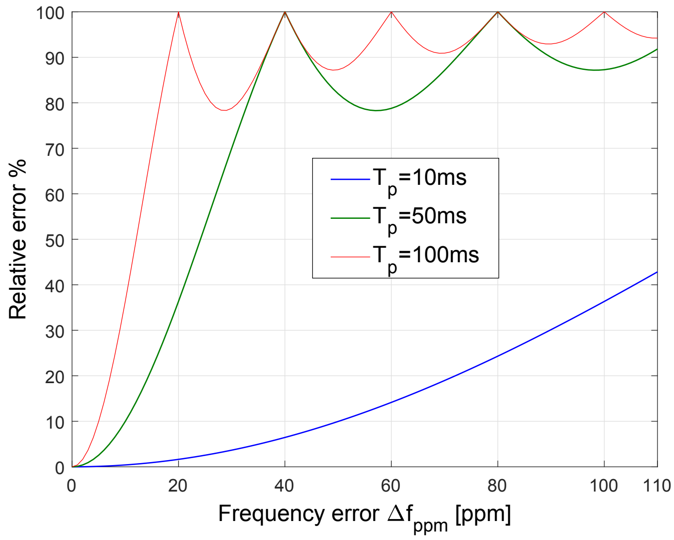

FIGURE 4.2: Relative error of the Fourier series calculation [88]

and decreases with respect to the increment of the integration period. Since the AIMS aims to use a long integration period for a better signal to noise ratio, the allowable frequency error can only be technically achieved if both devices are able to be synchronized to the same frequency base, which is not possible with the available equipment. Therefore, the frequency offset Δf has to be determined and considered in the Fourier series calculation as a correction factor for accurate results.

TABLE 4.1: Maximum frequency error for 1% measurement error

Integration period T_p [ms]	**Max. Frequency error Δf_{ppm}**
10	15.5
50	3.1
100	1.55

The frequency offset correction procedure to synchronize the reference frequency of the signal generator and the USB oscilloscope can be described as follows.

We apply an infinite impulse response (IIR) low-pass filter (LP) with 10/100 kHz pass/stop band frequency on the complex-valued mixed signal to find the equivalent complex base-band (ECB) signals $u_{x,ECB}$ as

$$u_{x,ECB}(t) = LP\Big\{u_{x,ts}(t) \cdot e^{(-j2\pi f_{rx} \cdot t)}\Big\}. \tag{4.4}$$

The frequency offset Δf of the signal $u_{x,ECB}(t)$ is then calculated by finding the mean value of the time derivative of the phase for each frequency step as

$$\Delta f = -\frac{1}{2\pi} \cdot mean\left\{\frac{d\measuredangle u_{x,ECB}(t)}{dt}\right\}. \tag{4.5}$$

The frequency offset Δf of the AIMS in [ppm] and [Hz] is shown in Fig. 4.3 and Fig. 4.4, respectively.

The Fourier series $U_x(f_r)$ and the equivalent short time Fourier series analysis $U_x(f_r, t)$ of the voltage and current signals including the 50 Hz cancellation are finally calculated for each frequency step with the offset Δf and the integral time T_e =0.3ms to determine the frequency- and time-dependent access impedance as

$$U_x(f_r) = \frac{1}{T_p} \int_0^{T_p} u_{x,ts}(t) \cdot e^{(-j2\pi(f_{rx}-\Delta f)\cdot t)} \cdot dt, \tag{4.6}$$

$$U_x(f_r, t) = \frac{1}{T_e} \int_t^{t+T_e} u_{x,ts}(\tau) \cdot e^{(-j2\pi(f_{rx}-\Delta f)\cdot \tau)} \cdot d\tau. \tag{4.7}$$

The presented calculation in (4.6) and (4.7) can be considered as a bandpass filter on the measurement frequencies f_r that cancels all disturbances on the power line. The cyclostationarity behavior of the impedance is analyzed for online measurements based on the short Fourier series computation in (4.7).

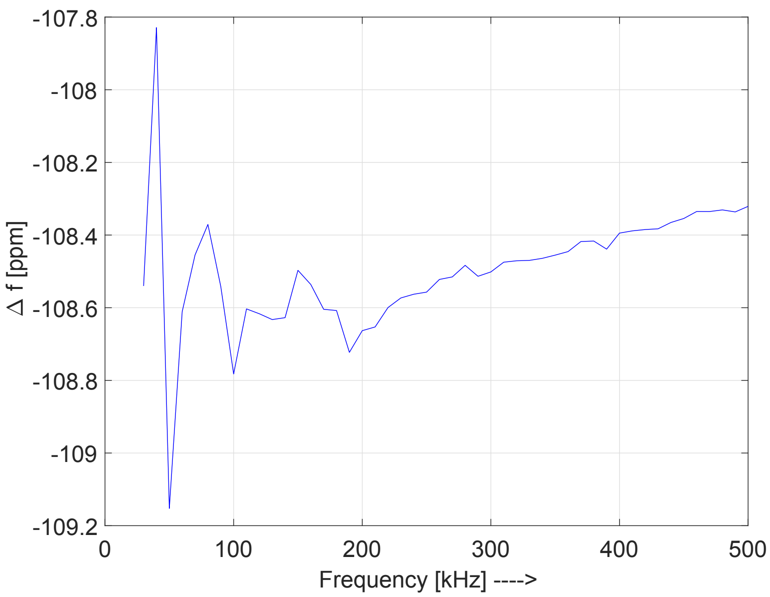

FIGURE 4.3: Frequency offset Δf of the AIMS in ppm [88]

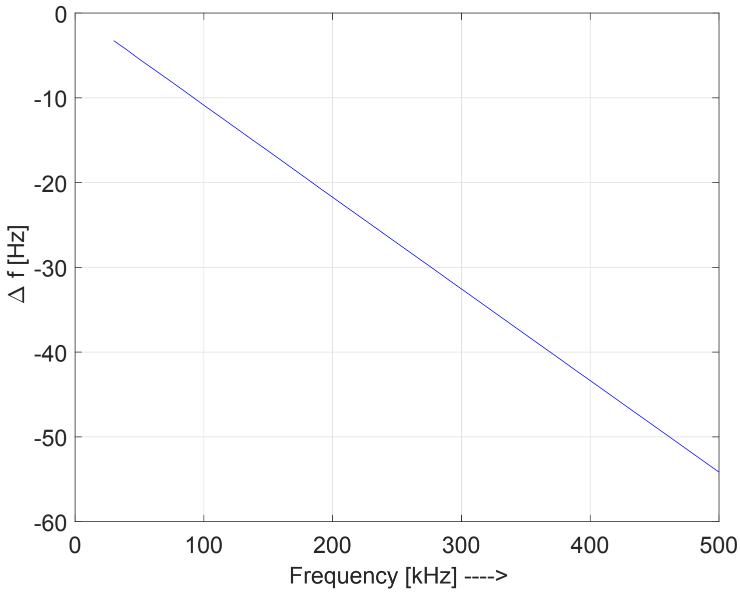

FIGURE 4.4: Frequency offset Δf of the AIMS in Hz [88]

4.4 Fourier Series Integral Time Optimization using Window Function

The short time Fourier series analysis of the voltage and current signals $U_x(f_r, t)$, given in (4.7), are computed over the time period T_e=0.3ms. This calculation is conventionally preformed by applying a rectangular window $w_r(t)$ on the signal $u_{x,ts}(\tau) \cdot e^{(-j2\pi(f_r+\Delta f)\cdot\tau)}$ which can be realized by a convolution in the time domain. The rectangular window is given as

$$w_r(t) = \begin{cases} 1: & 0 \le |t| \le \frac{T_e}{2} \\ 0: & otherwise. \end{cases} \tag{4.8}$$

To increase the efficiency of the short time Fourier series calculation, a window better than the rectangular window can be deployed. A common choice is to use a raised cosine window with a roll-off factor $\gamma = 0 \le \gamma \le 1$ [92]. It can be defined based on [93] as

$$w_c(t) = \begin{cases} 1 & : 0 \le |t| \le \frac{T_e}{2}(1-\gamma) \\ \frac{1}{2}(1+\cos(\frac{\pi}{2\gamma T_e}[|t| - \frac{T_e}{2}(1-\gamma)]) & : T_e(1-\gamma) \le t \le T_e(1+\gamma) \\ 0 & : |t| \le \frac{T_e}{2}(1+\gamma). \end{cases} \tag{4.9}$$

Fig. 4.5 shows the conventional rectangular window in the case of $\gamma = 0$ and the roll-off shape with respect to the calculation time T_e as described in (4.8) and (4.9).

The optimization of the roll-off shape is performed by minimizing the average noise power.

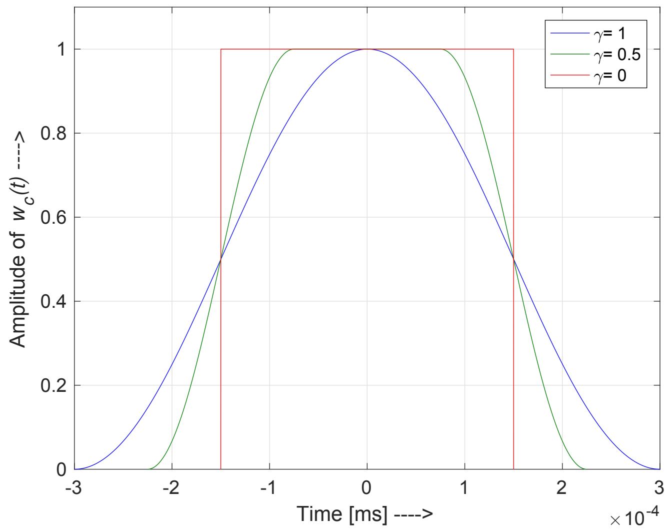

FIGURE 4.5: Raised cosine window $w_c(t)$ with various roll-off factors

To show that, we present a cosine signal $u_c(t)$ as an example with 1V amplitude at the frequency of f_w=500 kHz and sampling time T_s=100ns. The short time Fourier series is calculated as in (4.7) for the signal $U_c(t, f_w)$ using the cosine roll-off window as

$$U_c(f_w, t) = \frac{1}{T_e} \int_t^{t+T_e} w_c(t) \cdot u_c(\tau) \cdot e^{(-j2\pi(f_w - \Delta f)\cdot \tau)} \cdot d\tau. \tag{4.10}$$

Fig. 4.6 presents the frequency response of the signal U_c for the cases of γ={0, 1}. The simulation result shows the efficiency of the cosine roll-off window with γ=1 compared to the rectangular window. This optimization result leads to a better suppression of out-of-band disturbance.

The possible optimization amount can be determined using the mean square error (MSE) between the signal U_c and the noisy signal U_{nc}, assuming additive white Gaussian noise, for the different γ values. The signal $U_{nc}(f_w, t)$ is computed equivalently to (4.10). The MSE is given as

$$MSE = \frac{1}{N_s} \sum_{i=1}^{N_s} (U_{nc,i} - U_{c,i})^2, \tag{4.11}$$

where N_s is the number of samples of U_c and equal to 1 million. Fig. 4.7 shows the MSE in dBV against SNR for the different γ values. The simulation results show the gain of 2dBV in the case of roll-off factor γ =1 compared to the conventional rectangular window.

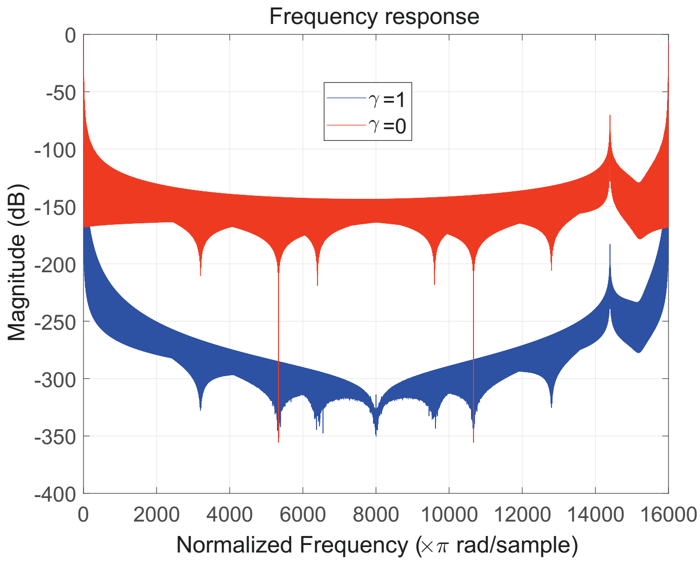

FIGURE 4.6: Frequency response of cosine signal $u_c(t)$ in frequency domain

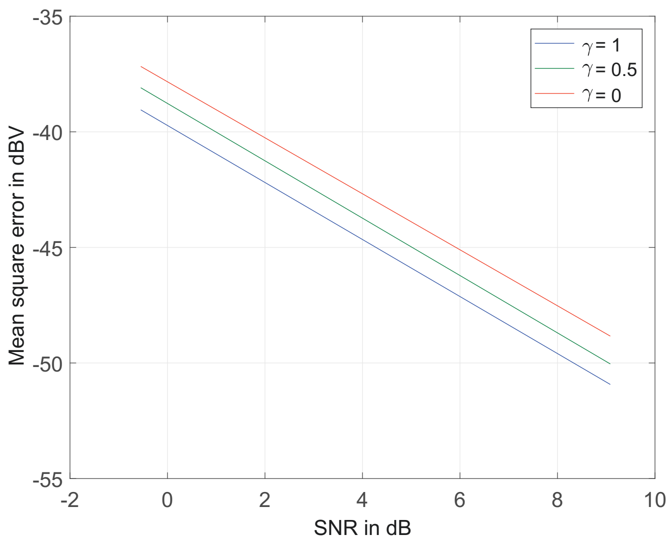

FIGURE 4.7: Mean square error (MSE) between the signal U_c and the noisy signal U_{nc} in [dBV] vs SNR in [dB]

4.5 AIMS Schematic Model

The impedance measurement system setup can be represented by the schematic model in Fig. 4.8. The microcontroller, the DDS, the amplifier and the coupling transformer are equivalently replaced by a voltage source with an internal impedance Z_i. The generated signal U_{DDS} by the DDS is a sine wave with an amplitude of 1V for each frequency step. The access impedance Z_A at the power outlet can be determined from the two frequency- and time-dependent voltages U_m and U_{sh}, and the current over the impedance Z_{sh}. The individual impedance of the connected load to the power line is represented as Z_{DUT} and will be investigated in Chapter 5. The coupling circuit model with the measurement cables is simplified by the serial parasitic impedance Z_{ps}. The influence of the measurement cables are represented by the parallel parasitic impedance Z_{pp}. The effects of the two frequency-dependent impedances Z_{ps} and Z_{pp} is extracted by the calibration measurements.

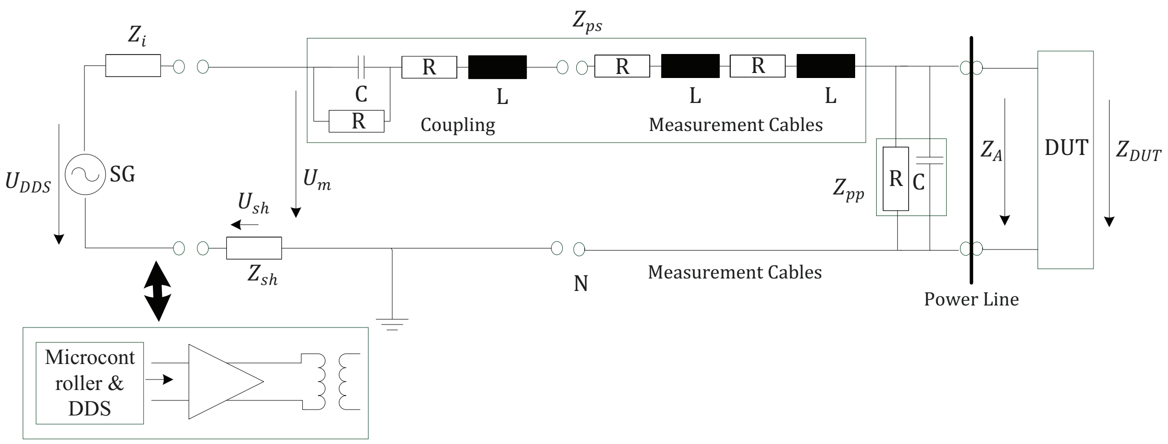

FIGURE 4.8: AIMS schematic model [88]

4.5.1 Measurement specification

The transmission line equations [85] are usually used in high frequency systems. These equations form the basis for a parametric model of the transfer function that is valid for PLC transmission signals in the MHz range [94]. They describe the wave propagation on electrical lines in the case of "electrically long" lines. Thus, the distribution of the voltage along the line is a local and time-dependent function.

However, if the line length is very small compared to the wavelength of the injected signal, then the line is called "electrically short". The injected signal leads to a voltage distribution along the line, which is approximately location-independent and therefore equals to the signal at the injecting point along the line. In this case, no standing waves are formed on the line and the circuit theory can be used for modeling the system.

Since the wavelength at the frequency range of 30-500 kHz is not an influencing factor for the cable length of 2–3 m, the circuit theory is used to determine the access impedance. However, for measurements in MHz frequencies, the wavelength at the cables plays an important role and the technique of the transmission line equations has to be used for the impedance characterization.

To eliminate the different parasitic effects caused by the coupling and the measurement cables, the AIMS has to be calibrated for every new measurement. A simplified schematic of the calibration and the measurement setup is shown in Fig. 4.9. The serial parasitic impedances Z_{ps} of the coupling circuit model with the connected measurement cables to the AIMS are compensated by the series RLC_{ps} circuit which takes into account the influence of the high pass filter. The parallel parasitic impedance Z_{pp} between the measurement cables are compensated by the capacitor C_{pp}.

The two delivered voltages U_m and U_{sh} for each frequency step f_r after the error correction describe the measurement system by the transfer function $H = U_{sh}/U_m$.

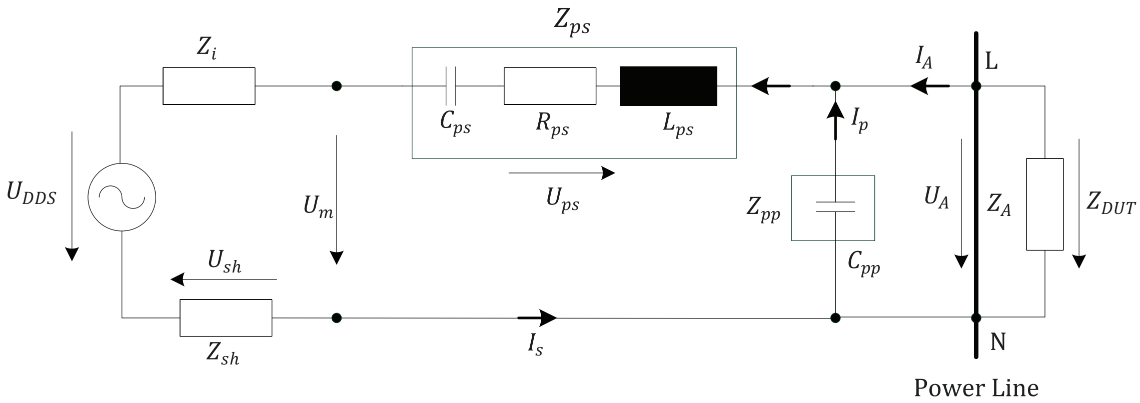

FIGURE 4.9: Simplified schematic of AIMS [88]

To specify the best calibration setup, four measurements are compared as follows.

- $H_0 = \frac{U_{sh_0}}{U_{m_0}}$: The AIMS output shorted.
- $H_\infty = \frac{U_{sh_\infty}}{U_{m_\infty}}$: The AIMS output opened.
- $H_1 = \frac{U_{sh_1}}{U_{m_1}}$: The AIMS output with a reference resistor $Z_{ref} = 1$.
- $H_{10} = \frac{U_{sh_{10}}}{U_{m_{10}}}$: The AIMS output with a reference resistor $Z_{ref} = 10$.

The measurements with the short circuit, $Z_{ref}= 1\Omega$, and $Z_{ref}= 10\Omega$ are chosen to cover the very low access impedance values in frequencies up to 500 kHz. The measurement with the output device opened is considered to cover the high impedances and the effects of the measurement cables. We calculate the standard deviation σ for each measurement H over $N_r = 50$ repetitions. The 50 repetitions are chosen as a trade-off between measurement duration and measurement accuracy given later by the confidence interval. The measurement with 50 repetitions of a single scenario takes about 9 h, since the number of samples captured by the oscilloscope for each frequency step is set to 1 million, and the measurements are performed with a high frequency resolution. Then, the 99% confidence interval of the standard deviation is found to determine the suitable calibration setup. The confidence interval c_i is calculated as $c_i = \bar{M} \pm t(S_M)$, where $\bar{M}$ is the mean of the measurement samples, t is the t-distribution by 99% confidence level equal to 2.6, and S_M is the standard error equal to $\sigma/\sqrt{(N_r)}$. The measurement results shown in Fig. 4.10 present the quality of the calibration where the first measurement scenario, with the output device shorted, brings more errors compared to the other measurement scenarios, which give us an expectation for the best calibration setup combination.

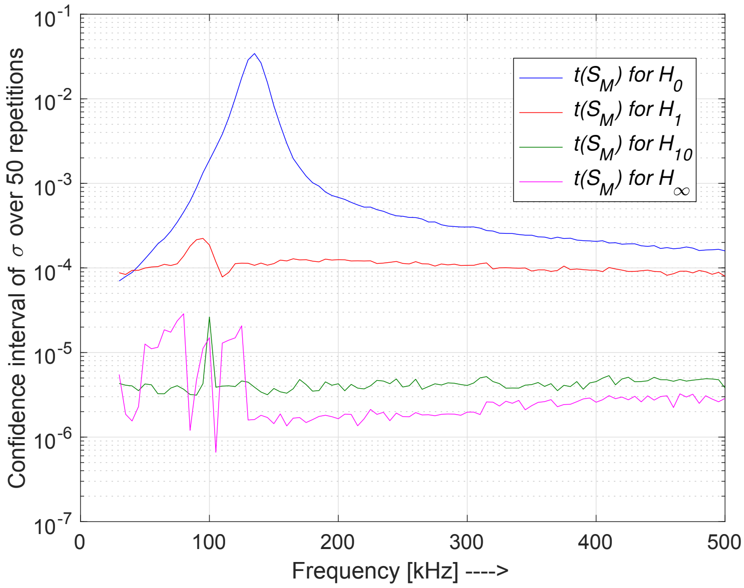

FIGURE 4.10: Confidence interval c_i of the standard deviation σ of four different measurements H over 50 repetitions [88]

4.5.2 Access impedance determination

The time- and frequency-dependent access impedance Z_A of the power grid can be determined from Fig. 4.9 as follows.

The measured voltage U_{sh} by the AIMS is given as

$$U_{sh} = Z_{sh} \cdot I_s. \tag{4.12}$$

The serial current I_s on the AIMS is described by

$$I_s = I_A + I_p = U_A \cdot \frac{Z_A + Z_{pp}}{Z_A \cdot Z_{pp}}. \tag{4.13}$$

The measured voltage U_m by the AIMS is given as

$$U_m = U_{ps} + U_A = Z_{ps} \cdot I_s + \frac{Z_A \cdot Z_{pp}}{Z_A + Z_{pp}} \cdot I_s. \tag{4.14}$$

From (4.12) and (4.14), the transfer function H can be found as

$$H = \frac{U_{sh}}{U_m} = \frac{Z_{sh} \cdot (Z_A + Z_{pp})}{Z_A \cdot Z_{ps} + Z_{ps} \cdot Z_{pp} + Z_A \cdot Z_{pp}}. \tag{4.15}$$

Thus the access impedance Z_A can be calculated from (4.15) as

$$Z_A = \frac{Z_{sh} \cdot Z_{pp} - H \cdot Z_{ps} \cdot Z_{pp}}{H \cdot (Z_{ps} + Z_{pp}) - Z_{sh}}. \tag{4.16}$$

4.5.3 Calibration setup

Typical calibration setups use the possible extremes of the measurement range (short and open circuit) as well as the expected operating point. In our case, the short circuit as the first extreme leads to very low-voltage values resulting in more errors than other measurements of the system transfer function, as shown in Fig. 4.10. Therefore, the lower available reference resistor of 1Ω is chosen instead of short circuit to overcome this problem. As a third calibration point, the reference resistor of 10Ω is added to the setup which still covers the interesting range of low impedance values. The open circuit as the second extreme covers the high impedances range. To verify the applicability of this calibration setup, a comparison with the classical calibration setups using short circuit measurements is performed. Each calibration setup is based on three measurements to estimate the frequency-dependent impedances Z_{sh}, Z_{ps} and Z_{pp}. These impedances vary from one measurement setup to another depending on the cables setup. However, they are equals for a given measurement setup and can be computed for any measurement setup.

- **H_0 & H_1 & H_∞ :**

  Three measurements are done, one with the AIMS output shorted, one with a reference resistor Z_{ref}=1Ω, and one with the AIMS output opened, respectively. This calibration setup is abbreviated in Fig. 4.11 and 4.12 as (01Inf). The calculation of the impedances Z_{sh}, Z_{ps} and Z_{pp} is next considered.

  The AIMS output shorted can be computed from (4.15) as

$$\lim_{Z_A \to 0} (H_0) = \frac{U_{sh0}}{U_{m0}} = \frac{Z_{sh}}{Z_{ps}}. \tag{4.17}$$

  From (4.17), the impedance of the shunt resistor Z_{sh} can be estimated as

$$Z_{sh} = H_0 \cdot Z_{ps}. \tag{4.18}$$

The AIMS output opened can be computed from (4.15) as

$$\lim_{Z_A \to \infty} (H_\infty) = \frac{U_{sh\infty}}{U_{m\infty}} = \frac{H_0 \cdot Z_{ps}}{Z_{ps} + Z_{pp}}. \tag{4.19}$$

From (4.19), the parallel parasitic impedance between the measurement cables Z_{pp} can be estimated as

$$Z_{pp} = Z_{ps} \cdot (\frac{H_0}{H_\infty} - 1). \tag{4.20}$$

The AIMS with a defined reference resistor Z_{ref}=1Ω can be computed from (4.15) as

$$\lim_{Z_A \to 1} (H_1) = \frac{U_{sh1}}{U_{m1}} = \frac{H_0 \cdot Z_{ps} \cdot (1 + Z_{pp})}{Z_{ps} \cdot (1 + Z_{pp}) + Z_{pp}}. \tag{4.21}$$

From (4.21) and (4.20), the serial parasitic impedance Z_{ps} can be estimated as

$$Z_{ps} = \frac{\frac{H_0}{H_\infty} - \frac{H_0}{H_1}}{(\frac{H_0}{H_\infty} - 1) \cdot (\frac{H_0}{H_1} - 1)}. \tag{4.22}$$

- $\boldsymbol{H}_0$ **&** $\boldsymbol{H}_{10}$ **&** $\boldsymbol{H}_\infty$ **:**

The second calibration setup is based on three measurements, one with the AIMS output shorted, one with a reference resistor Z_{ref}=10Ω, and one with the AIMS output opened, respectively. This calibration setup is abbreviated in Fig. 4.11 and 4.12 as (010Inf). The impedances Z_{sh}, Z_{ps} and Z_{pp} can be estimated from (4.15) as

$$Z_{sh} = H_0 \cdot Z_{ps}. \tag{4.23}$$

$$Z_{pp} = Z_{ps} \cdot (\frac{H_0}{H_\infty} - 1). \tag{4.24}$$

$$Z_{ps} = \frac{(\frac{10 \cdot H_0}{H_\infty}) - (\frac{10 \cdot H_0}{H_{10}})}{(\frac{H_0}{H_\infty} - 1) \cdot (\frac{H_0}{H_{10}} - 1)}. \tag{4.25}$$

- $\boldsymbol{H}_1$ **&** $\boldsymbol{H}_{10}$ **&** $\boldsymbol{H}_\infty$ **:**

The third calibration setup is based on three measurements, one with a reference resistor Z_{ref}=1Ω, one with a reference resistor Z_{ref}=10Ω, and one with the AIMS output opened, respectively. This calibration setup is abbreviated in Fig. 4.11 and 4.12 as (110Inf). The impedances Z_{sh}, Z_{ps} and Z_{pp} can be estimated from (4.15) as

$$Z_{sh} = H_\infty \cdot (Z_{ps} + Z_{pp}). \tag{4.26}$$

$$Z_{ps} = -\frac{Z_{pp} \cdot (-H_{\infty} \cdot Z_{pp} + H_1 - H_{\infty})}{H_1 \cdot Z_{pp} - H_{\infty} \cdot Z_{pp} + H_1 - H_{\infty}}. \tag{4.27}$$

$$Z_{pp} = \frac{9 \cdot H_1 \cdot H_{10} - 10 \cdot H_1 \cdot H_{\infty} + H_{10} \cdot H_{\infty}}{H_{\infty} \cdot (H_1 - H_{10})}. \tag{4.28}$$

Three measurements of each calibration setup are repeated 50 times. The mean value of the 50 measurement repetitions is calculated to select and ensure the best calibration setup that delivers the most accurate results. However, calibration and access impedance measurements are performed for one time for each frequency step without repetitions and mean value calculation. The measurement results show that the 2Ω shunt resistor can be correctly measured using the three calibration setups as presented in Fig. 4.11. The third calibration setup (H_1 & H_{10} & H_{∞}) has been selected for the AIMS, since this calibration setup can accurately measure the 2Ω shunt resistor and the confidence interval of the measurement with the output device shorted brought the most errors.

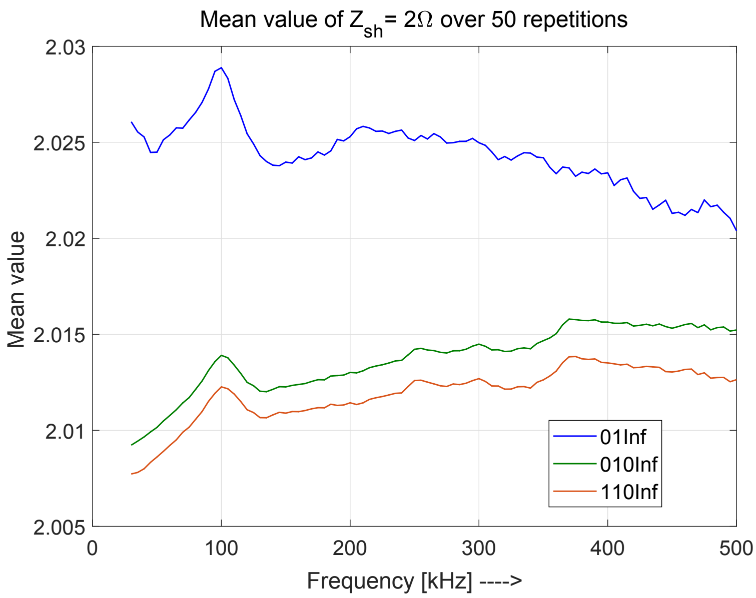

FIGURE 4.11: Mean value of Z_{sh} for different calibration setups over 50 repetitions [88]

Moreover, the measurement results over the 50 repetitions for each calibration setup show that the impedance Z_{pp} (parallel to Z_A) for frequencies up to 500 kHz is high impedance, above 1kΩ and equivalently for all calibration setups, as presented in Fig. 4.12. Thus, the parallel parasitic effects between the measurement cables can be neglected for measurements up to 500 kHz. For measurements in broadband frequencies, the influence of this impedance has to be considered, since it going to be low. As a consequence, the best selected calibration setup can be simplified to consider only two measurements, namely (H_1 & H_{10}). The impedances Z_{sh} and Z_{ps} for the simplified calibration setup (H_1 & H_{10}) can be estimated by

$$Z_{ps} = \frac{10 \cdot H_{10} - H_1}{H_1 - H_{10}}, \quad Z_{sh} = H_1 \cdot Z_{ps} + H_1. \tag{4.29}$$

The access impedance of the power line based on the simplified calibration setup can be determined from (4.16) in detail as

$$Z_A(f_r, t) = \frac{U_m(f_r, t) \cdot Z_{sh}(f) - U_{sh}(f_r, t) \cdot Z_{ps}(f)}{U_{sh}(f_r, t)}. \tag{4.30}$$

The simplified calibration setup can be in the same way used as the original one for measurements up to 500 kHz. The presented AIMS software provides the simple and the original calibration setup.

In Appendix A, we provide further details on the calibration setup with respect to the calibration point, where we connect the calibration resistors to the measurement system. In addition, we show the influence of the measurement cables lay setup on the calibration accuracy (see Appendix A).

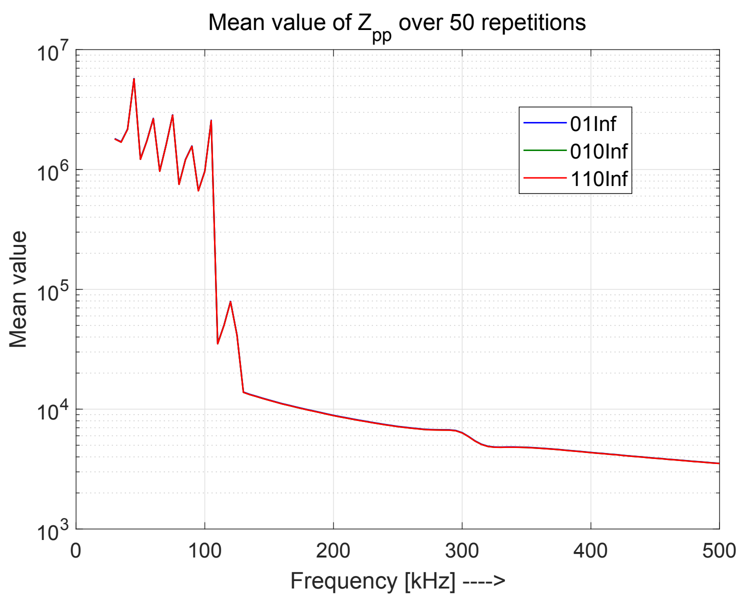

FIGURE 4.12: Mean value of Z_{pp} for different calibration setups over 50 repetitions [88]

4.6 Access Impedance Measurements Results Using AIMS

In this section, different impedance measurement results are presented. First, offline impedance measurements are executed to show the accuracy of the AIMS. Online access impedance measurement on different power outlets are then performed. The measurement software provides three representative results, namely the magnitude, the imaginary part, and the real part of the impedance with respect to the frequency and time. The original calibration setup is applied for all measurement results to cover the high and low impedance values.

4.6.1 Offline measurement results

In order to evaluate the accuracy of the AIMS, offline measurements have been done on reference resistors from 1Ω to 10Ω. These reference resistors has a tolerance value of 1%. The measured resistor values cover the interesting range of low impedances that can affect the communications over PLC in the frequency range up to 500 kHz. The accuracy of the measured resistor values is evaluated by comparing them to nominal values and to the same measurements done by the vector network analyzer (Bode 100) considered as an impedance analyzer [95]. The absolute and relative errors are computed. The absolute error has been calculated as the magnitude difference between measurement with AIMS and nominal values, and as the magnitude difference between measurements with AIMS and Bode 100. The relative error has been calculated considering the absolute error as a percentage of the nominal value of the reference resistors.

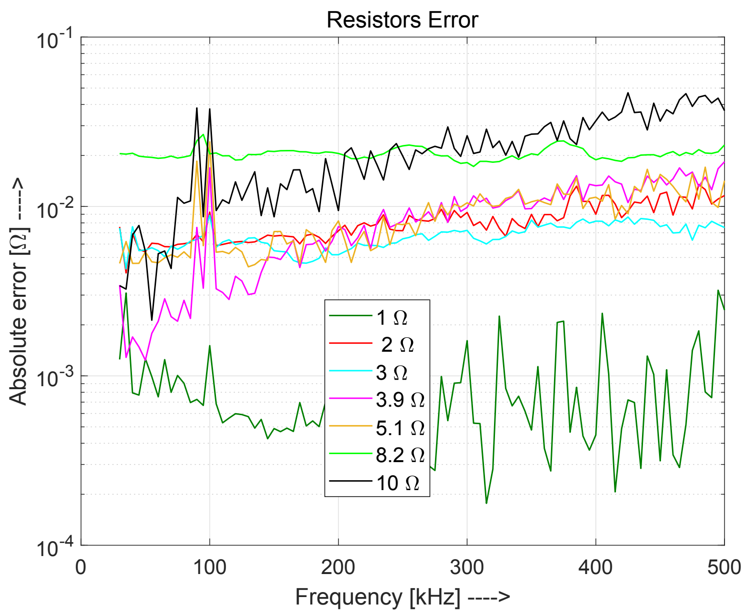

FIGURE 4.13: Magnitude of absolute error in resistor measurements compared to nominal values [88]

Fig. 4.13 and Fig. 4.14 show the absolute and relative error for the measured reference resistors compared to nominal values, respectively. The absolute error is less than 0.05Ω and the relative error is less than 0.7%.

Fig. 4.15 and Fig. 4.16 show the absolute and relative error for the measured reference resistors compared to the impedance analyzer Bode 100, respectively. The absolute error is less than 0.06Ω and the relative error is less than 0.6%. These measurement results represent the accuracy of the AIMS which is less than 1% error for impedances smaller than 10Ω over the frequency range between 30-500 kHz.

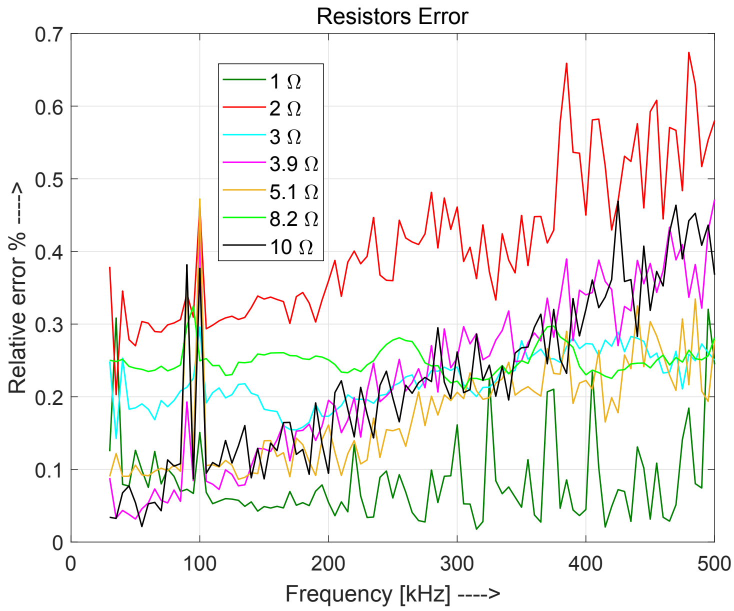

FIGURE 4.14: Magnitude of relative error in resistor measurements compared to nominal values [88]

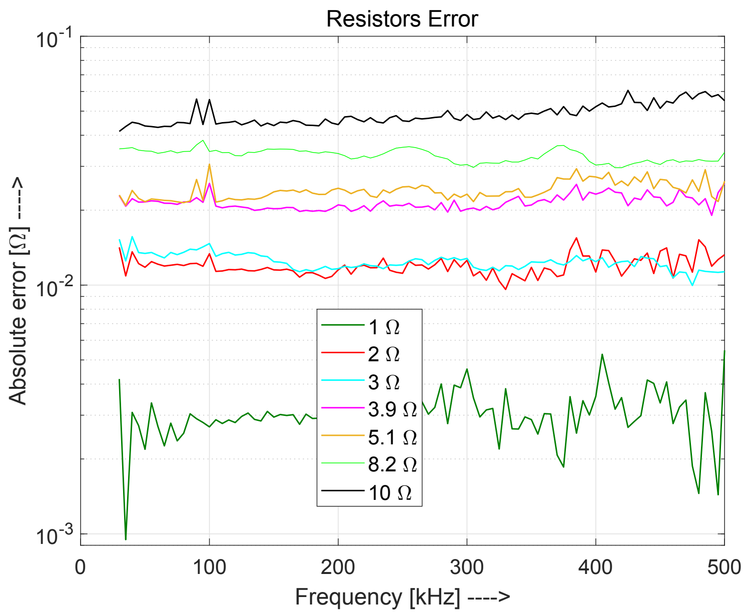

FIGURE 4.15: Magnitude of absolute error in resistor measurements compared to impedance analyzer (Bode 100) [88]

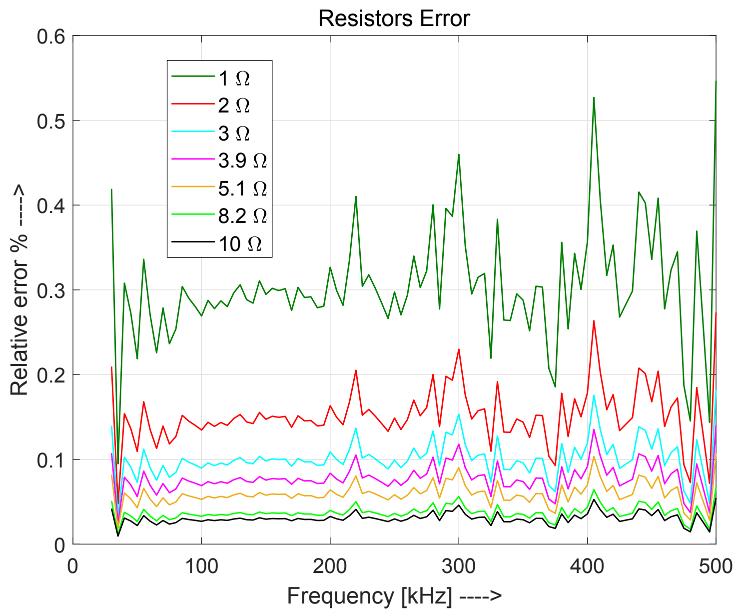

FIGURE 4.16: Magnitude of relative error in resistor measurements compared to impedance analyzer (Bode 100) [88]

4.6.2 Online access impedance measurement results

Access impedance measurements at the power line have been executed on different outlets on the low-voltage distribution grids. The measurements setup where loads and no loads are connected near to the measurement point is shown in Fig. 4.17. The AIMS is always connected very nearly to the measurement point using a power strip. The power strip is used to connect electrical loads as close as possible to the measurement point to show their effects on the power grid.

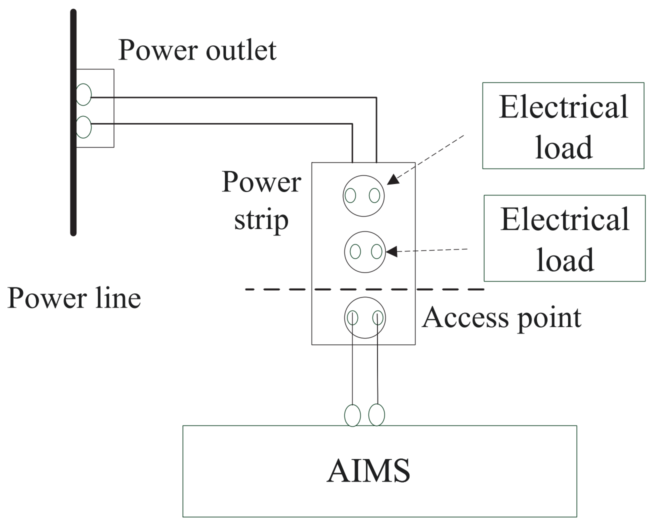

FIGURE 4.17: Access impedance measurements setup [88]

Fig. 4.18 shows access impedance measurements in the university laboratory on different power outlets where no load equipment are connected near to the measurement point. The access impedance of the electro lab table outlet 2 is lower than the other power outlets, because other appliances are usually built in the table close to the connection box. The access impedance is increasing towards the higher frequencies and below 1Ω at the frequency of 100 kHz in case of power outlet 2.

Fig. 4.19 and Fig. 4.20 show the access impedance with respect to time and frequency for measurements in the university laboratory on power outlet 1 and 2 where no load equipment are connected near to the measurement point during one cycle of the mains (20 ms at 50 Hz). The access impedance is stable over the time and there are no variations within one mains cycle.

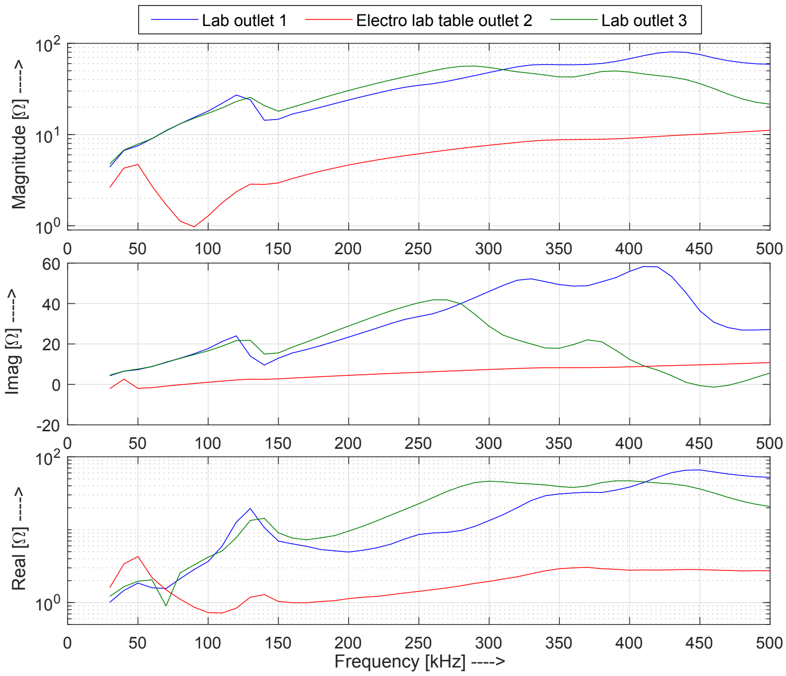

FIGURE 4.18: Access impedance measurements on different power outlets where no loads are connected near to the measurement point [88]

Fig. 4.21 shows access impedance measurements in the university laboratory on lab power outlet 1 and electro lab table outlet 2 where different load equipment are connected near to the measurement point. As connected loads, the following equipment are considered: Samsung monitor P2250, Philips PM3082 oscilloscope, Fujitsu laptop Lifebook E781 with power supply type CP410715-01, and Samsung TV UE65JU6050U. The measurement results show the different behavior of the connected load equipment on the different power outlets. The magnitude of the impedance where the Samsung monitor and the Fujitsu laptop are connected near to the measurement point are below 1Ω in the FCC frequency band, 0.37Ω by 210 kHz and 0.5Ω by 360 kHz, respectively. The Samsung TV causes magnitude of impedance below 1Ω in the CENELEC frequency bands.

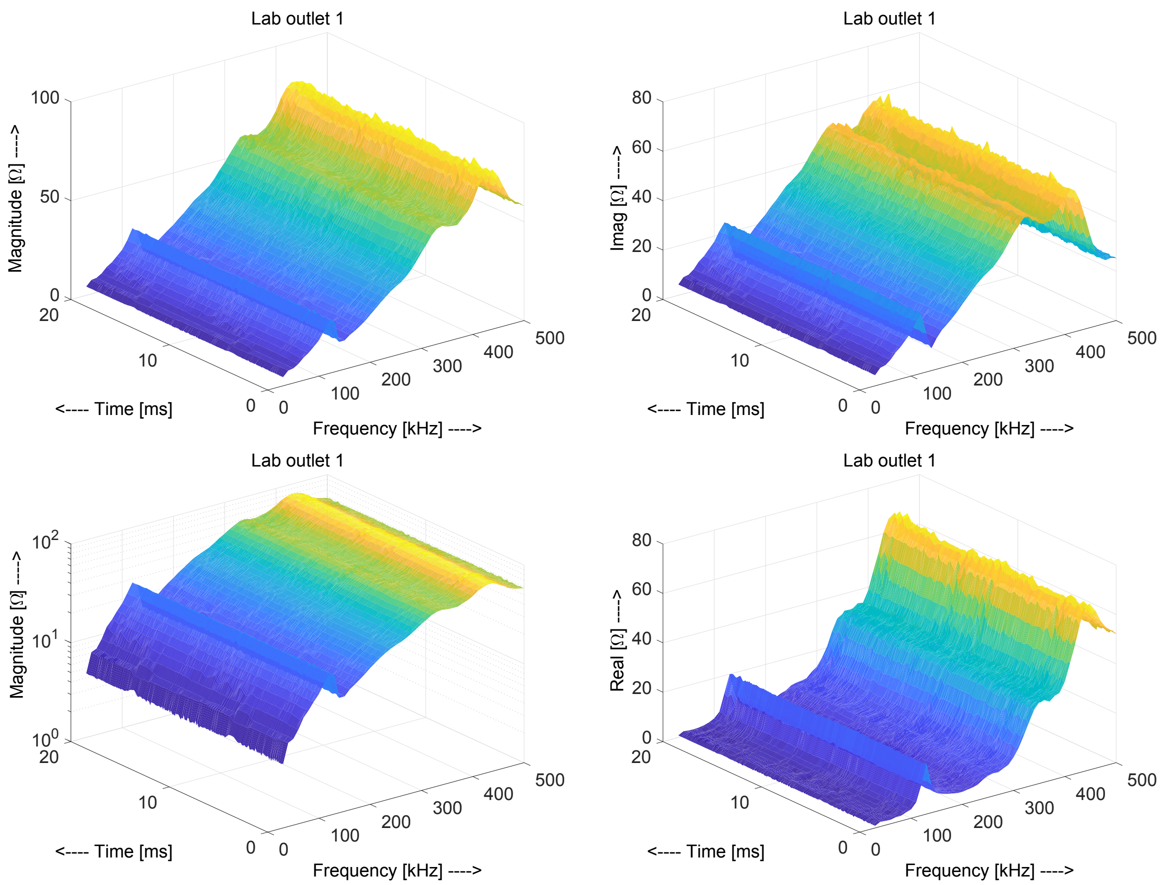

FIGURE 4.19: Access impedance measurement on lab outlet 1 with respect to time and frequency where no loads are connected nearby [88]

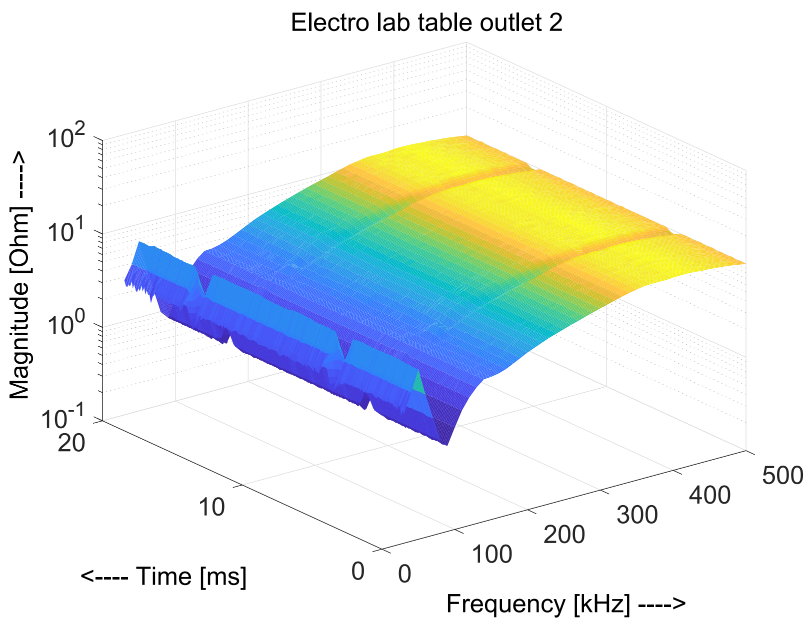

FIGURE 4.20: Access impedance measurement on lab outlet 2 with respect to time and frequency where no loads are connected nearby [88]

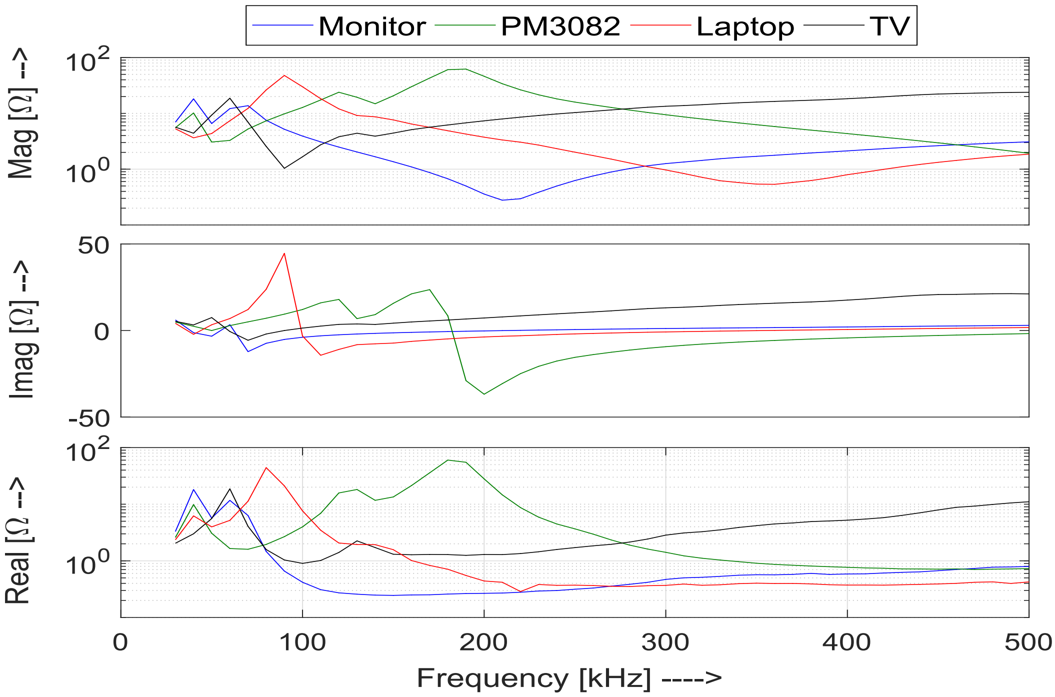

(A) Lab power outlet 1

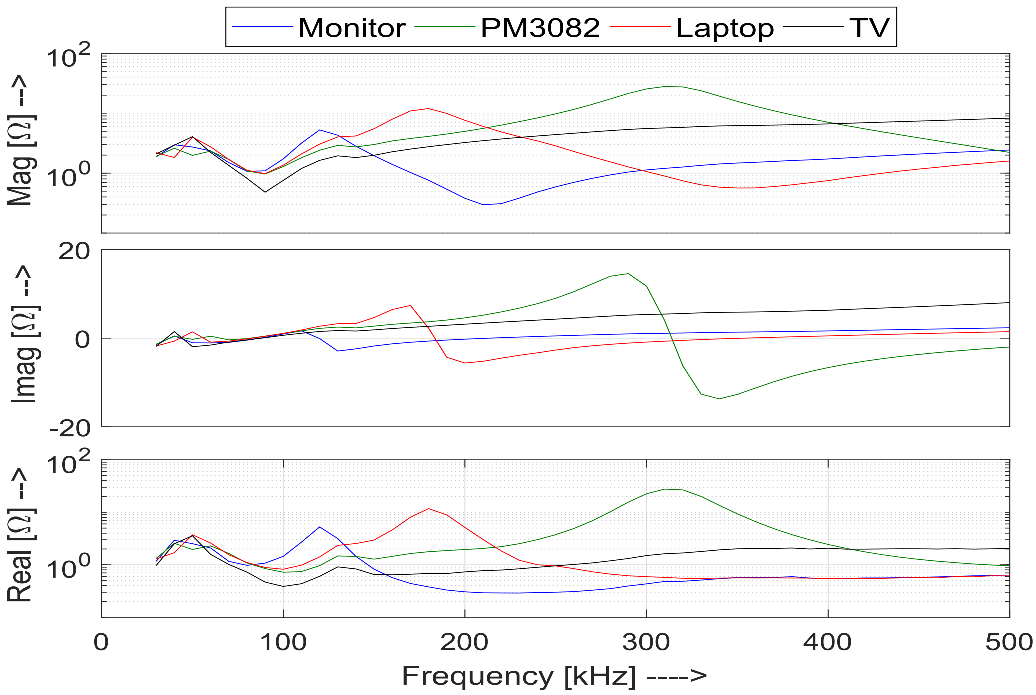

(B) Electro lab table power outlet 2

FIGURE 4.21: Access impedance measurements on different power outlets where load equipment are connected near to the measurement point

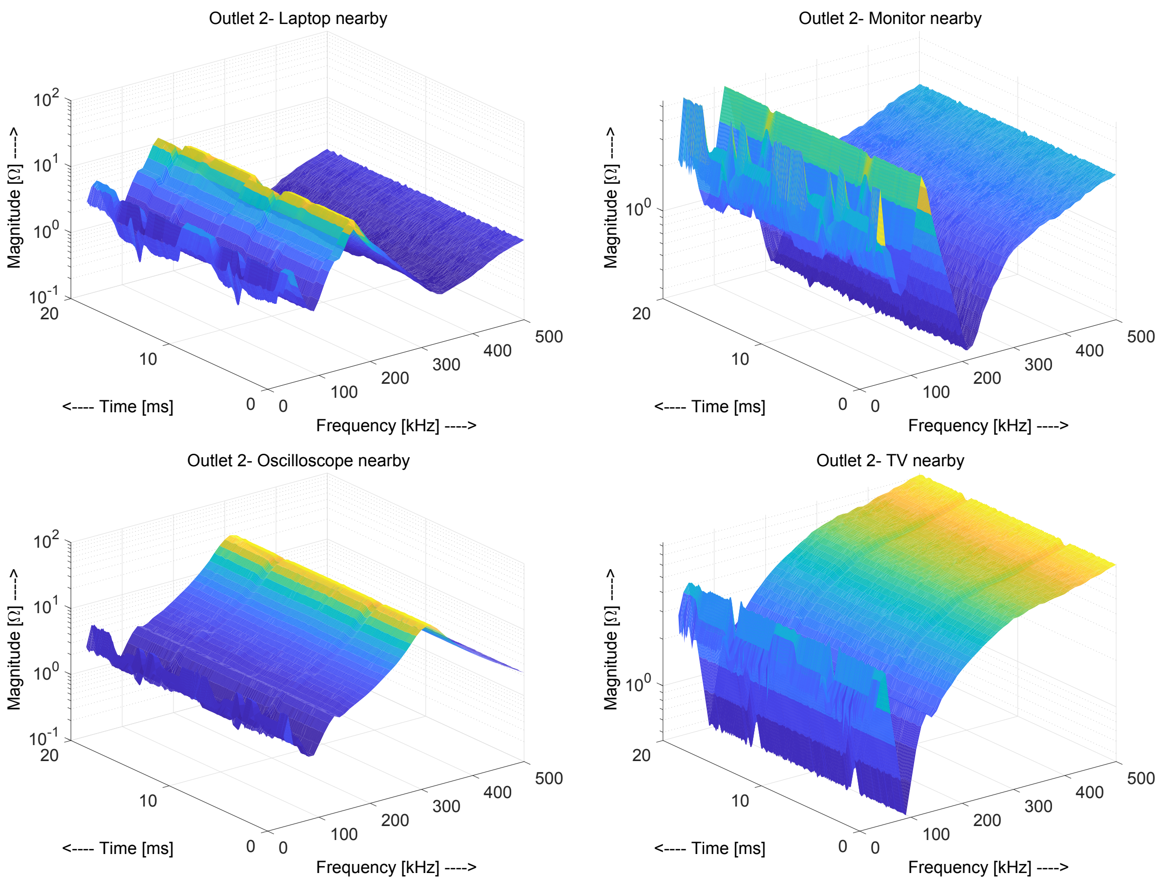

FIGURE 4.22: Access impedance measurement on electro lab table outlet 2 with respect to time and frequency where different loads are connected nearby [88]

Fig. 4.22 shows the cyclostationarity behavior of the access impedance for measurements in our university laboratory on electro lab table outlet 2 where different load equipment are connected near to the measurement plug using a power strip during one cycle of the mains (20 ms at 50 Hz). As connected loads, we consider the same equipment as in Fig. 4.21. The access impedance variation within one mains cycle depends basically on the nearby loads. The cyclostationarity of the access impedance where the Samsung monitor P2250 and the Fujitsu laptop are connected near to the measurement point is much larger than the Philips oscilloscope PM3082 and the Samsung TV, especially in the CENELEC bands.

An overview of all performed access impedance measurements in this chapter is presented in Table 4.2.

Finally, a statistical verification of measurements with the AIMS is introduced. We calculate the standard deviation σ over $N_r = 25$ repetitions to evaluate the measured access impedances where the Samsung monitor is connected near to the measurement point. Then, the 99% confidence interval of the standard deviation is found for the t-distribution equal to 2.7 over 25 repetitions. This measurement represents a critical case of measurement accuracy

TABLE 4.2: Access impedance measurements overview

Measurement type	**Measurement setup**	**Frequency observation**	**Time observation**
Offline impedance	Reference resistors	Error less than 1%	-
Access impedance	No load	Below 1 Ohm in some cases	Mostly time-invariant
Access impedance	With load (Oscilloscope-TV)	Below 1Ω in CENELEC bands	Mostly time-invariant
Access impedance	With load (Monitor-Laptop)	Below 0.5Ω in FCC bands	Time-variant

because of the strong time-variant behavior and very low impedance. The measurement repetitions are performed under defined setup during the night to keep the power line network as much as possible unchangeable. The 25 repetitions have been again chosen as a tradeoff between measurement duration and accuracy. The measurement duration takes about 5 h with a fine frequency resolution. Fig. 4.23 shows the accuracy of the online access impedance measurement results where the measurement error over 25 repetitions on power outlets 1 and 2 is acceptable over the frequency range.

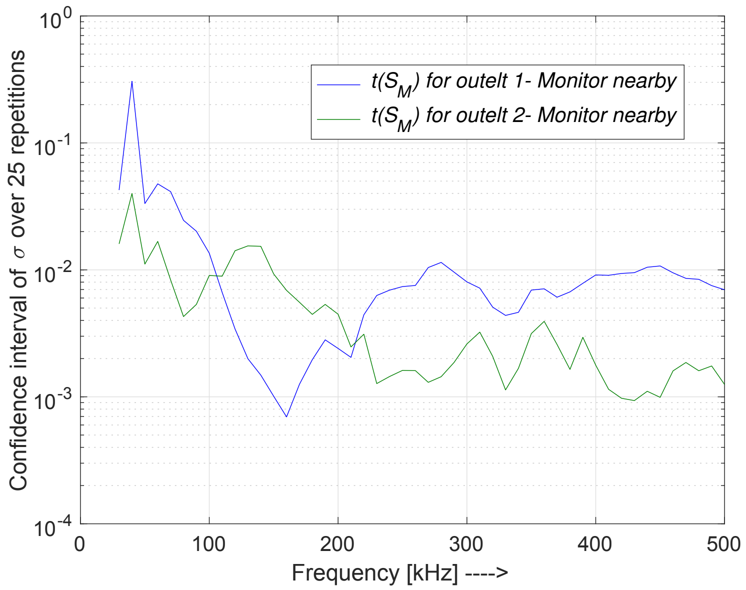

FIGURE 4.23: Confidence interval c_i of the standard deviation σ for access impedance measurements on power outlet 1 & 2 where a monitor connected near to the measurement point [88]

4.7 Conclusion

This chapter has described in detail the operation concepts of the access impedance measurement system for PLC at frequencies between 30-500 kHz. Different calibration setups for the measurement system are compared. Frequency offset correction has been added to the system to synchronize the reference frequency of the DDS and the oscilloscope. The applied signal processing provided the cancellation of the mains frequency and the synchronization to the zero-crossings. This access impedance measurement system was able to measure low impedances with error less than 1%. Access impedance measurements on different power outlets at the university laboratory are performed and are shown the variable characteristic of the network impedance over time and frequency caused by the connected devices. The measured access impedances are in some cases very low, below 0.3Ω, at the resonance points with a strong time-variant behavior.

Chapter 5

Load Impedance Measurement

The measurement and analysis of load impedances on the power grid is the topic of this chapter. The characterization of PLC propagation channel is mainly dependent on the load impedance characteristics. Therefore, we carried out a measurement campaign on a representative set of devices that can be found in a house, office or laboratory. The measurement procedure has enabled the analysis of the impedance behavior with respect to time and frequency within the frequency range between 30-500 kHz that is used by NB-PLC systems. We have found that the impedance behavior of each equipment varies on the power grid, some equipment has a time-variant impedance and others have time-invariant impedance. This is caused by the switched-mode power supply and the EMI filter design which change their behavior significantly on the power network. Furthermore, the measured load impedances will be evaluated and verified with respect to their time and frequency behavior.

5.1 Introduction

The characterization of the PLC propagation channel at frequencies up to 500 kHz is mainly dependent on the load impedances, the attenuation, the noise, and the electrical cable characteristics. Experimental characterization of the low voltage cables for narrowband PLC is presented in [96]. It has been recognized that the PLC channel response is affected by the presence of transformers [97] and electrical device (load) impedances [98]–[100].

The knowledge of the load impedances allows the prediction of the channel transfer function through the application of a bottom-up channel modeling approach that uses transmission line theory applied to a certain network topology, as it is done for instance in [37], [38], [40]. This approach computes the channel transfer function when the wire topology, the wire electrical characteristics, and the load impedances are known. Therefore, the accurate measurements of load impedances connected to the low-voltage transmission lines is a necessary requirement to understand the behavior of the power line channel.

A vector network analyzer (VNA) is used for the characterization of the time-variant impedance of devices encountered in home PLC networks for broadband frequencies 2- 30 MHz [101], [102]. Other principles to measure time-variant load impedances have been reported in [103], [104]. However, the impedance of electrical devices on the power grid at frequencies up to 500 kHz has not yet been measured and considered. This chapter fills this gap by extending the access impedance measurement system (AIMS) presented in Chapter 4 to measure the impedance of electrical load devices in the frequency range of 30-500 kHz [105].

This chapter is organized as follows: In Section 5.2, we present a method to measure the impedance of load equipment that are connected to the power grid using the AIMS. Measurement results of the impedance of different load equipment are presented in Section 5.3. A procedure to verify the measured load and access impedances with respect to time and frequency is proposed in Section 5.4. Finally, the chapter is concluded in Section 5.5.

5.2 Impedance Measurement Procedure of Electrical Devices

In this section, we present a method to measure the connected load impedances to the power grid in frequencies up to 500 kHz using the introduced AIMS in Chapter 4. This measurements allow the analysis of the load impedance behavior in context of time variation and frequency dependency.

The measurement idea is to connect a device that has a high impedance representation on the power grid in parallel to the device under test (load) which allows the estimation of the load impedance, since the expected impedance of loads has to be low in the narrowband frequencies.

The measurement setup of equipment load impedance on the power grid is described in Fig. 5.1. As a high impedance device, an isolation transformer (IT) is considered. The output of the isolation transformer is connected to the AIMS in parallel to the device under test (DUT). The isolation transformer is connected to the power line and supplies the DUT with electricity to measure its impedance in active mode.

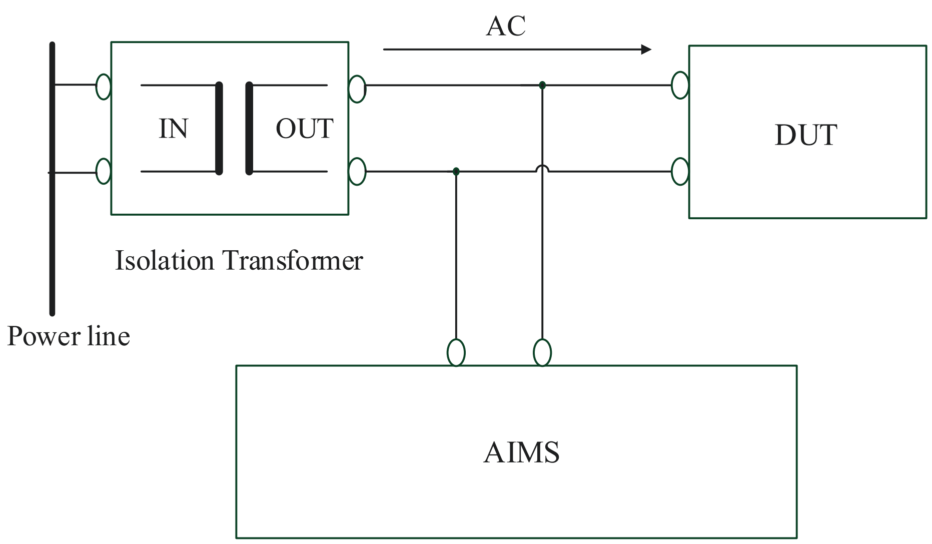

FIGURE 5.1: Load impedance measurement setup using an isolation transformer [88]

5.2.1 Load impedance calculation

A simplified schematic of the load impedance measurement setup is shown in Fig. 5.2. The schematic of the AIMS is simplified as the simplification in Fig. 4.9. The measured impedance Z_{me} by the AIMS is given as

$$Z_{me}(f_r, t) = \frac{1}{Z_{IT}(f_r, t)^{-1} + Z_{DUT}(f_r, t)^{-1}}, \tag{5.1}$$

where f_r represents the measurement frequency range.

From (5.1), the load impedance Z_{DUT} can be found as

$$Z_{DUT}(f_r, t) = \frac{-Z_{me}(f_r, t) \cdot Z_{IT}(f_r, t)}{Z_{me}(f_r, t) - Z_{IT}(f_r, t)}. \tag{5.2}$$

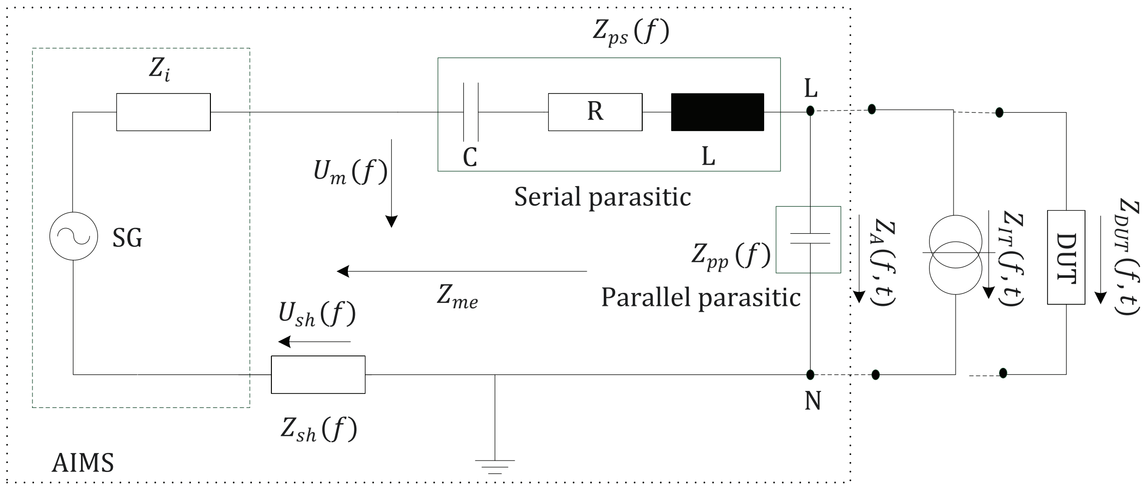

FIGURE 5.2: Schematic setup of load impedance measurement [88]

In order to measure the load impedance as in (5.2), the isolation transformer impedance has to be known. In particular, we firstly measure the access impedance (Z_{IT}) where the IT is connected to the power gird. After that, we connect the load equipment to the output of the isolation transformer and perform the load impedance measurement to determine the impedance Z_{DUT}.

This load impedance measurement method has a different calibration setup than the access impedance measurement, since the load impedance has to be separated from the measurement. In fact, the calibration point (where we connect the reference resistors) of the load impedance measurement is not the same as for the access impedance measurement. More details about the calibration setup of load impedance measurement are given in the Appendix A.

5.2.2 Isolation transformer impedance measurement

The measurement setup of the impedance of the IT (Z_{IT}) is shown in Fig 5.3, where the IT is connected only to the power line. The impedance measurement of the IT is shown in Fig. 5.4. As expected, the VOLTCRAFT IT-1500 [106] has a high impedance representation on the power line by 1.5 kΩ at the resonance point and can be used for the proposed measurement method. Moreover, the measurement result with respect to time and frequency shows that the impedance of the IT is time-invariant and can be considered as only frequency-dependent $Z_{IT}(f)$, as depicted in Fig. 5.5.

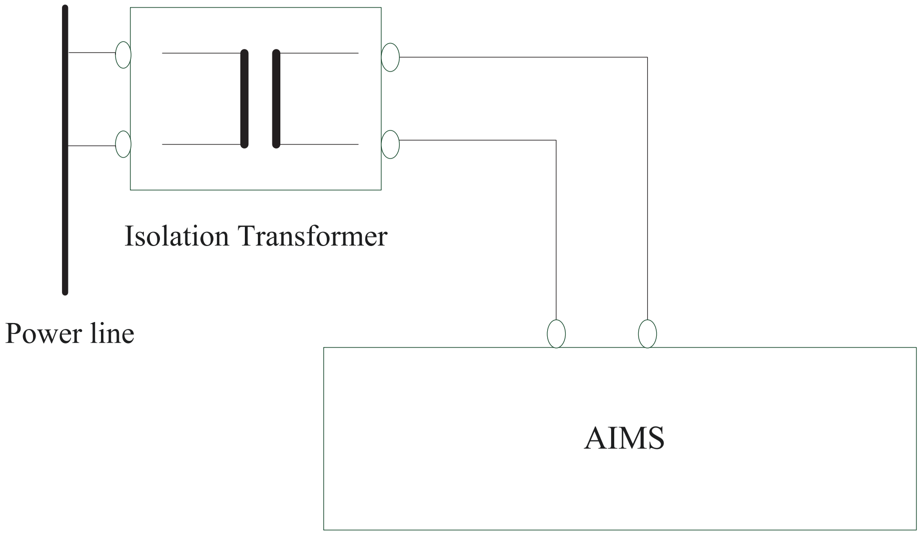

FIGURE 5.3: Impedance measurement setup of IT [88]

Furthermore, we consider a method to increase the impedance of the isolation transformer. We connect two VOLTCRAFT IT-1500 in serial and measure the impedance of them as shown in Fig. 5.6. The measurement result presented in Fig. 5.7 shows that the impedance of the two isolation transformers that are connected in serial on the power line has been decreased unexpectedly and two resonance points at the frequencies of 120 kHz and 360 kHz appear. Thus, connecting more IT in series cannot increase the impedance of the isolation transformer for the equipment impedance measurement.

In Appendix B, we compare the impedance of different available isolation transformer types. The measurement results show that the VOLTCRAFT IT-1500 is the highest impedance between them. Therefore, the VOLTCRAFT IT-1500 is used in all load impedance measurements.

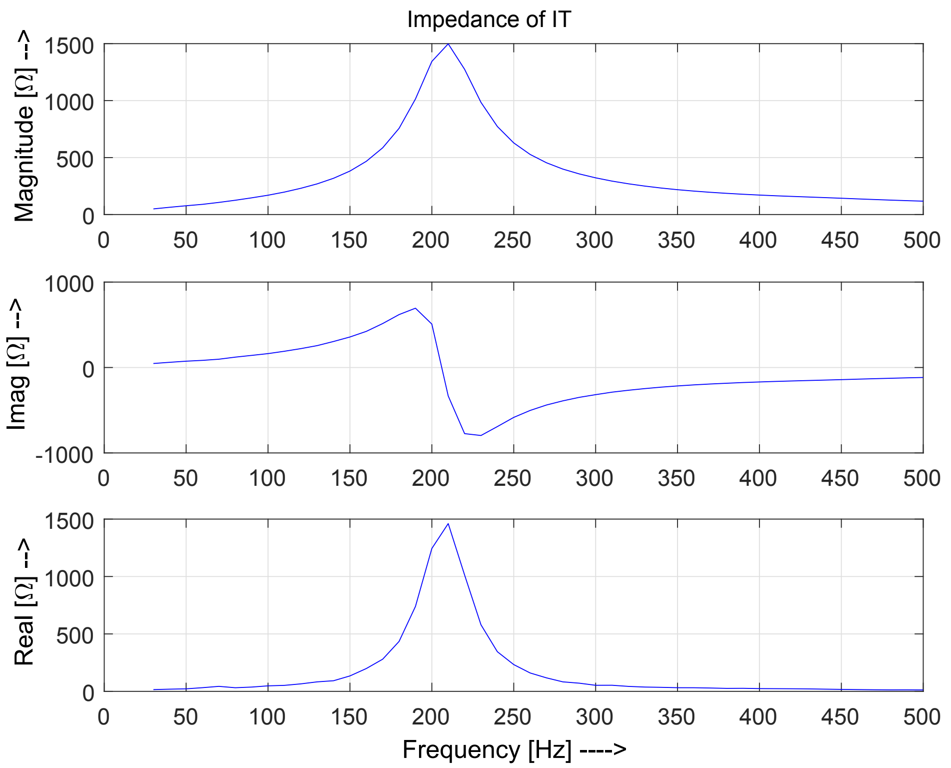

FIGURE 5.4: Impedance measurement of the isolation transformer on the power line with respect to frequency [88]

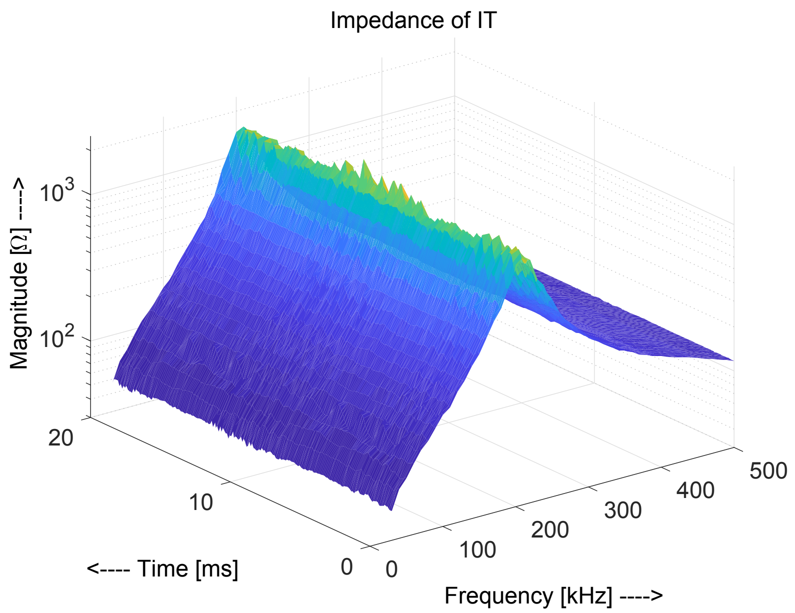

FIGURE 5.5: Impedance measurement of the isolation transformer on the power line with respect to time and frequency [105]

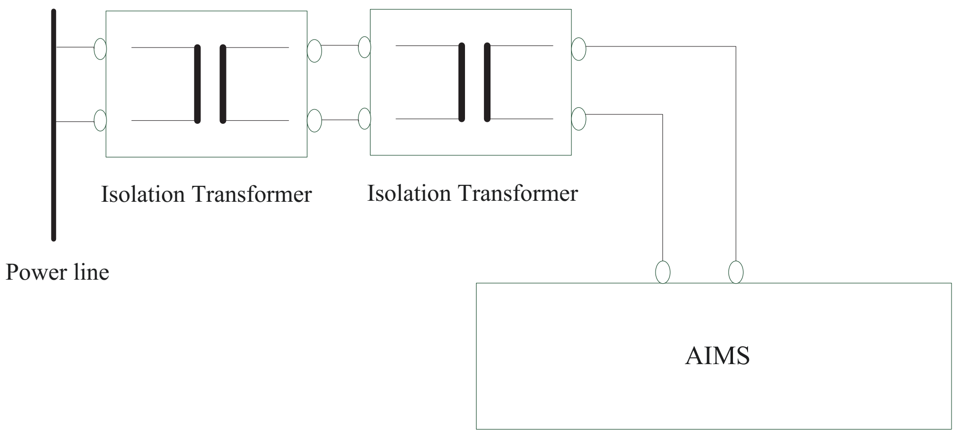

FIGURE 5.6: Impedance measurement setup of two ITs in serial [105]

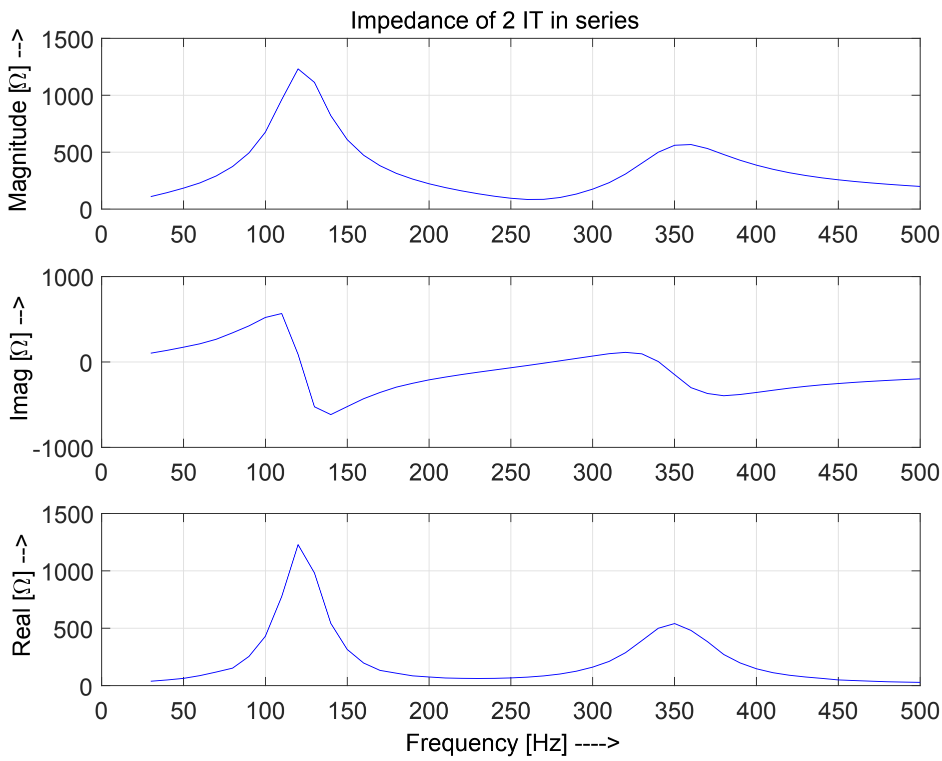

FIGURE 5.7: Impedance measurement of two isolation transformers that are connected in serial to the power line [105]

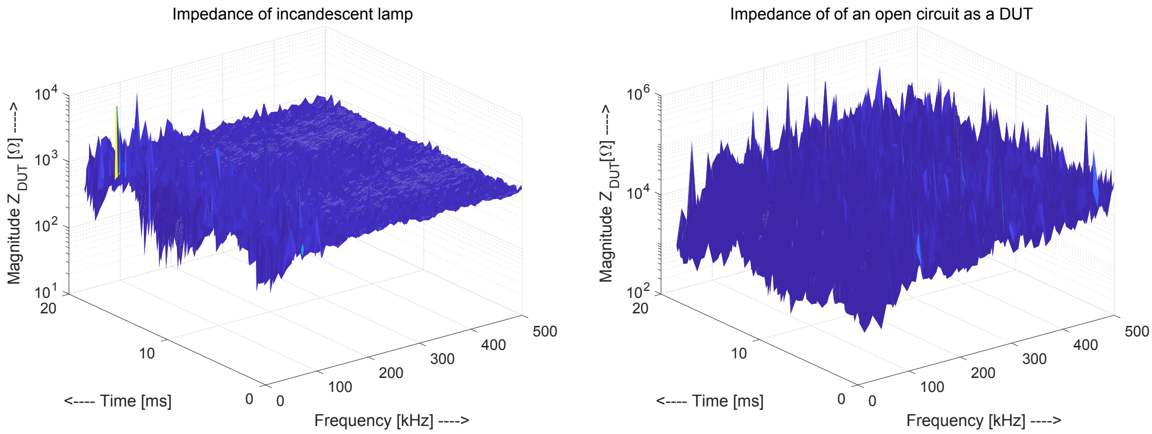

FIGURE 5.8: Time- and frequency-dependent impedances of incandescent lamp and open circuit as DUT [88]

5.3 Online Impedance Measurement of Electrical Load Equipment

The load impedance measurement is done as described in Fig. 5.1 and with respect to (5.2). As connected loads, we focus on the following appliances: open circuit as an DUT, incandescent lamp, Philips oscilloscope PM3082, Samsung TV UE65JU6050U, Fujitsu laptop E-Series, and Samsung monitor P2250. These equipment show an interesting behavior on the power grid with respect to the time and frequency.

The measurement results shown in Fig. 5.8, confirm the equipment impedance measurement method where the measured impedance of an open circuit as an DUT in parallel to the IT is very high, between 4kΩ and 200kΩ. It has been also shown that the impedance of the incandescent lamp is high impedance and time-invariant, between 800Ω and 1.7kΩ, in the measurement frequency range.

Fig. 5.9 shows the impedance of the Philips oscilloscope and Samsung TV, both of them are relatively time-invariant, except the small time-variant behavior in the CENELEC bands. The oscilloscope has the lowest impedance point, below 2Ω, at the frequency of 500 kHz and the TV has the resonance impedance point, below 1Ω, at the frequency of 100 kHz.

Fig. 5.10 shows the impedance of the Samsung monitor and the Fujitsu laptop, both of them are strongly time-variant. The monitor impedance is below 0.3Ω at the frequency of 210 kHz and the laptop impedance is below 0.5Ω at the frequency of 340 kHz.

The presented measurement results showed that each device has different behavior on the power network. The time-variant behavior of the impedance of the Samsung monitor P2250 and the Fujitsu laptop is caused by the switched-mode power supply (SMPS) unit which change their behavior significantly over the time on the power line. The very low impedance in the FCC band of these two devices is mainly dependent on the EMI filter design which causes these impedances drop at specific frequencies.

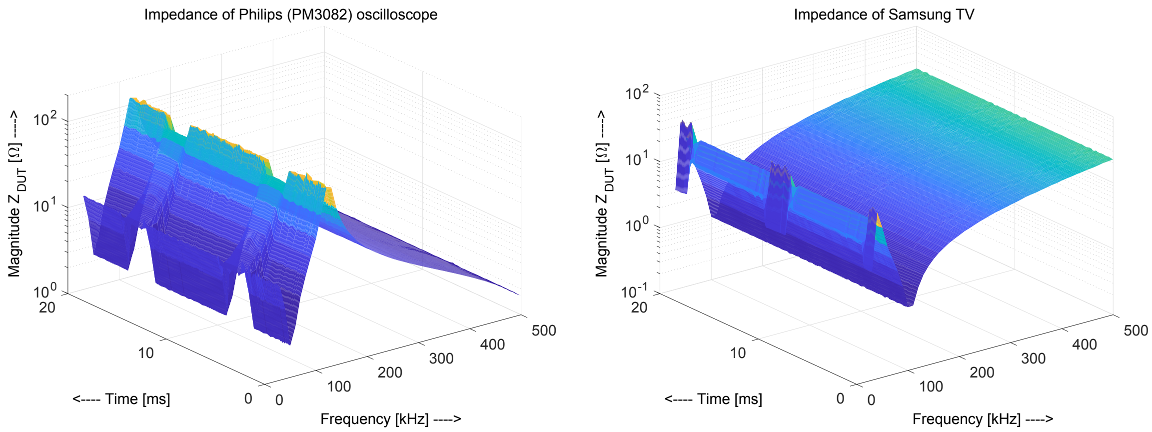

FIGURE 5.9: Time- and frequency-dependent impedances of PM3082 oscilloscope and Samsung TV [88]

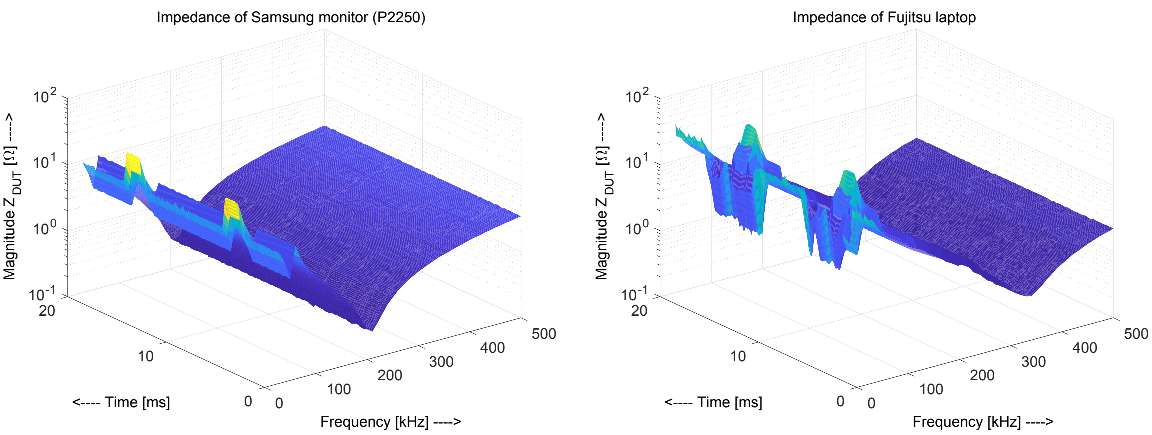

FIGURE 5.10: Time- and frequency-dependent impedances of P2250 monitor and Fujitsu laptop [88]

An overview of all performed load impedance measurements in this section is presented in Table 5.1.

TABLE 5.1: Load impedance measurements overview

Measurement type	**Measurement setup**	**Frequency observation**	**Time observation**
Load impedance	Incandescent lamp	High impedance up to 1.7kΩ	Time-invariant
Load impedance	Oscilloscope- TV	Below 1Ω in CENELEC bands	Mostly time-invariant
Load impedance	Monitor- Laptop	Below 0.5Ω in FCC bands	Time-variant

5.4 Impedance Measurement Results Evaluation

The measured impedances on the power grid are evaluated here. The evaluation method is done by estimating the access impedance on the power line based on the measured load impedances. The estimated access impedance is then compared with the measured access impedance for the same connected load devices to the power grid.

The access impedance estimation model is shown in Fig. 5.11. Load devices are connected in parallel to the power line. Therefore, the access impedance caused by the connected load devices can be calculated as the combination of the parallel load impedances and the impedance of the power line where no devices are connected. The access impedances and the single load impedances are measured in Chapter 4 and Chapter 5, respectively, and will be used for the estimation model. The estimated access impedance Z_E on the power line where different load devices are connected, can be given as

$$Z_E(f_r, t) \simeq \frac{1}{Z_A(f_r, t)^{-1} + \sum_{ii=1}^{K} Z_{DUT_{ii}}(f_r, t)^{-1}}, \tag{5.3}$$

where K is the number of the connected load devices to the power grid, Z_{DUT} is the impedance of the loads, and Z_A is the measured access impedance where no loads are connected near to the measurement point.

5.4.1 Evaluation with respect to frequency

The measured and estimated access impedance in case of various load devices are connected near to the measurement point at outlet 2 with respect to frequency are shown in Fig. 5.12 and Fig. 5.13. The same used load devices in this chapter are considered for the comparison. The measured access impedances are shown in Fig. 4.21 and Fig. 4.22, and the measured load impedances are shown in Fig. 5.9 and Fig. 5.10.

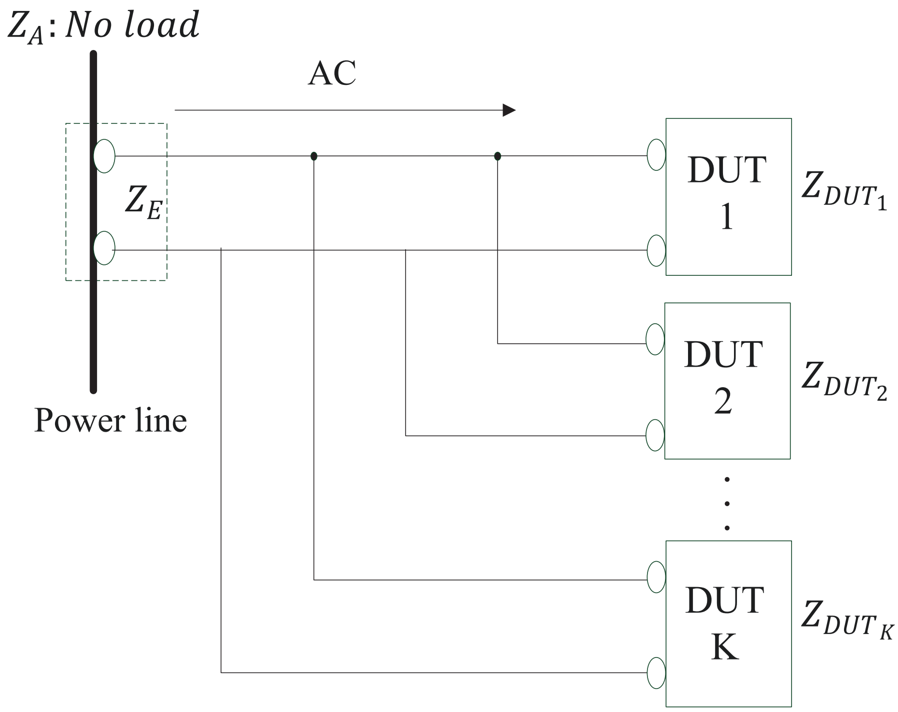

Figure 5.11: Access impedance estimation model [88]

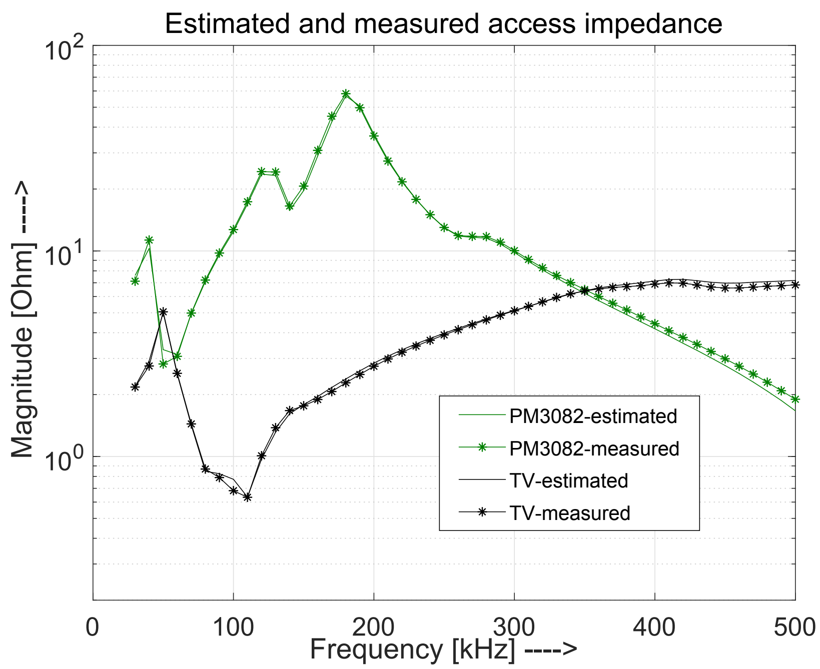

Figure 5.12: Estimated and measured access impedance where oscilloscope/TV is connected near to power outlet 2 [88]

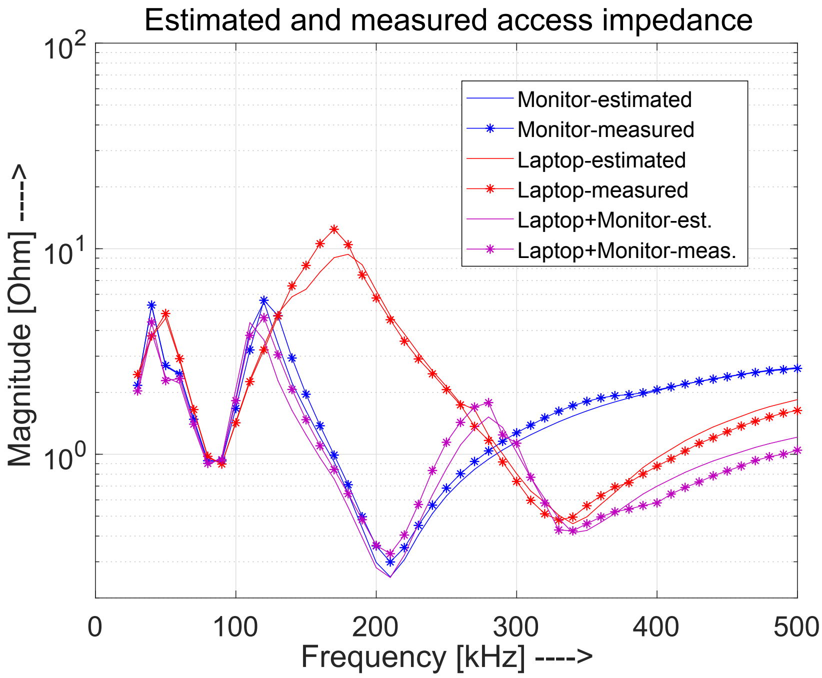

FIGURE 5.13: Estimated and measured access impedance where laptop/monitor/laptop+monitor are connected near to power outlet 2 [88]

The measured and estimated access impedances are identical in the case of the oscilloscope/TV is connected near to the measurement point. Also, the measured and estimated access impedances are almost identical with small differences in the case of the laptop/monitor is connected near to the measurement point. The reason of the small error is the time-variant behavior of the load impedances. Therefore, we compare the estimated and measured access impedances where the monitor and the laptop are connected together at power outlet 2. Nevertheless, the error is still relatively small and the evaluation method is still competitive, although these two loads have very low impedance and time-variant behavior.

5.4.2 Evaluation with respect to time

We have seen that, the estimated and measured access impedance in the case of the connected monitor and laptop to the power grid has brought small differences over the measurement frequency range, because of the time-variant behavior of these equipment. Therefore, we calculate here the access impedance of these two devices connected together on the power grid with respect to the time and frequency and compare it with the measurement.

Fig. 5.14 and Fig. 5.15 show the calculated as in (5.3) and the measured access impedance for the laptop and the monitor that are connected together at power outlet 1 and outlet 2, respectively. The measured and estimated access impedances are relatively identical and confirm the measurement method. The cyclostationary impedance behavior of each device varies on the different power outlets.

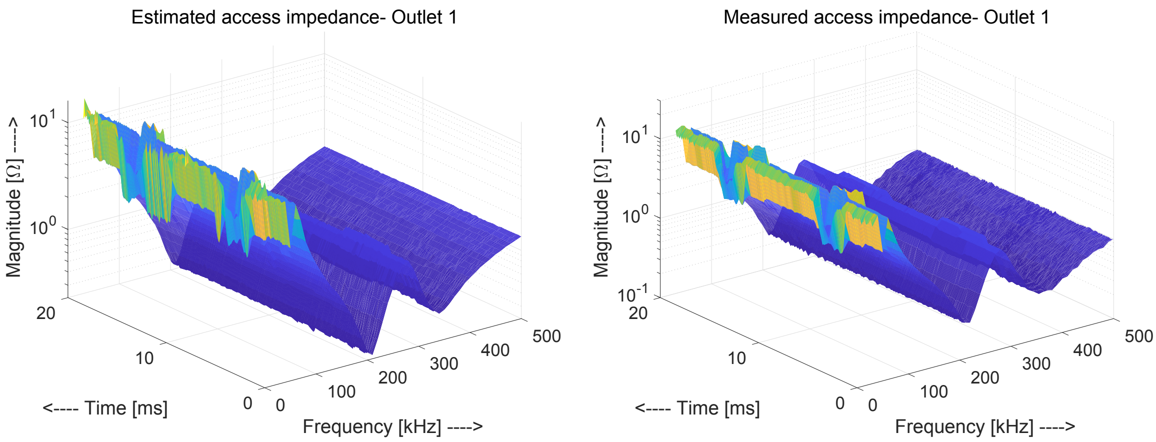

FIGURE 5.14: Estimated and measured access impedance with respect to time & frequency where laptop+monitor are connected near to power outlet 1 [88]

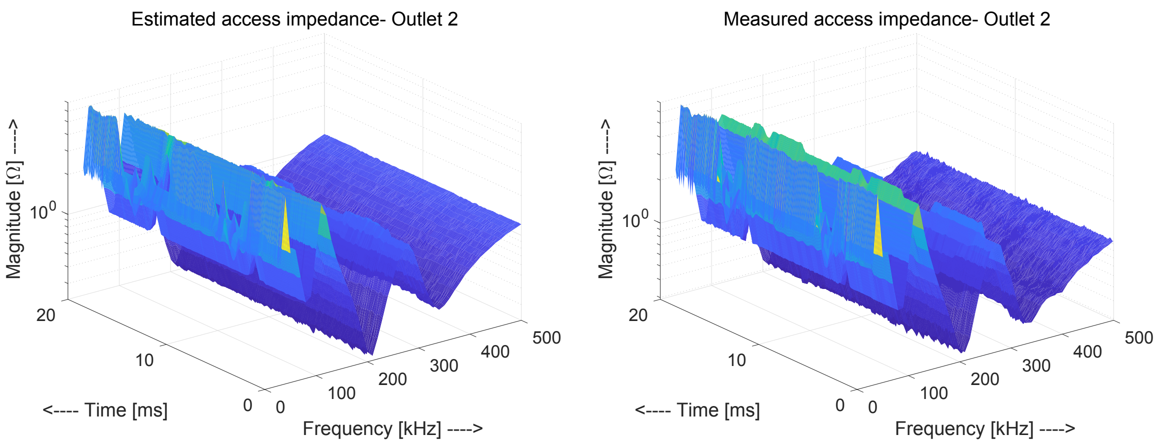

FIGURE 5.15: Estimated and measured access impedance with respect to time & frequency where laptop+monitor are connected near to power outlet 2 [88]

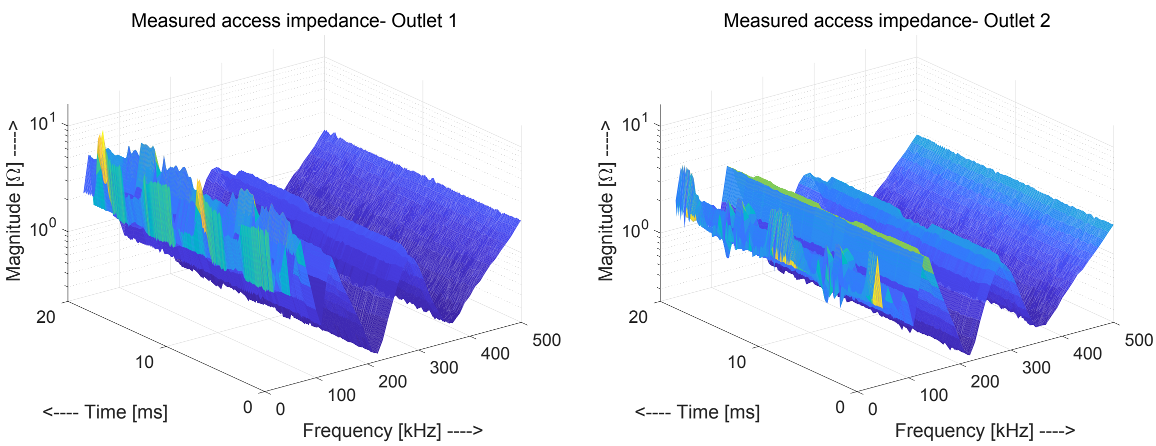

FIGURE 5.16: Measured access impedance where laptop, monitor, oscilloscope and TV are connected near to power outlet 1 & 2 [88]

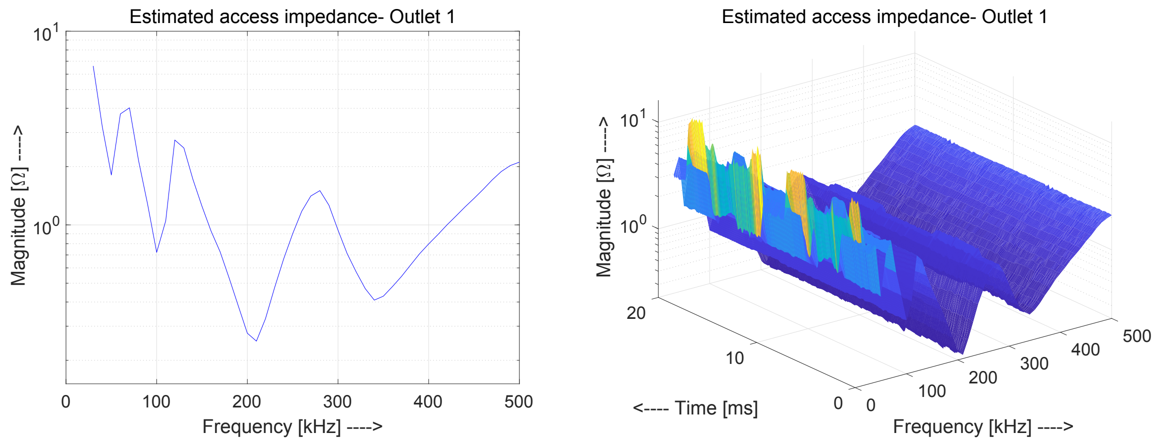

FIGURE 5.17: Estimated access impedance where laptop, monitor, oscilloscope, and TV are connected near to power outlet 1 [88]

Furthermore, the access impedance is investigated where the four presented load equipment (laptop, monitor, oscilloscope and TV) are connected next to each other at power outlets 1 and 2. Fig. 5.16 shows that the access impedance behavior on the power line is mainly dependent on the lower load impedance value, and the four impedance resonances represent the dominating load at the specific frequencies, since the connected load devices to the power grid are in parallel.

Also, the estimated and measured access impedances at the power outlet 1 are compared with respect to time and frequency, where the four equipment are connected next to each other. The measured and estimated access impedances are relatively identical and confirm the measurement procedure as shown in Fig. 5.17.

The presented evaluation results show that the measured load equipment can be used to estimate the access impedance of the power network which give us an expectation of the connected equipment and their influence on the power line.

5.5 Conclusion

This chapter has described the concepts of the load impedance measurements on the power line for frequencies between 30-500 kHz using the access impedance measurement system. An isolation transformer is used to separate the impedance of load equipment from the impedance of the power network. The impedance of the isolation transformer is measured and shown to have a high impedance and time-invariant behavior on the power line. Time- and frequency-dependent impedance measurements of equipment are presented. The measurement shows that each equipment has different impedance behavior on the power line. Some equipment are mostly time-invariant and some of them are strongly time-variant with low impedances below 0.5Ω in the FCC band. The time-variant behavior of the impedance is caused by the SMPS of the equipment and the impedance drops at specific frequencies are related to the EMI filter design. The measurement results are evaluated by comparing the estimated and measured access impedance with respect to time and frequency. The estimated and measured impedances are relatively similar and confirm the measurement method.

These impedance measurement results will allow the prediction of the connected load devices to the power grid without prior knowledge of the connected loads. Furthermore, the access impedance measurements will be used in the next chapters to develop an efficient PLC modem with optimized power amplifier regulation.

Chapter 6

Voltage and Current Modeling According to Impedance Measurement

The accurate characterization of the output voltage and output current of PLC devices with respect to time and frequency variant access impedances on the power line is essential for successful design of PLC systems. The impedance of the PLC channel is considered to be very low and time-variant. The flowing current at the output of PLC devices increases to its limit if the access impedance goes under a limit value. This problem leads to a reduction of the power amplifier output level of PLC modems and the transmitted signals. In this chapter, we present a voltage and current modeling method corresponding to time-variant access impedance measurements. The access impedances are modeled using resonant circuits. The impulse response of the designed RLC filters is calculated to find the voltage and current models. Simulation results based on the IEEE 1901.2 standard will be presented to confirm the modeling method.

6.1 Introduction

The power outlets are everywhere in homes and office buildings, making power line the largest infrastructure which can be used for data communication. However, it has remained an engineering challenge to communicate data reliably on the power grid. The reliability challenge is partly due to the varying nature of the power line and the load impedances connected to it.

Studying PLC in details implies interesting facts about the effects of the low access impedance on the communication performance. A transmitted signal by a PLC modem that reaches the receiver may be too small to be successfully received, mainly due to load impedances and the impedance of the power line as shown in Chapter 3. Therefore, in the interest of successful communication, the modeling of the signal voltage and current at the output of PLC modems in the case of very low access impedance is an important factor.

The low value of the power line access impedance has been precisely measured in Chapter 4. It has been shown that access impedances in narrowband frequencies are time-variant in some cases and frequency-dependent. The time-variant behavior caused by the switched-mode power supply unit of equipment and the low impedances are related to the EMI filter design.

This chapter presents a method to model the time-variant voltage and current of PLC devices corresponding to access impedance measurements [79]. It is organized as follows: The modeling algorithm is realized in Section 6.2. RLC circuits that simulate the impedance behavior are implemented. The impulse responses of the RLC filters are then calculated to find the time-variant voltage and current. A monitoring mechanism of the time-variant voltage and current at specific time slots is introduced as well. The evaluation of the presented method is given by simulation results in Section 6.3. Finally, Section 6.4 concludes the chapter.

6.2 Voltage and Current Modeling of PLC Devices

Analysis of the flowing current over the transmitter circuit with respect to the required output power is fundamental. The operation conditions of PLC devices and modems are presented in (3.2.1), including a model of a PLC transmitter with varying amount of load impedance shown in Fig. 3.1. It has been recognized that the power amplifier output level decreases linearly with respect to the voltage reduction caused by the low impedance amount which reduces the transmitted signal and the performance. In this section, we present a time-variant voltage and current modeling method corresponding to the access impedance behavior on the power network.

6.2.1 Access impedance modeling

The measurements presented in Chapter 4 showed that the access impedances cannot be modeled with a constant resistor over the measurement frequency range, but it presents a complex behavior. Their behavior is similar to the impedance of the simple resonant circuit (RLC circuit). Therefore, we can model the complex behavior of the measured access impedances using the resonant circuit model.

Online access impedance measurements on the power outlet 2 are presented in Fig. 4.22 where a Fujitsu laptop/Samsung monitor is connected near to the measurement point for frequencies up to 500 kHz. The Fujitsu laptop and the Samsung monitor have time-variant behavior and very low access impedances on the FCC band, below 0.5Ω and 0.3Ω at the resonance point, respectively. The access impedance where both are connected to power outlet 2 is shown in Fig. 5.15. The impedance is also very low and has two resonance points on the FCC band. As a relatively high and constant access impedance, a LevelOne network-switch is connected to the power outlet 2. The measured access impedance is shown in Fig. 6.1. The access impedance behavior is stable on the FCC-above-CENELEC band, by 6.6Ω, where a LevelOne network-switch is connected near to the measurement point.

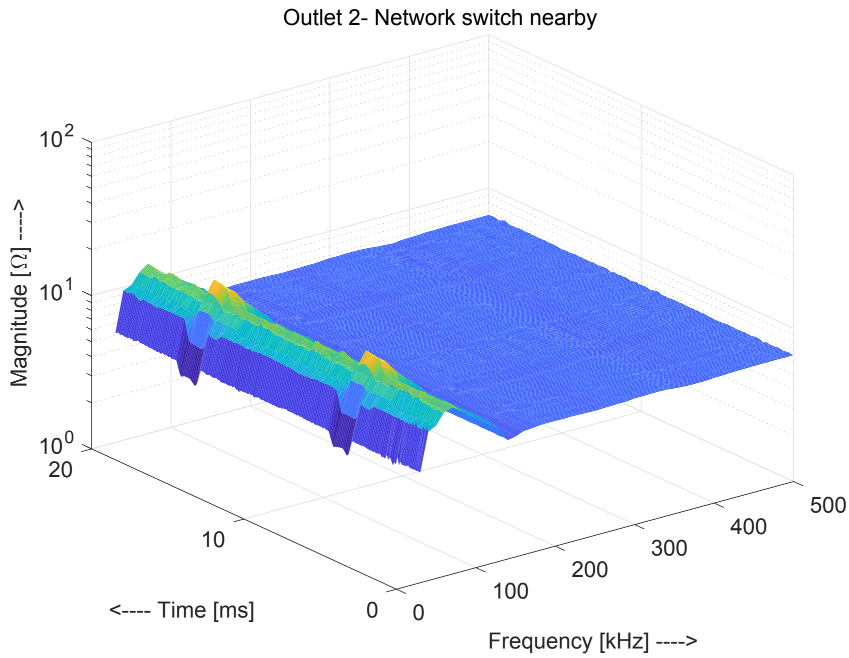

FIGURE 6.1: Access impedance measurement on power outlet 2 where a network-switch is connected near to the measurement point [79]

From the presented access impedances, three different circuit models can be considered in the frequency range from 150-500 kHz as shown in Fig. 6.2. Model 1 simulates the access impedance curve with one RLC circuit in the case of a laptop/monitor is connected to the power line. Model 2 simulates the access impedance curve with two parallel RLC circuits in the case of laptop and monitor are connected together to the power line. Model 3 simulates the access impedance curve with only one resistor in the case of a network switch is connected to the power line.

The resonant circuit models that correspond to the measured access impedances are simulated in LTspice. The parameters of the RLC circuit models are given for each access impedance case in Table 6.1. A comparison between the measured and modeled access impedances based on RLC circuits is shown in Fig. 6.3. The impedance curves are compared in the FCC-above-CENELEC frequency band since this frequency band will be used later for further simulation results. The access impedance modeling curves are mostly equal to the access impedance measurement curves and can be used equivalently.

TABLE 6.1: RLC circuit model parameters

Laptop nearby	**Monitor nearby**	**Switch nearby**
R=0.47Ω L=1.33 μH C=0.17 μF	R=0.25Ω L=1.34 μH C=0.43 μF	R=6.6Ω

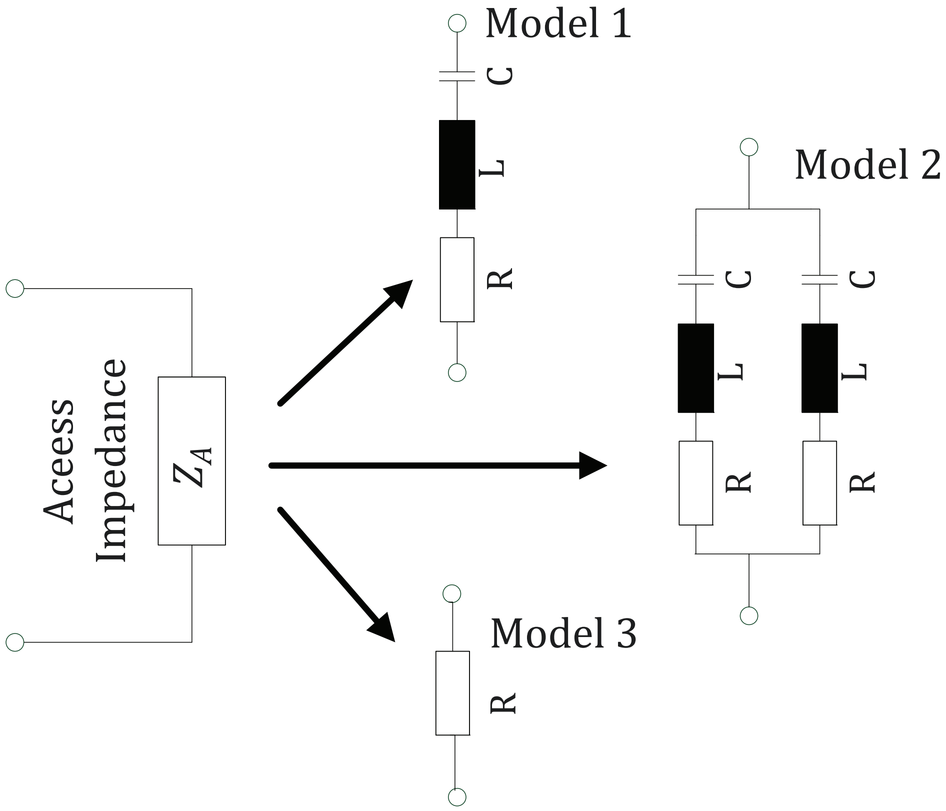

FIGURE 6.2: RLC circuit models for access impedance measurements [79]

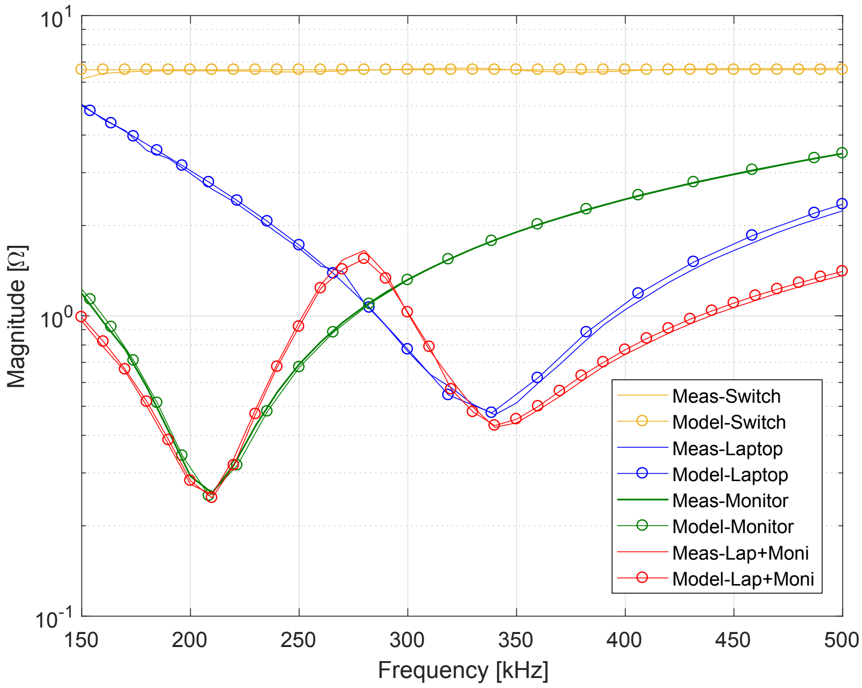

FIGURE 6.3: Access impedance measurements vs. RLC circuit models [79]

6.2.2 Voltage and current modeling method

To model and analyze the voltage and current at the transmitter side with respect to time, we simplify the transmission model presented in Fig. 3.1 to focus only on the access impedance. The schematic model of a PLC device is shown in Fig. 6.4, where the voltage $u_g(t)$ represents the voltage of the signal generator, the voltage $u_{in}(t)$ represents the voltage at the output of the PLC device that is regulated by the automatic gain control (AGC) using the multiplication factor α based on the load impedance amount, the current $i_{in}(t)$ represents the flowing current over the transmitter circuit that is also affected by the low access impedance and the internal impedance R_g, and the voltage $u_{tx}(t)$ represents the transmitted voltage at the transmitter side.

The access impedance Z_A is equivalently replaced by one of the RLC circuit models. This resonant circuit is later considered as a filter. The voltage $u_{tx}(t)$ and the current $i_{in}(t)$ are time-variant and directly affected by the access impedance. The calculation of these two parameters in the frequency domain is well investigated in Chapter 3. Therefore, we model them here in the time domain.

Since the electrical components of the circuit presented in Fig. 6.4 are passive components, we can model the voltage and current based on the linear system theory as shown in Fig. 6.5. Considering the system as a black box, we can find the requested voltage and current model using the impulse response of the designed RLC circuit models. The voltage model $u_{tx}(t)$ is calculated from $u_{in}(t)$ using the impulse response of $h_u(t)$. The current model can be found

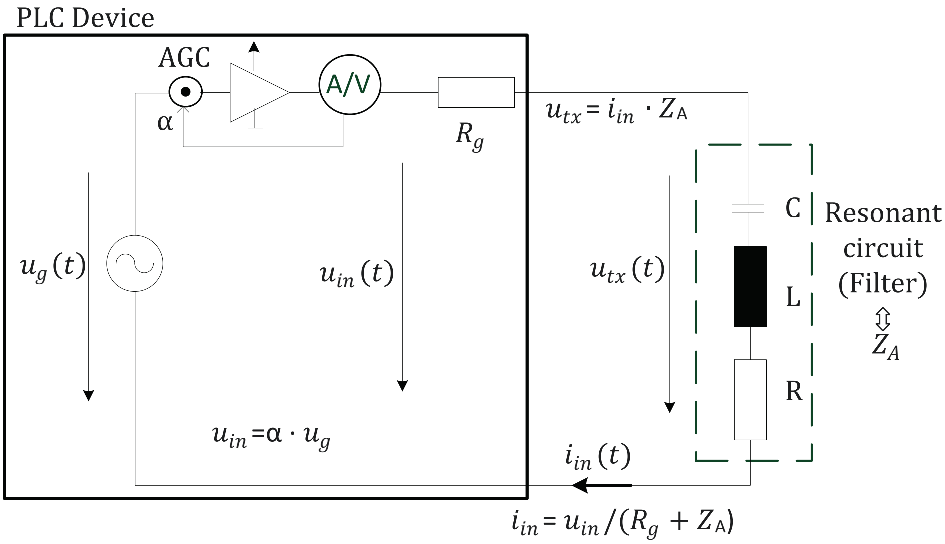

FIGURE 6.4: Simplified schematic model of a PLC transmitter [79]

in two ways as shown in the modeling system. It can be computed from the modeled signal $u_{tx}(t)$ using the impulse response of $h_{i2}(t)$ or directly from $u_{in}(t)$ using the impulse response of $h_{i1}(t)$. The current and voltage are mathematically computed as

$$\begin{aligned} u_{tx}(t) &= u_{in}(t) * h_u(t) \\ i_{in}(t) &= u_{in}(t) * h_{i1}(t) \\ i_{in}(t) &= u_{tx}(t) * h_{i2}(t), \end{aligned} \tag{6.1}$$

where (*) represents the convolution operation, $h_u(t)$, $h_{i1}(t)$, and $h_{i2}(t)$ represent the impulse responses of the RLC circuit models.

The impulse response of $h_{i1}(t)$ can be described as a combination of the two filters $h_u(t)$ and $h_{i2}(t)$ as

$$h_{i1}(t) = h_u(t) * h_{i2}(t). \tag{6.2}$$

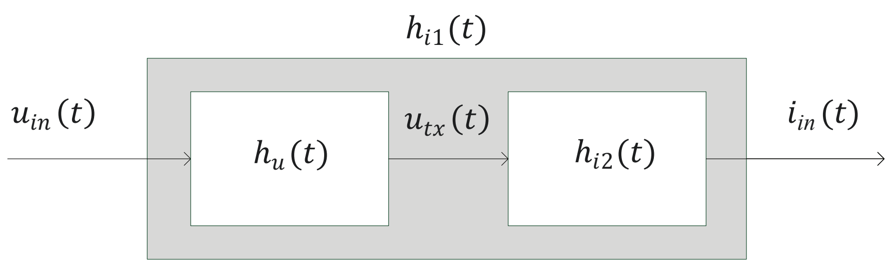

FIGURE 6.5: Black box model [79]

TABLE 6.2: Transfer function of resonant circuits in S-domain

	Model 1	Model 3
$H_u(s)$	$\frac{s^2LC+sCR+1}{s^2LC+sC(R_g+R)+1}$	$\frac{R}{R_g+R}$
$H_{i1}(s)$	$\frac{sC}{s^2LC+sC(R_g+R)+1}$	$\frac{1}{R_g+R}$
$H_{i2}(s)$	$\frac{sC}{s^2LC+sCR+1}$	$\frac{1}{R}$

6.2.3 Filter design

To find the impulse response of the presented circuit models, filter design based on Laplace transformation is considered. The transfer function of the RLC filters in S-domain for the voltage and current signals are found from the simplified circuit presented in Fig. 6.4. Table 6.2 describes the transfer function of the filter models. The transfer function of the resonant circuit Model 2 is not given in the table because of the long representation with denominator polynomials of factor 4.

The time discrete impulse response of the filters is found by converting the transfer function form S-domain to Z-domain using the mathematical First-order hold (FOH) method [107]. The step response of filter Model 1 in the time continuous representation matches the time discrete representation as shown in Fig. 6.6. The simulation results show that the step response of the filter $H_{i2}(s)$ has a longer duration compared to $H_{i1}(s)$, because of the lower damping factor in the denominator. Therefore, the filter $h_{i2}(t)$ will not be used for the current modeling and the filter $h_{i1}(t)$ is only studied.

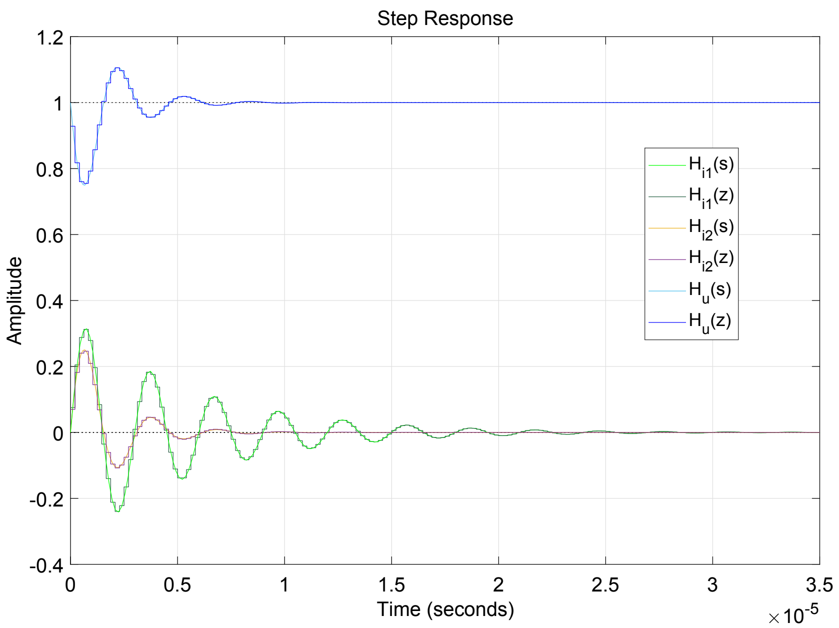

FIGURE 6.6: Step response of filter Model 1 [79]

The frequency response of the transfer function H_{i1} in S- and Z-domain for different access impedance models is shown in Fig. 6.7. The simulation considers the resonant circuit Model 1 for the access impedance of laptop/monitor is connected to the power line and the circuit Model 2 for the access impedance of laptop and monitor are connected together to the power line. The Model 3 is not given, since the impedance is flat and no resonance point exists. It has been shown that the filter models respond at the same resonance points with a certain magnitude and can be used for the current modeling.

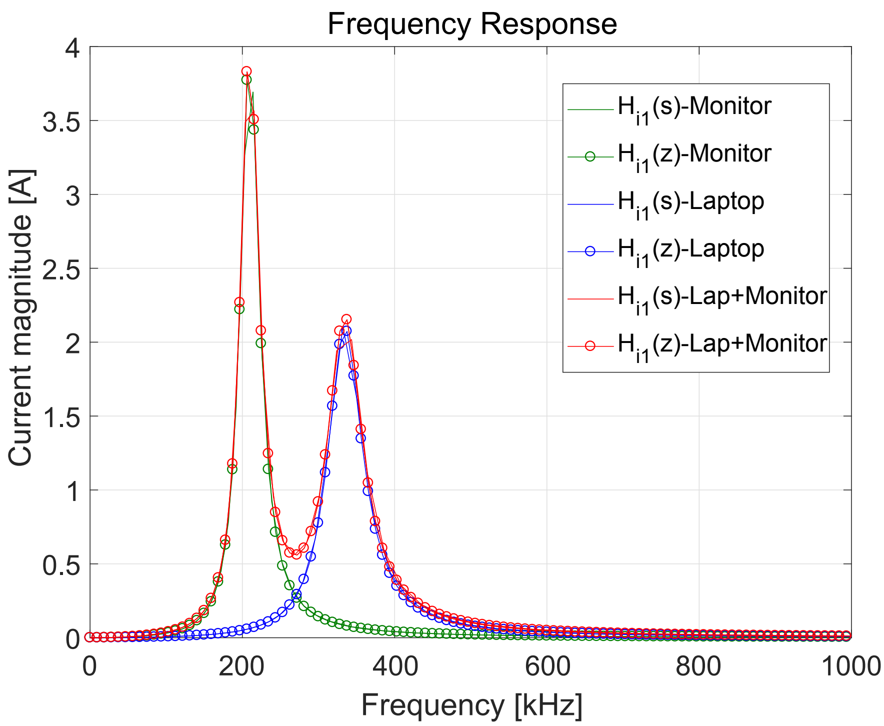

FIGURE 6.7: Frequency response of H_{i1} in S- and Z-domain for different access impedance models [79]

6.2.4 Time-variant monitoring mechanism

Analyzing the measured access impedances, two or three changes have been observed in most cases with respect to the measurement time over one cycle of the mains. Thus, the time-variant voltage and current at specific time slots, where the access impedance is constant, can be determined using a combination of parallel resonant circuits with a toggle switch as shown in Fig. 6.8.

The schematic model presented in Fig. 6.4 is further simplified. The signal generator, AGC, and the PA are compensated with the voltage source $u_{in}(t)$, taking into account their influences. The number of the resonant circuits is given according to the number of the time variation of the access impedance. The unconnected RLC circuits to the toggle switch S are grounded. The switch S toggles between the RLC circuits for each time slots to monitor the voltage and current behavior at the specific time slots where the impedance is relatively constant.

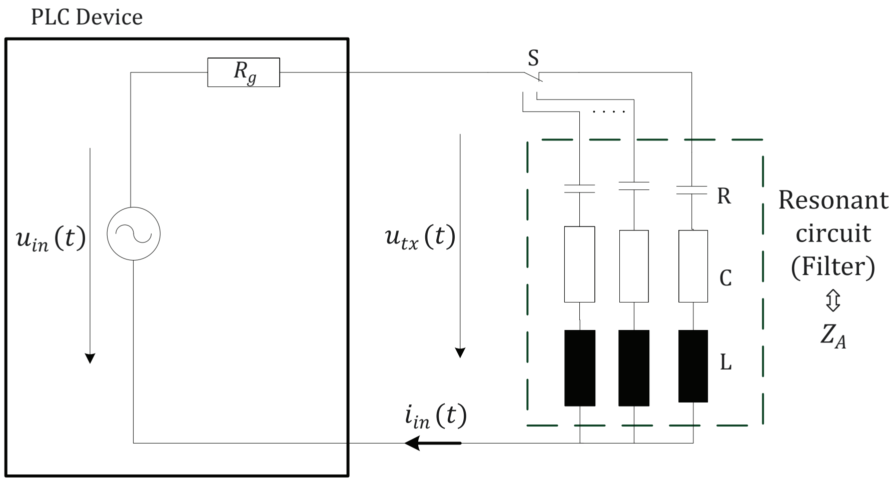

FIGURE 6.8: Voltage and current monitoring model [79]

The calculation of the voltage and the current at specific time slots as a combination of parallel resonant circuits is given as

$$\begin{aligned} u_{tx}(t) &= \sum_{j=1}^{J} u_{in\_j}(t) * h_{u\_j}(t), \\ i_{in}(t) &= \sum_{j=1}^{J} u_{in\_j}(t) * h_{i1\_j}(t), \end{aligned} \tag{6.3}$$

where J represents the number of the parallel filters (mostly 2 or 3) and $u_{in\_j}(t)$ is the generated signal for each time slot where the access impedance is constant.

The signal $u_{in\_j}(t)$ toggled by the switch can be found as

$$u_{in\_j}(t) = u_{in}(t) \cdot g_j(t), \tag{6.4}$$

where $g_j(t)$ represents a weighting function that simulates the switch process. An example of the timing diagram that represents the behavior of the weighting function $g_j(t)$ is shown in Fig. 6.9.

The function $g_j(t)$ is mathematically described as

$$\begin{cases} g_j(t) \in \{0; 1\} \\ \sum_{j=1}^{J} g_j(t) = 1 \\ g_j(t) = g_j(t + \nu \cdot T_0), \end{cases} \tag{6.5}$$

where T_0 the fundamental period equal to 20ms and $\forall \nu \in \mathbb{Z}$.

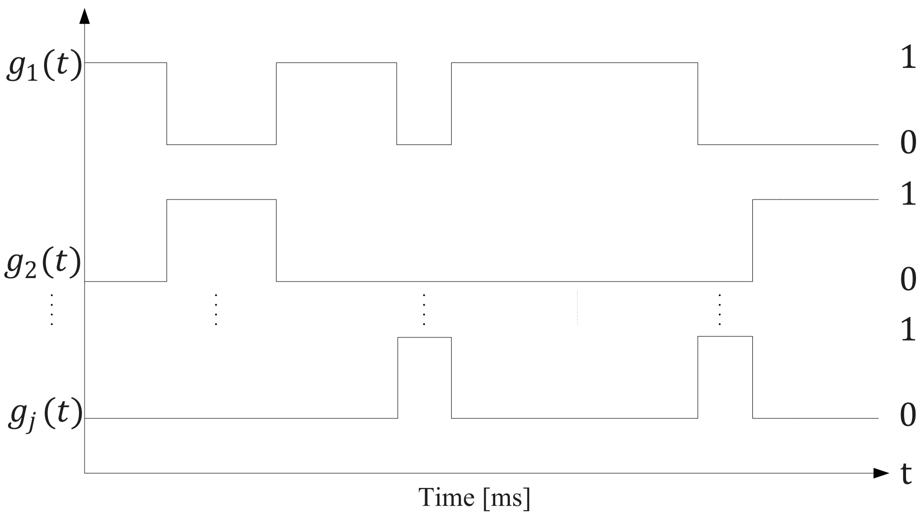

FIGURE 6.9: Timing diagram of weighting function $g_j(t)$ [79]

6.3 Evaluation of Modeling Method

In order to evaluate the presented modeling method, we introduce a simulation environment with a PLC device that transmits signals on the power line for the different access impedance values.

6.3.1 Simulation parameters

The transmitted signal by a PLC device is implemented with respect to the IEEE 1901.2 standard. The simulation results can be equivalently considered by other PLC standards. The physical layer specifications of IEEE 1901.2 is presented in [68]. We select the FCC-above-CENELEC frequency band, from 154.6875 to 487.5 kHz, since the measured access impedances have resonances in this frequency range. The FFT length is 256 and the subcarrier spacing is 4.6875 kHz. The number of the used subcarriers is 72 and the sampling frequency is 1.2 MHz.

The parameters of the PLC device are implemented according to the new version of the transmitter modem presented in Chapter 3. The Analog Front End AFE032 of Texas Instrument is considered and conforms the FCC-above-CENELEC band [108]. The voltage U_{amp} is selected to be 10V and the current output of the amplifier is limited to 1.5A. The effective voltage at the output of the transmitter shall not exceed 134 dBµV as defined in EN-50065-1 [8]. The internal impedance R_g is set to 2Ω.

6.3.2 Simulation results

The preamble signal in the IEEE 1901.2 consists of 9.5 OFDM symbols and these will be used for the evaluation of the modeled voltage and current signals. The reason of that is the generated symbols are chirp signals. These chirp signals have special properties in OFDM systems that allow us to analyze the resulted voltage and current. In particular, they show resonances in the voltage and the current signals at the time domain that are caused by the low access impedances. The data frames can be equivalently evaluated.

Fig. 6.10 shows the voltage $u_{in}(t)$ at the output of the PLC device for the different access impedance values. The voltage $u_{in}(t)$ is stable to 10V in the case of flat and relatively high access impedance (voltage control area) and reduces in the case of low access impedance with resonances (current control area).

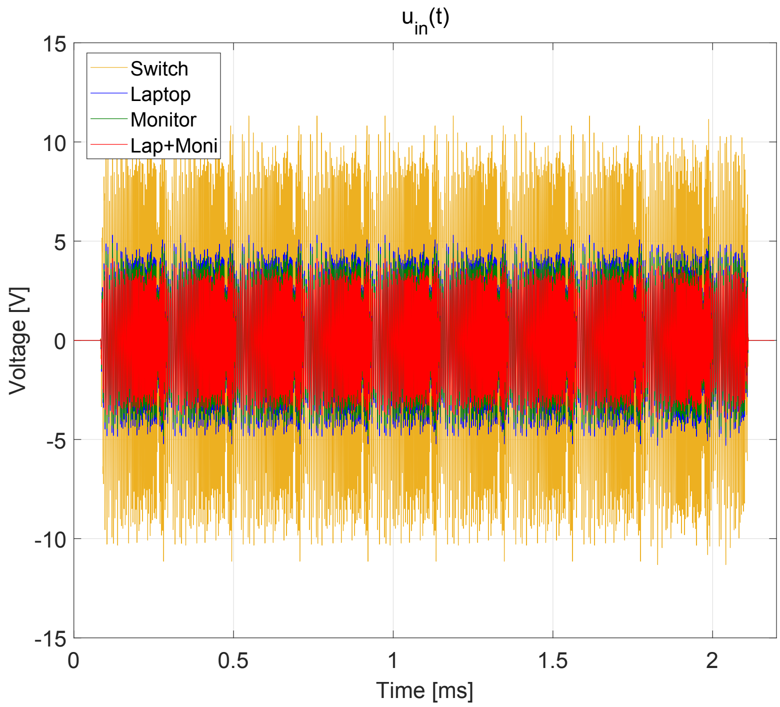

FIGURE 6.10: The voltage $u_{in}(t)$ of preamble symbols for different access impedances [79]

Fig. 6.11 shows the voltage $u_{tx}(t)$ for 9.5 preamble symbols and for one preamble symbol (for clarification) at the transmitter side according to the different access impedance values. The voltage $u_{tx}(t)$ remains constant for the high impedance value and decreases for low impedance values. The chirp signals shape behaves correspondingly to the access impedance curves and shows resonances in the time domain signals.

Fig. 6.12 shows the current $i_{in}(t)$ for 9.5 preamble symbols and for one preamble symbol at the output of a PLC device according to the different access impedance values. The current $i_{in}(t)$ is stable below 1.5A for a high impedance value and increases for low impedance values. This increment is realized to meet the power consumption of the PLC device and limited to 1.5A root mean square (RMS) value. The shape of chirp signals behaves also correspondingly to the access impedance curves and shows resonances in the time domain signals.

It can be recognized that the behavior of the current and voltage signal is mainly influenced by the measured low access impedances.

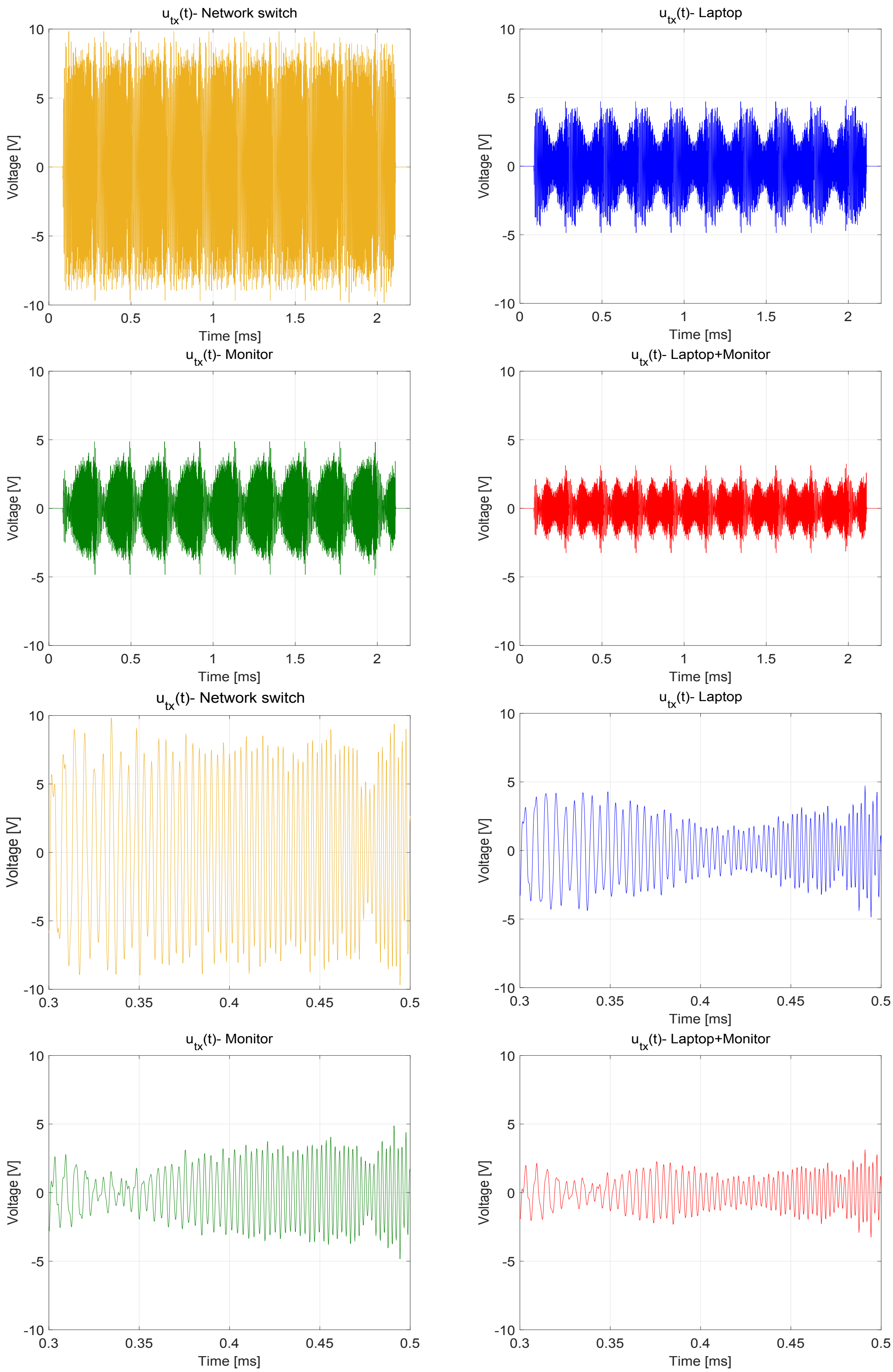

FIGURE 6.11: The voltage $u_{tx}(t)$ of preamble symbols for different access impedances

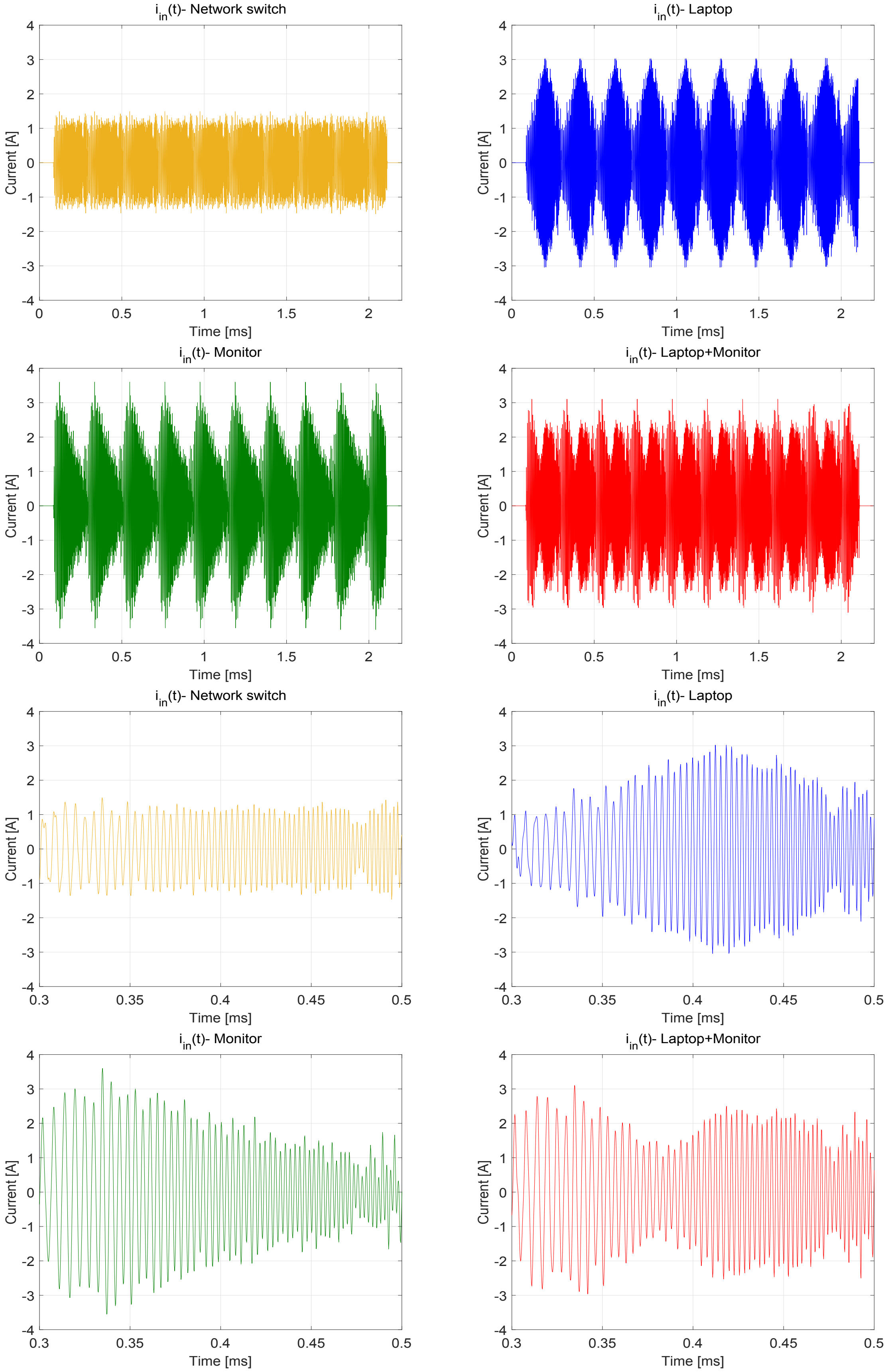

FIGURE 6.12: The current $i_{in}(t)$ of preamble symbols for different access impedances

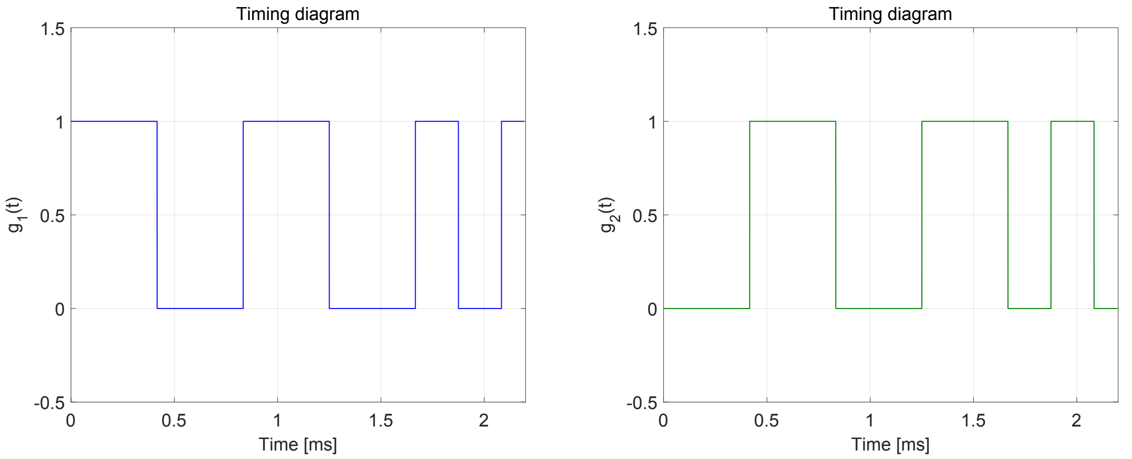

FIGURE 6.13: Timing diagram example of $g_1(t)$ & $g_2(t)$ [79]

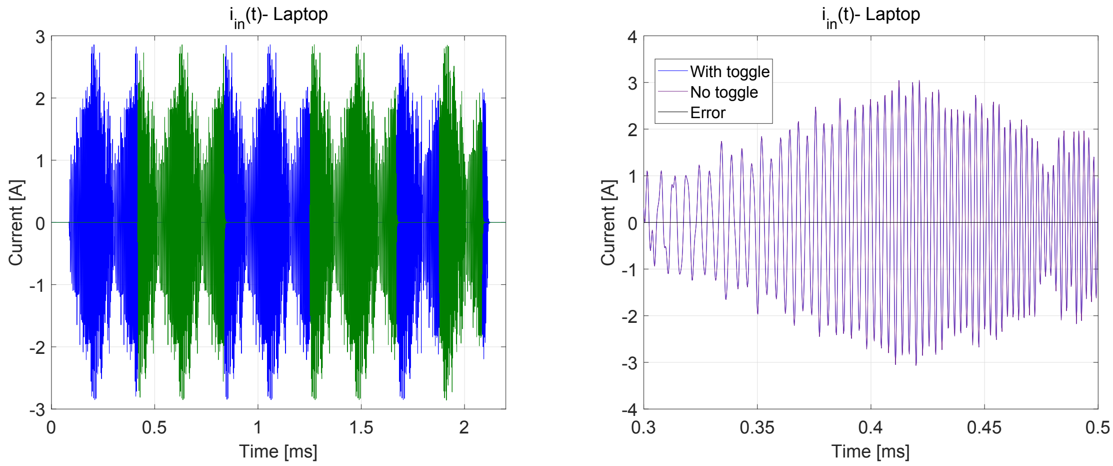

FIGURE 6.14: Verification of the time-variant current analysis method [79]

The analysis of the current of the preamble signal at specific time slots with respect to the access impedance where a laptop is connected on the power line is shown Fig. 6.14. The two weighting functions $g_1(t)$ & $g_2(t)$ are the timing diagram of the toggle switch and shown in Fig. 6.13. The analysis method at specific time slots is verified by comparing the current of the preamble in the case of using the toggle switch and the normal case with one filter. The difference error between the two signals is calculated. It has been shown that the error is small and negligible as depicted by one symbol of the preamble.

6.4 Conclusion

This chapter has presented models of the transmitted voltage and current of PLC devices and modems corresponding to time-variant access impedances. The modeling method based on the impulse response of RLC filters that simulate the behavior of the measured access impedances. Moreover, a mechanism to observe the time-variant voltage and current at specific time slots is introduced. The investigated voltage and current models are evaluated and verified by simulation results based on the IEEE 1901.2 standard. The influence of low access impedances by reducing the transmitted signal and increasing the flowing current through PLC devices has been shown.

Chapter 7

TX-Signal Optimization by Low Access Impedance

Low access impedances on the power grid lead to reductions of the transmitted signals by PLC modems. Therefore, the optimization of the transmitted signal by PLC devices in the case of low access impedances will be presented here. The optimization method at the transmitter side is performed by switching off subcarriers in frequencies with low access impedances and high current which increases the signal level on the other subcarriers with suitable access impedances and the achievable data rate as well. The optimal number of suppressed subcarriers that delivers the maximum profit is determined. The gain of the optimization method with respect to the packet error rate over signal to noise ratio is evaluated by simulation results based on the IEEE 1901.2 standard.

7.1 Introduction

PLC smart metering systems are the application with the greatest support from the industry and utilities in the narrowband frequencies. These metering systems depend on highly reliable and available communication networks. A great number of distributed smart meters must be managed remotely, thus data must be transferred reliably and securely between spatially separated points.

In the case of PLC, it is very difficult to verify a modem, since parameters of the PLC transmission channel that maybe crucial to system reliability expose a highly frequency- and time-variant behavior. One of the most restrictive requirement is the compliance with the EN 50065-1 standard for signaling on low voltage electrical networks in context of the impedance magnitude.

Furthermore, the power consumption of the available modems and applications has to be low and limited. This power consumption limitation leads to a reduction of the power amplifier output level of PLC devices to meet the very low amount of a load impedance on the power line channel, as discussed in Chapter 3. Therefore, in order to achieve a useful signal level, the transmitted signal voltage has to be adapted to match the actual impedances on the power grid.

In this chapter, we present an optimization method to increase the performance of OFDM PLC transmission systems by selecting and suppressing the transmitted signal (voltage) on the subcarriers with a low access impedance which increases automatically the transmitted signal (voltage) on the other subcarriers [109]. Hence, the SNR is significantly increased and the achievable data rate as well. This optimization is done under the conditions of the power consumption limitation of PLC applications and the access impedance frequency selectivity. Furthermore, the optimal number of suppressed subcarriers will be determined and the validation of the proposed method will be verified with respect to packet error rate measurements for the online measured access impedances.

This chapter is organized as follows: In Section 7.2, we introduce a simplified model of a PLC transmitter on the power line in the case of a low access impedance. The optimization method to improve the data rate is presented in Section 7.3. An algorithm to determine the allowed number of suppressed subcarriers that achieves the maximum gain is investigated in Section 7.4. Section 7.5 evaluates the performance of the optimization method by numerical results based on the IEEE 1901.2 standard for different access impedance measurements. Finally, Section 7.6 concludes the chapter.

7.2 Communication Model over PLC

The behavior of PLC devices on the power line channel is represented by the model of transmitter and receiver operating on the same channel as shown in Fig. 3.1. The transmitted signal is time- and frequency-variant and directly affected by the low impedance on the power line as presented in Chapter 3. Hence, the transmitted signal has to be optimized in this case.

7.2.1 Simplified model of transmission

Fig. 7.1 presents a simplified model of the transmission between two PLC devices. The PLC transmitter is simplified by the voltage of the generator $U_g(f)$, the power amplifier, and the internal impedance R_g. The voltage $U_{in}(f)$ represents the signal at the output of the transmitter, $U_{tx}(t, f)$ represents the signal at the transmitter side, and the current $I_{in}(t, f)$ represents the flowing current at the transmitter. The power amplifier output level is regulated by the multiplication factor α based on voltage and current measurements, as described in Section (3.2.1). The PLC channel is represented by the access impedance $Z_A(t, f)$ that affects the transmitted signal at the power line channel, the transfer function $H_c(t, f)$, and the additive noise $N(t, f)$. The PLC receiver is simplified by the resistor R_{rx} that assumes to be high impedance.

The calculation of the transmitted signal $U_{tx}(t, f)$ and the current $I_{in}(t, f)$ will be here briefly discussed. The detailed calculation of these two parameters is presented in Section (3.2.1). The multiplication factor α is determined in terms of α_u and $\alpha_i(t)$ as:

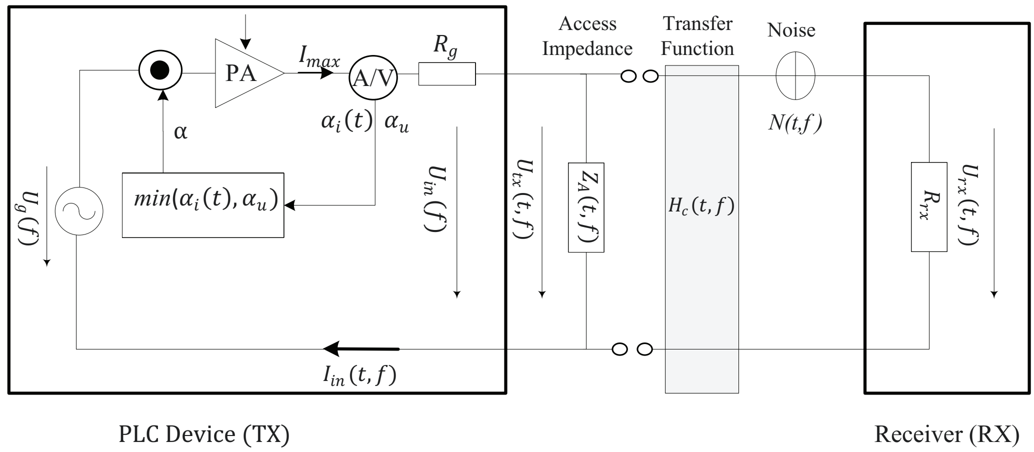

FIGURE 7.1: Simplified model of PLC transmission

- If $\alpha_i(t) \geq \alpha_u$, then $\alpha = \alpha_u$ and the output voltage of the PA is defined using the constant α_u to fulfill the voltage level of the EN 50065-1. The optimization method cannot be utilized in this case and all subcarriers are used in the transmission.

- If $\alpha_i(t) < \alpha_u$, then $\alpha = \alpha_i(t)$ and this case represents the interesting situation of signal reduction that we want to optimize. The factor $\alpha_i(t)$ is determined as

$$\alpha_i(t) = \frac{I_{max}}{I_{total}}, \tag{7.1}$$

where I_{max} is the maximum flowing current over the PA and I_{total} is the total flowing current at the transmitter side for each subcarrier and defined as

$$I_{total} = \sqrt{\sum I_{in}(t,f)^2}. \tag{7.2}$$

For each subcarrier, the flowing current at the transmitter side $I_{in}(t,f)$ is calculated from Fig. 7.1 as

$$I_{in}(t,f) = \frac{U_{in}(t,f)}{Z_A(t,f) + R_g}. \tag{7.3}$$

The voltage at the output of the PLC transmitter $U_{in}(f)$ is determined as

$$U_{in}(f) = \alpha \cdot U_g(f). \tag{7.4}$$

As a consequence, the transmitted signal $U_{tx}(t,f)$ for each subcarrier can be computed as

$$U_{tx}(t,f) = I_{in}(t,f) \cdot Z_A(t,f). \tag{7.5}$$

7.3 Optimization Method

The influence of the low access impedance on PLC systems by reducing the transmitted signal and the achievable data rate is introduced in Chapter 3. The achievable data rate has been reduced up to 90% in the worst case. Hence, the development of an optimization method to improve the transmitted signal and the achievable data rate in the case of a low access impedance is required.

The optimization method of the OFDM PLC systems is described in Fig. 7.2. The idea is to set the voltage as zero for the subcarriers that reduce the transmission performance where the access impedance is low. The amplitude adjusting is performed by finding the subcarriers that have the maximum current $I_{in}(t, f)$ and switching them off as long as the power amplifier output level is regulated using the factor $\alpha = \alpha_i(t)$. As a result, the internal power loss of the power amplifier is reduced and a higher signal to noise power ratio level is achieved on the other subcarriers. The higher SNR leads to a better data rate than the state of the art transmission.

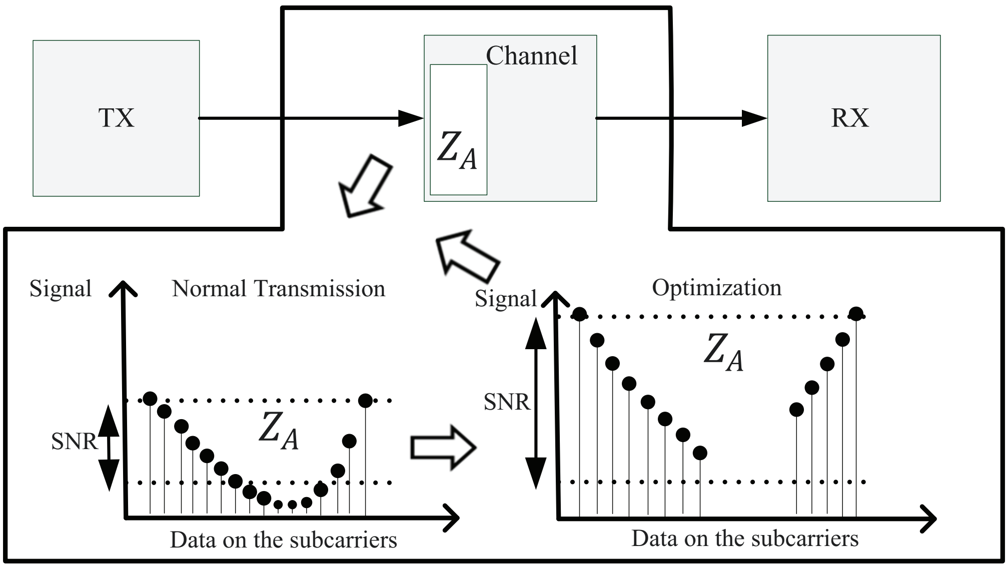

FIGURE 7.2: Optimization method description [77]

7.3.1 Data rate improvement

In this section, the optimization method shown in Fig. 7.2 will be applied to improve the achievable data rate presented in Chapter 3. The computation of the achievable data rate by OFDM PLC systems is presented in Section (3.2.3). For the simulation environment, we consider the same parameters as in (3.2.4).

The transmitted signal is implemented with respect to the PRIME standard [75]. The transmitter circuit parameters are related to the analog front end AFE031 of Texas Instrument and conform the EN 50065-1 CENELEC A-band [81]. The access impedance is related to the EN 50065-1, measurements were done by Dostert shown in Fig. 3.3, measurements were done by CEPRI shown in Fig. 3.4, phase B-N, and measurements were done in Austria shown in Fig. 3.5, phase 1 & 3. In order to realize a realistic simulation environment, the channel attenuation and the noise are based on the measured values by CEPRI as shown in Fig. 3.6, 26# (L=250m) and Fig. 3.7, phase A-N, respectively.

The optimized data rate for the different access impedances based on suppressing subcarriers is shown in Fig. 7.3. The places of the switched off subcarriers are corresponding to the low access impedance which results in a higher amplitude level and a higher SNR as well. The optimization method cannot be applied in the case of access impedance is related to the EN 50065-1 because of the high impedance value. The achievable data rate has been increased significantly compared to the state of the art transmission shown in Fig. 3.8. The solid lines denote the optimized transmission and the dashed lines denote the state of the art transmission. The difference between the solid and dashed lines of the same color represents the SNR gain between the normal and optimized transmission.

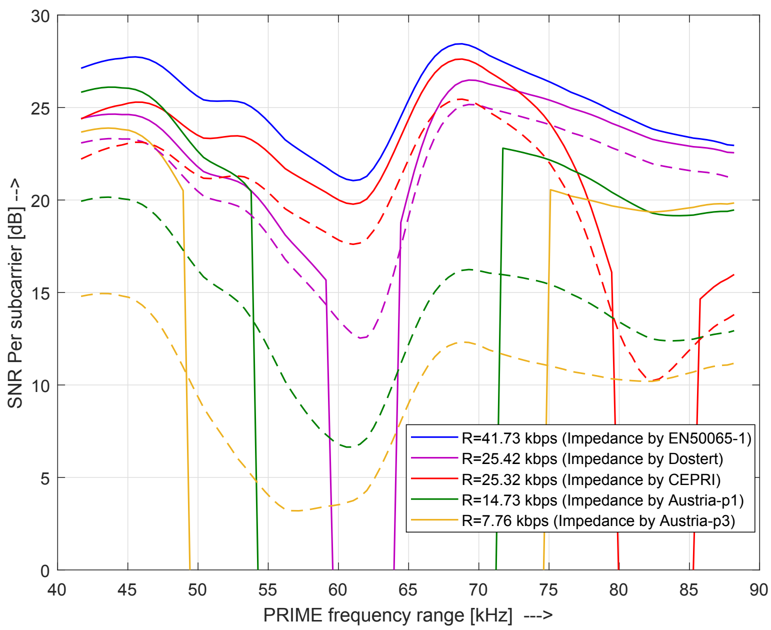

Figure 7.3: The achievable data rate in the state of the art transmission and the optimized transmission for different access impedances

Table 7.1 presents the simulation results for the optimized transmission for different access impedances. It describes the total current at the transmitter I_{total}, the effective voltage at the output of the transmitter $U_{tx,eff}$, the effective power at the output of the generator $P_{in,eff}$, the effective power at the output of the transmitter $P_{tx,eff}$, and the achievable data

Table 7.1: Simulation results for optimized transmission in the case of low access impedances

$Z_A[\Omega]$	I_{total} [A]	$U_{tx,eff}$ [dBµV]	$P_{in,eff}$ [W]	$P_{tx,eff}$ [W]	R [kbps]
EN 50065-1	0.32	133.9	1.63	1.57	41.73
Dostert	1.4	131.35	6.31	4.14	25.42
CEPRI	1.4	131.3	6.06	4.03	25.32
Austria- P1	1.4	128.5	5.98	3.76	14.37
Austria- P3	1.4	126.2	5.12	2.94	7.76

rate. Compared to the simulation results for the normal transmission shown in Table 3.1, the optimization method produces gains in all simulation parameters. The effective current I_{total} never reaches the limit in all cases and the effective voltage at the output of the transmitter $U_{tx,eff}$ has been increased. The power consumption requirement for the power amplifier has been improved in context of the effective powers $P_{in,eff}$ and $P_{tx,eff}$.

7.4 Restriction of Suppressed Subcarriers

The implementation of the optimization method presented in Fig. 7.3 is based on a greedy algorithm which means that the subcarriers are suppressed until $\alpha_i(t) \geq \alpha_u$. However, this implementation does not consider the allowed number of the suppressed subcarriers, since the channel coding of the PRIME standard on the transmitter and the receiver is not examined. Therefore, the number of the suppressed subcarriers has to be restricted for the successful realization.

The restricted algorithm of the suppressed subcarriers is described in Table 7.2. The allowed number of subcarriers to be suppressed is determined with respect to two conditions:

- The switched off subcarriers number does not exceed the limit N_{limit}. This limit specifies the threshold where the channel coding still works properly. Suppressing subcarriers more than N_{limit} breaks the transmission and the channel coding. Therefore, N_{limit} is a constant and has to be specified for every transmission mode and modulation scheme.
- The multiplication factor $\alpha = \alpha_i(t)$ $(\alpha_i(t) < \alpha_u)$.

The allowed number of subcarriers to be switched off N_{limit} will be later specified for the simulation environment.

7.4.1 Simulation environment

In order to show the applicability of the optimization method on other NB-PLC standards, the OFDM-based PLC transmitter structure, as well as the corresponding receiver structure, are designed in this section based on the IEEE 1901.2 standard [68]. Both transmitter and receiver, are implemented to evaluate the optimization method with more restricted conditions, considering the number of the suppressed subcarriers.

TABLE 7.2: Subcarriers suppression algorithm implementation

Algorithm 1: Subcarriers suppression

1: assign the allowed number of subcarriers N_{limit} that can be suppressed for each transmission mode.
2: **if** $\alpha_i(t) \geq \alpha_u$ **then**
3: no optimization applied.
4: **else**
5: **while** $((\alpha_i(t) < \alpha_u)$ & (No. of suppressed subcarriers $<= N_{limit}$))
6: find the subcarriers with the maximum current $I_{in}(t, f)$.
7: set the voltage $U_g(f)$ of the subcarrier with the maximum current as zero.
8: compute α again for the new voltages.
9: **end**
10: **end**

For the simulation environment, the following settings are chosen. We select the FCC-above-CENELEC frequency band, from 154.6875 to 487.5 kHz, since the measured access impedances have resonances in this frequency range. The sampling frequency has been chosen to 1.2 MHz, while the FFT size is 256, i.e. the subcarrier spacing accounts for 4.6875 kHz. The number of the used subcarriers is 72 and the frame control header (FCH) length is 12 symbols.

For data transmission, the modulation schemes differential binary phase shift keying (DBPSK) and differential quadrature phase shift keying (DQPSK) are selected for the comparison. The FCH data are additionally repeated six times in the Super-ROBO mode with coherent modulation BPSK and QPSK.

In all modes, data are protected by the rate 1/2 convolutional code with generator polynomials 171 and 133 and interleaved within the whole packet. Non-FCH data are encoded with an appropriately shortened Reed Solomon (RS) Code, which is based on RS (255, 239) for DBPSK and DQPSK mode.

Furthermore, each OFDM symbol is windowed by a raised–cosine slope of 8 samples at its beginning and end for spectral forming. The 8 tail and 8 head shaped samples of the symbol from each side of the symbol are overlapped with the tail and head samples of adjacent symbols. The length of the cyclic prefix is set to 30 for FCH and Non-FCH data. Finally, the preamble symbols are transmitted at the beginning of each data packet. The preamble signal consists of 9.5 symbols in the time domain.

Since there is no standardized receiver, we tried to find fair solutions, which include synchronization according to [110], and soft-input Viterbi decoding.

The parameters of the simulation environment based on the IEEE 1901.2 are summarized in Table 7.3.

Since the transmitter and receiver are implemented for FCC-above-CENELEC frequency band, we select for the simulation access impedances with low values in this frequency band. The access impedances where a Fujitsu laptop/Samsung monitor is connected near to the

Table 7.3: Parameters of IEEE 1901.2

Frequency range	154.6875-487.5 kHz
Sampling frequency	1.2 MHz
OFDM	
FFT length	256
Length of cyclic prefix	30
Number of symbols in preamble	9.5
Subcarrier spacing	4.6875 kHz
No. of carriers used (one–sided)	72
Forward Error Correction	Reed Solomon code, Convolutional code, Repetition code
Modulation	DBPSK, DQPSK

measurement point are considered and shown in Fig. 4.22. These impedances have very low values on the FCC band, below 0.5Ω and 0.3Ω at the resonance point, respectively. Moreover, the access impedance where both are connected to the power line is also considered with two resonance points on the FCC band as shown in Fig. 5.15.

In addition, we consider a relatively high and stable access impedance such as in Fig. 6.1, where a network-switch is connected to the power line, to indicate that the optimization method cannot be applied in this case.

The parameters of the PLC transmitter are also related to the Analog Front End AFE032 of Texas Instrument and conform the FCC-above-CENELEC band [108].

In the simulations, the AWGN channel is chosen for simplification. Real measurements for channel attenuation and noise are considered in (7.3.1). It has been shown that the proposed optimization method increases the transmission data rate.

7.5 Performance Evaluation

First, we determine the limit N_{limit} of the suppressed subcarriers for different modulation schemes. The performance of the optimization method with respect to packet error rate (PER) is then compared to the state of the art transmission.

7.5.1 N_{limit} specification

To specify the allowed number of suppressed subcarriers N_{limit}, we present simulation results for a PLC transmitter and receiver based on the IEEE 1901.2 where the access impedance on the power line is flat (network-switch is connected). The optimization method cannot be applied in this case. However, the subcarriers are suppressed by force to determine the threshold where the transmission and the channel coding fail.

Fig. 7.4 and Fig. 7.5 show the relation between the suppressed subcarriers number, the PER, and the SNR values for DBPSK and DQPSK modulation schemes, respectively. The PER is fixed to 10^{-3} due to the long simulation duration. It can be realized that the PER

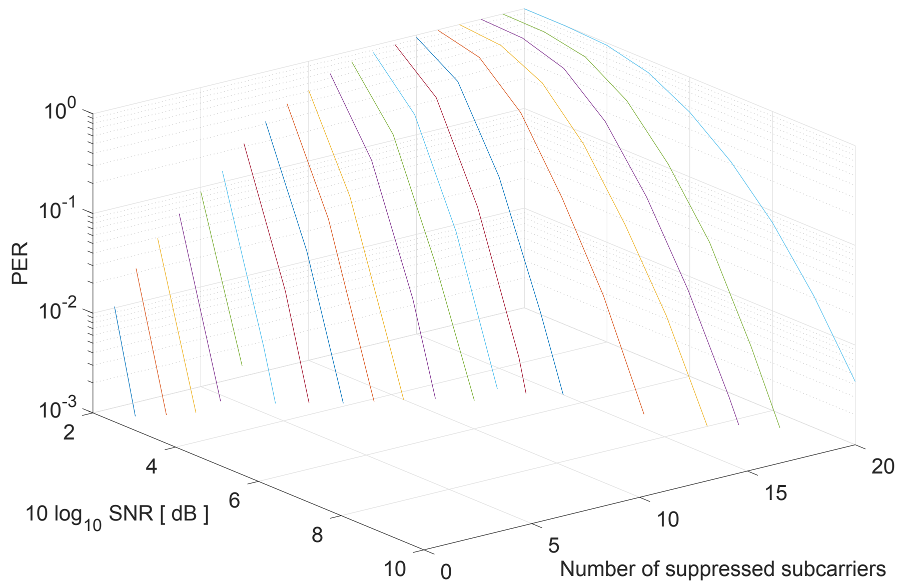

FIGURE 7.4: Determination of N_{limit} for DBPSK modulation [109]

increases extremely from 15-16 suppressed subcarriers for DBPSK and from 12-13 suppressed subcarriers for DQPSK. Therefore, the limited number of suppressed subcarriers N_{limit} for the optimization algorithm is chosen for DBPSK as 16 and for DQPSK as 12. Hence, the optimization method switches off subcarriers as long as $\alpha_i(t) < \alpha_u$ and N_{limit} is not reached.

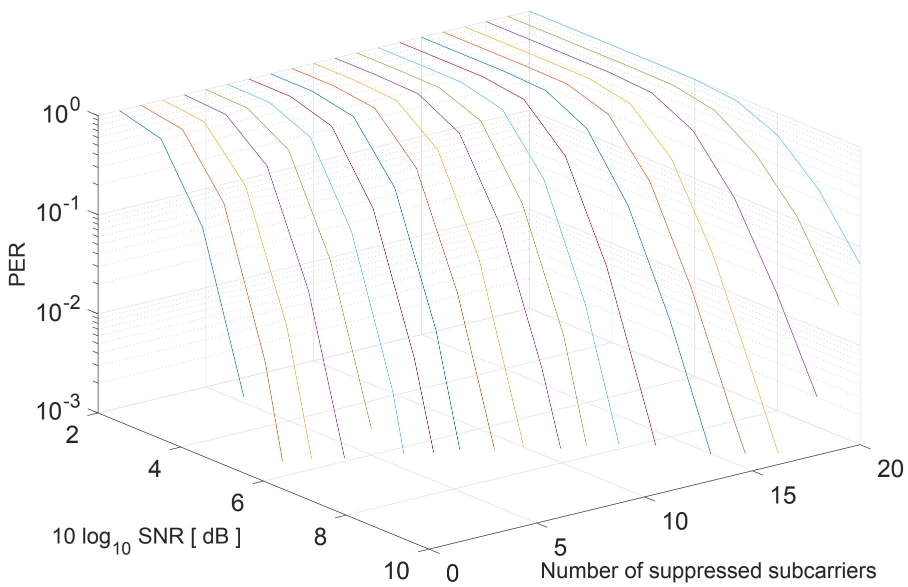

FIGURE 7.5: Determination of N_{limit} for DQPSK modulation [109]

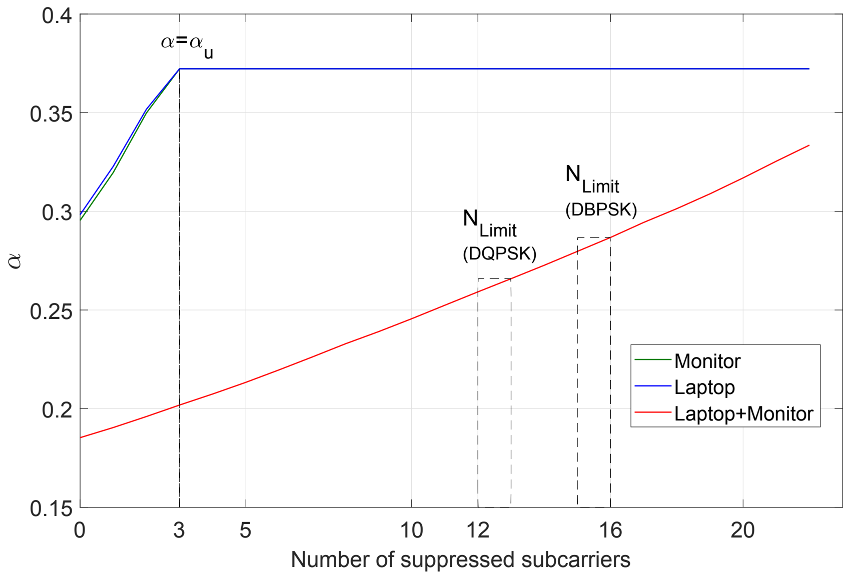

FIGURE 7.6: Suppressed subcarrier vs. α [109]

Fig. 7.6 shows the behavior between the suppressed subcarriers and the multiplication factor α. It has been shown that the factor α reaches α_u by switching off 3 subcarriers for access impedance where a monitor/laptop is connected to the power line. Thereafter, no subcarriers can be suppressed and the optimization method cannot be further applied. For access impedance where both (monitor and laptop) are connected together to the power line, the factor α did not reach α_u and $\alpha = \alpha_i(t)$ even after switching off 22 subcarriers, which is more than N_{limit}. Therefore, the maximum expected gain in this situation will be by suppressing N_{limit} of subcarriers for DBPSK and DQPSK.

7.5.2 Gain evaluation

Fig. 7.7, Fig. 7.8, and Fig. 7.9 present the PER obtained for IEEE 1901.2 over SNR for access impedance measurements where monitor, laptop, and laptop+monitor are connected to the power line, respectively. The simulation results consider two modulation schemes DBPSK and DQPSK. The subcarriers are switched off until the optimization method does not bring any further gain for both schemes. The blue lines represent the transmission in the normal case and the red lines represent the optimized transmission. It has been shown that the optimization method increases the transmission performance with respect to the PER.

To determine the exact gain of the optimization method, we set the PER to 10^{-3} in Fig. 7.7, Fig. 7.8, and Fig. 7.9, and calculate the difference between the normal transmission and the optimized transmission for DBPSK and DQPSK schemes in terms of SNR.

Fig. 7.10 shows the SNR gain with respect to the number of switched off subcarriers for a DBPSK modulation scheme. The simulation results consider access impedance values where different load equipment are connected to the power line. As expected from Fig. 7.6,

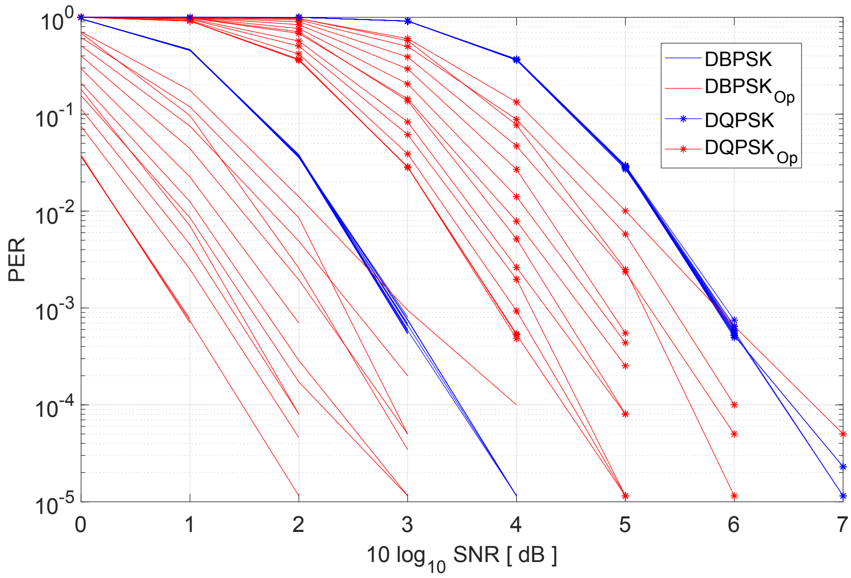

FIGURE 7.7: PER of IEEE 1901.2 for an access impedance where a monitor is connected to the power line [109]

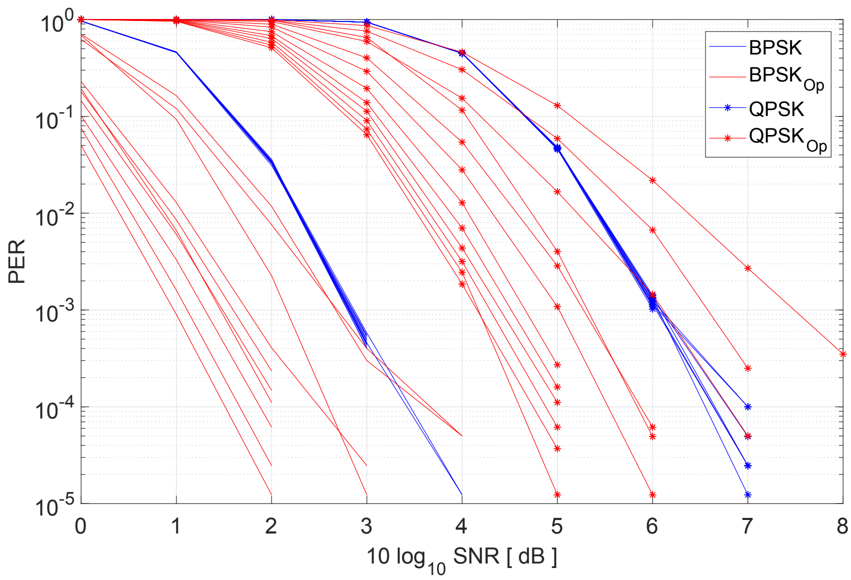

FIGURE 7.8: PER of IEEE 1901.2 for an access impedance where a laptop is connected to the power line

the maximum gain is reached by switching off 3 subcarriers for the access impedance where a monitor/laptop is connected to the power line ($\alpha = \alpha_u$). The achievable gain is equal to 2dB. However, the maximum gain is reached by switching off 16 subcarriers for an access impedance where the monitor and laptop are connected together to the power line (N_{limit} is reached). The achievable gain is equal to 2.4dB.

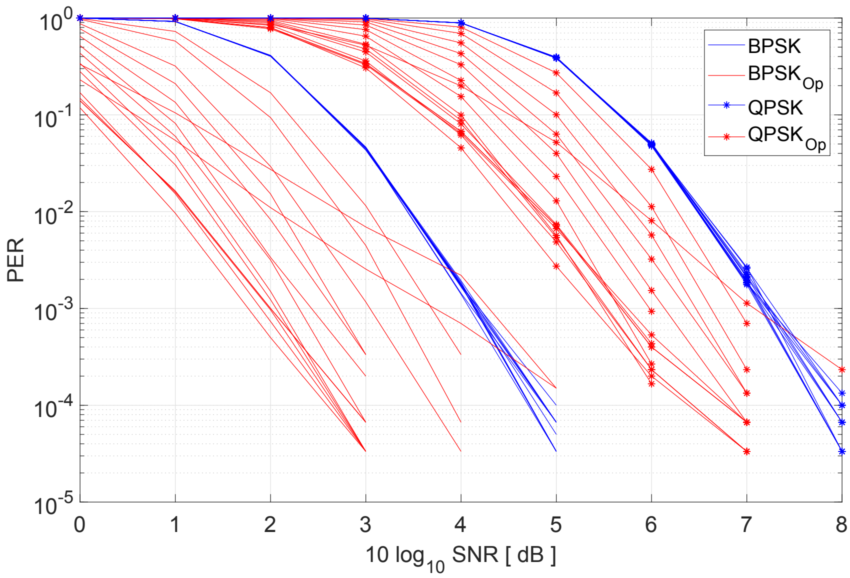

FIGURE 7.9: PER of IEEE 1901.2 for an access impedance where the monitor and laptop are connected to the power line

Also, Fig. 7.11 shows the SNR gain with respect to the number of switched off subcarriers for a DQPSK modulation scheme. It has been shown that the expected maximum gain is reached by switching off 3 subcarriers for an access impedance where a monitor/laptop is connected to the power line ($\alpha = \alpha_u$). The achievable gain is equal to 2dB (Monitor) and 1.85dB (Laptop). The maximum gain is reached by switching off 12 subcarriers where the monitor and laptop are connected together to the power line (N_{limit} is reached). The achievable gain is equal to 1.87dB.

The presented simulation results verify the subcarriers suppression algorithm where the maximum gain can only be achieved when $\alpha = \alpha_u$ or the allowed number of suppressed subcarriers N_{limit} is reached.

7.5.3 Signals evaluation

The influence of the optimization method on the transmitted signal and the current at the transmitter side is evaluated here. The voltage $u_{tx}(t)$ and the current $i_{in}(t)$ are modeled based on the method presented in Chapter 6. Fig. 7.12 shows the voltage $u_{tx}(t)$ at the transmitter side in the case of the normal and the optimized transmission for the different access impedance values. The switched off subcarrier numbers are chosen with respect to the

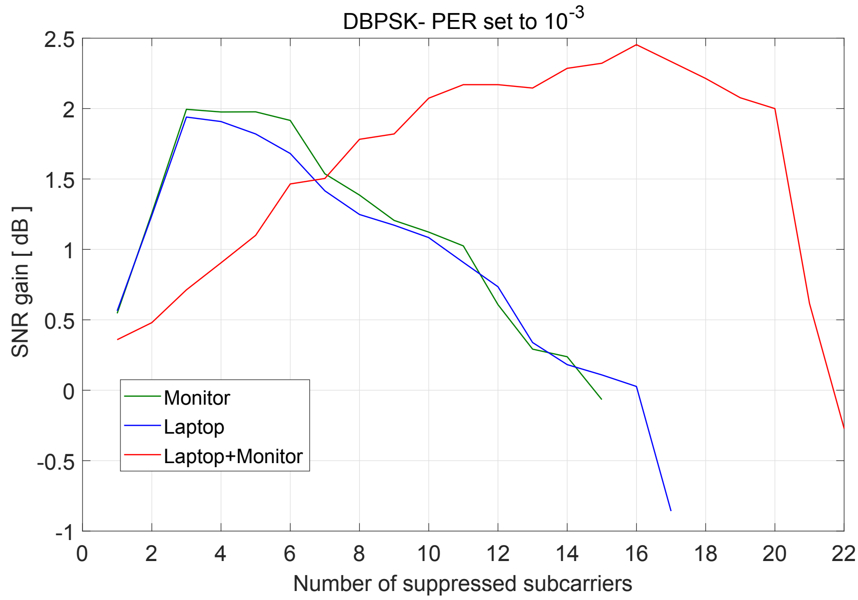

FIGURE 7.10: SNR gain of IEEE 1901.2 for DBPSK scheme [109]

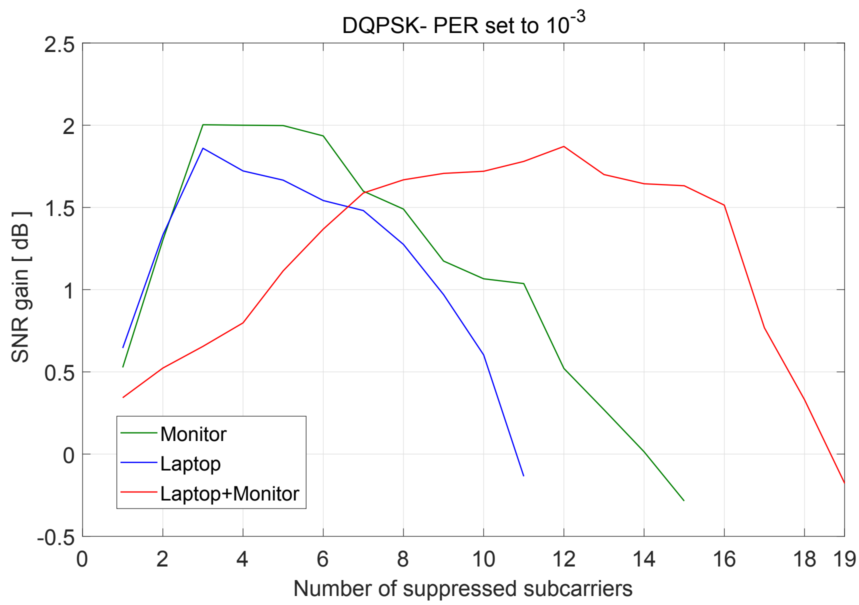

FIGURE 7.11: SNR gain of IEEE 1901.2 for DQPSK scheme [109]

TABLE 7.4: Effective voltage at the transmitter side

	RMS U_{tx} [dBµV]			
	Switch	**Monitor**	**Laptop**	**Lap+Moni**
DBPSK	133.3	123.8	124.3	119.2
DBPSK$_{Op}$	133.3	125.7	126.4	123.1
DQPSK	133.5	123.9	124.7	119.3
DBPSK$_{Op}$	133.5	125.7	126.8	122.7

maximum gain for each access impedance value in the case of a DBPSK modulation scheme. The preamble signal is used for the evaluation. The reason is that the generated symbols are chirp signals. These chirp signals have special properties in OFDM systems that allow us to analyze the resulted voltage and current. In particular, they show the improvement on the voltage and current signals by the low access impedances at the time domain. The data frames can be equivalently evaluated.

The complete transmitted signal is shown only for the case where the network-switch is connected to the power line. The voltage $u_{tx}(t)$ remains constant and the optimization method is not applied in this case. For other access impedance values, we zoomed-in three symbols of the preamble in the plots for a better representation. The voltage decreases for low impedance values as shown in the preamble symbols. The chirp signals shape behaves correspondingly to the access impedance curves. It has been shown that the switched off subcarriers positions are related to the low impedance value. The optimized signal voltage level is increased compared to the normal transmission.

Table 7.4 describes the effective voltage (RMS) U_{tx} in [dBµV] at the output of the transmitter for the normal and optimized transmission. The simulation results consider different access impedance values and modulation schemes. The effective voltage at the output of the transmitter conforms the level of (134 dBµV) where the access impedance value is high. The effective voltage level is decreased where the access impedance values are low. It reaches 119.2 dBµV in the worst case where the monitor and laptop are connected together to the power line. The effective voltage level is increased by 2-3 dBµV in the optimized transmission.

Also, Fig. 7.12 shows the corresponding current $i_{in}(t)$ to the voltage signal $u_{tx}(t)$ at the transmitter side in the case of the normal and optimized transmission for the different access impedance values. The current $i_{in}(t)$ is stable below 1.5A in the preamble symbols for high impedance value and the optimization method is not applied in this case. The current increases for low impedance values and is limited to 1.5A RMS value. It has been shown that the switched off subcarrier positions are related to the low impedance values.

7.6 Conclusion

This chapter presents an optimization method to improve the transmitted signal by PLC devices in the case of low access impedances and limited power consumption of transmitters. The optimization method is done by selecting and suppressing the subcarriers with the lowest access impedance and the maximum current which increases automatically the transmitted signal on the other subcarriers. This method based on a greedy algorithm has delivered, in the cases of very low access impedance, a significant gain in the achievable data compared to the state of the art transmission for PRIME technology. An algorithm to determine the allowed number of suppressed subcarriers that deliver the maximum gain without influencing the transmission has been investigated and verified. The PER has been simulated as a performance factor for packets based on the IEEE 1901.2 standard. The PER over SNR has been improved for very low access impedances by 2.4dB and 2dB as a maximum for DBPSK and DQPSK schemes, respectively. The transmitted signal and the flowing current at the transmitter side are also improved in the case of low access impedances compared to the state of the art transmission.

The presented optimization algorithms can be combined with most PLC standardization since the modification on the transmitted signal caused by the PLC channel behavior is only applied on the transmitter side and no hardware adaptation is required.

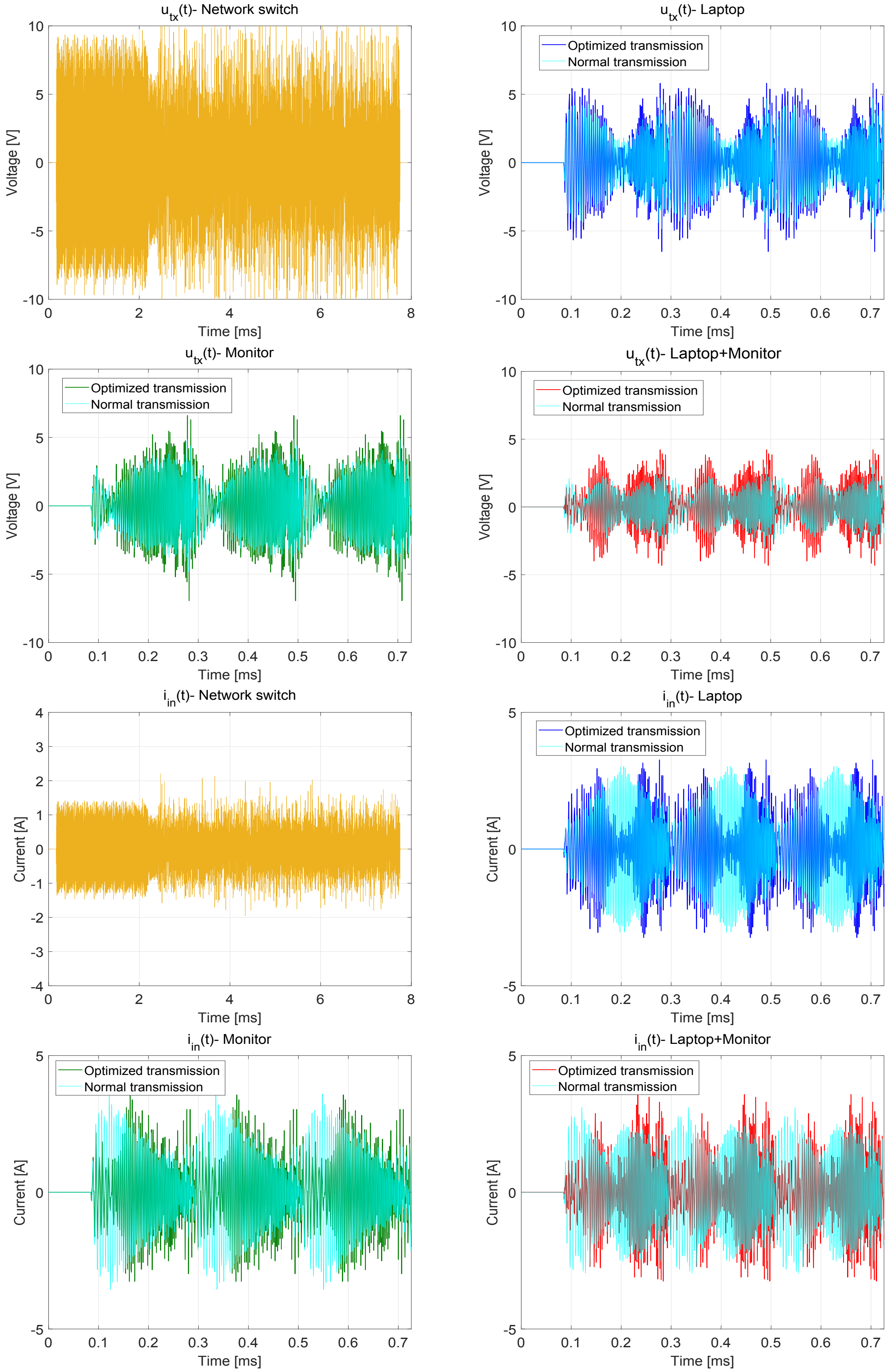

FIGURE 7.12: The voltage $u_{tx}(t)$ and the current $i_{in}(t)$ of preamble symbols in case of the normal and optimized transmission for different impedances [109]

Chapter 8

Conclusions

For the proper design of NB-PLC systems, good knowledge of the grid characteristics in terms of load and access impedances is required. In this respect, experimental measurement campaigns were performed in several scenarios where PLC can be applied. In this work, a comprehensive overview of the power line channel access impedance in narrowband frequencies and its influence on the data transmission over power lines from a telecommunications point of view was presented. This investigation also led to an optimization method for improving the performance of NB-PLC systems in the case of low access impedance on the power grid. This chapter reports our contributions in this thesis in three main parts and suggests possible directions for future work.

8.1 Contributions Related to NB-PLC Access Impedance

The impact of power line access impedance on the performance of NB-PLC systems was analyzed and examined. First, the essential basis for investigating the effects of the access impedance on NB-PLC systems was provided. A behavioral model of the PLC channel with respect to a linear time-variant system extended from a linear time-invariant system was presented. The communication scenario between transmitter and receiver over the NB-PLC channel was discussed. It has been shown that the low access impedance caused by an unmatched load on the power grid reduces the power amplifier output level of PLC modems and the transmitted signals. Furthermore, the achievable data rate by PLC transmitters was mathematically investigated under the condition of power consumption limitations. For the simulation parameters, the PRIME standard was taken as an example, while the transmitter circuit was related to AFE031 of Texas Instruments. It has been found that the achievable data rate was reduced by 55-90% for the low access impedances compared to the assumed impedance by the EN 50065-1 standard.

In addition, the coexistence problem caused by changing the impedance values of smart grid applications between transmitting and receiving was presented. A typical transmission scenario of two different applications on the CENELEC bands based on LTspice simulation was proposed. It has been shown that the transmitted signal is attenuated and absorbed before reaching the receiver because of the changed impedance value. The EN 50065-7:2002 standard was presented as a possible solution for overcoming the changeable impedance with its implementation difficulties caused by the frequency selective impedance and the high cost. It has been found that the allocation of various PLC applications to different wires introduces possibilities for solving the transmission problem when different transmitters transmit on the same wire. These contributions were mainly reported in Chapters 2 and 3.

8.2 Contributions Related to Access and Load Impedance Measurements

An accurate access impedance measurement system in the frequency range of 30-500 kHz was developed to analyze and examine the impedance behavior with respect to time and frequency on the power grid. The measurement system is based on direct voltage-current measurement to determine the access impedance of the power line. The digital signal processing was applied in order to completely cancel out the mains frequency component and the synchronization to the zero-crossings. In order to remove all parasitic effects that may disturb the measurements, various calibration setups were compared and selected the most precise setup. This measurement system was able to measure low impedances with an error of less than 1%. Access impedance measurements were performed on different power outlets at the university laboratory and showed the variable characteristics of the network impedance caused by the connected load devices. The access impedance was experimentally proved that is time-variant and very low in some cases, below 0.3Ω at the resonance point, at the CENELEC and FCC bands.

Furthermore, a load impedance measurement procedure at narrowband frequencies based on the access impedance measurement system was presented. The impedance of the load equipment was separated from the impedance of the power grid using an isolation transformer, due to its high impedance. A measurement campaign was performed on a set of devices that can be found in a typical house or laboratory, i.e., a number of home appliances and laboratory equipment. Interestingly, it has been observed that the impedance behavior of each device varies on the power grid; some devices have time-variant impedance, while others have time-invariant impedance. It has been realized that the cause of the impedance time variations is simply due to the switched-mode power supply unit of these devices. Moreover, the deployment of EMI filters significantly reduces the impedance at specific frequencies. Finally, the measured load and access impedances were evaluated and verified according to their time/frequency characteristics. These contributions were mainly reported in Chapters 4 and 5.

8.3 Contributions Related to NB-PLC System Optimization

Modeling of the output voltage and current of PLC devices was presented with respect to the measured time- and frequency-variant access impedances on the power line. The aim was to allow NB-PLC systems to be improved. The modeling method is based on the impulse response of RLC filters that simulate the behavior of the measured access impedances. A mechanism for analyzing the time-variant voltage and current at specific time slots was proposed. The investigated voltage and current models were evaluated and verified using simulation results based on the IEEE 1901.2. The influence of the measured low access impedances on the signal transmitted by and the current flowing through PLC devices was shown with respect to the time. It has been found that the transmitted signal reached the limit defined in the EN 50065-1 standard in the case of relatively high impedance values, whereas it decreased in the case of low access impedances. The current flowing at the transmitter increased corresponding to the low access impedances as well.

Finally, an optimization method was presented for improving the signal transmitted by PLC devices in the case of low access impedances and limited power consumption of the transmitters. The optimization method works by selecting and suppressing the subcarriers with the lowest access impedance and the maximum current, which automatically strengthens the signal transmitted on the other subcarriers. It has been found that this optimization method based on a greedy algorithm delivered a significant gain in the achievable data compared to the state of the art transmission for the PRIME technology. Moreover, an algorithm to determine the allowed number of suppressed subcarriers that deliver maximum benefit without influencing the transmission and the channel coding was developed and verified. In order to show the applicability of the optimization method to other NB-PLC standards, the PER as a performance factor for packets based on the IEEE 1901.2 standard was simulated. It has been found that the PER over SNR improved for very low access impedances by 2.4dB and 2dB as a maximum for DBPSK and DQPSK schemes, respectively. It has been also shown how the transmitted signal increased in the case of the optimized transmission compared to the state of the art. These contributions were mainly reported in Chapters 6 and 7.

8.4 Future Perspectives

As a final comment, some future perspectives were shown, which could represent further research topics. First of all, it would be interesting to extend the available PLC modems in order to be able to get information about their channel access impedance, which would enable the full implementation of the optimization method presented in Chapter 7 in practical systems. Second, due to safety issues, all impedance measurements presented in this work were performed in a laboratory. Therefore, it would be worth developing the presented access impedance measurement system further to enable it to be used for field measurements. Finally, it would also be interesting to propose a classification as well as impedance profiles of the measured load equipment according to their time and frequency characteristics, which would allow predicting the connected loads to the power gird without prior knowledge. Hence, more load impedance measurements would need to be performed in the field on representative equipment. Based on this classification, it would be possible to analyze the PLC channel response as well as the power grid status better.

Appendix A

AIMS Calibration Setup

A.1 AIMS Calibration Point

The access and load impedance measurements using the AIMS have different calibration points. The calibration point means where we connect the calibration resistors to the measurement system, which has an influence on the accuracy of the measurement results.

We use for the access and load impedance measurement setups, a measurement adapter VOLTCRAFT SMA-10, where the output of the AIMS is connected to it. The output of the measurement adapter is connected to the power outlet in the case of an access impedance measurement and is connected to the output of the isolation transformer in the case of an equipment impedance measurement as shown in Fig. A.1 and Fig. A.2, respectively.

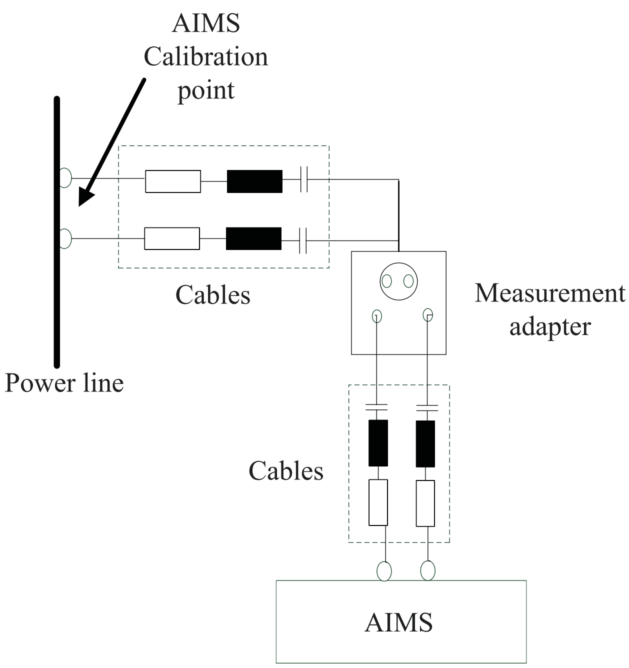

FIGURE A.1: Access impedance measurement- calibration point

Fig. A.1 shows the AIMS calibration point for the access impedance measurement setup. It has been shown that the calibration point has to be at the output of the measurement

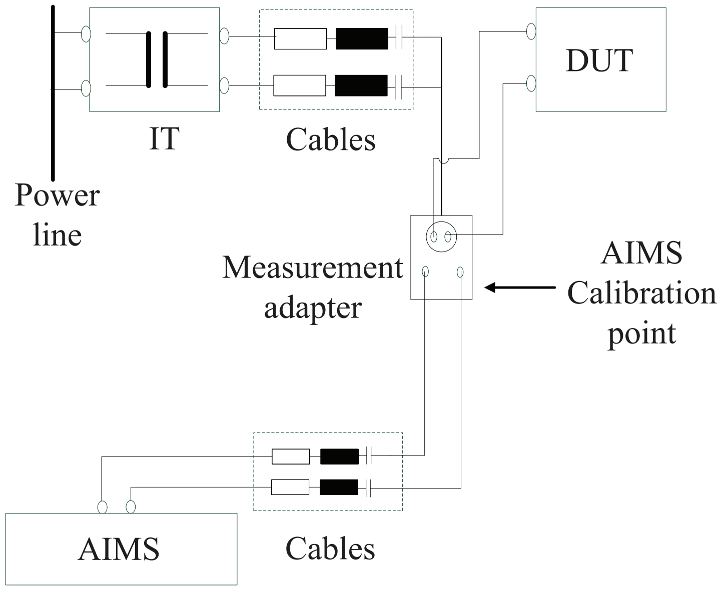

FIGURE A.2: Equipment impedance measurement- calibration point

adapter that is connected to the power outlet, which takes into account the parasitic effects of the adapter cables.

Fig. A.2 shows the AIMS calibration point for the equipment impedance measurement setup. It has been shown that the calibration resistors are connected to the input of the measurement adapter where the measured equipment are later plugged-in. This calibration setup allows the separation of the isolation transformer impedance from the equipment impedance.

A.2 Influence of the Measurement Setup on the Calibration

We aim to highlight the influence of the measurement cables lay setup on the calibration accuracy. To do so, the AIMS is calibrated using the calibration method (H_1 & H_{10} & H_∞). Then, three offline measurements are executed for different resistors with defined cables lay setup. After that, three measurements are executed for the same resistors with changed cable lay setup. Fig. A.3 shows that the three measurements, after changing the cables lay setup, cannot deliver accurate results anymore although they have the same calibration. Therefore, the AIMS has to be always calibrated at the measurement point and under defined setup because any changes in the measurement cables will disturb the results and the calibration.

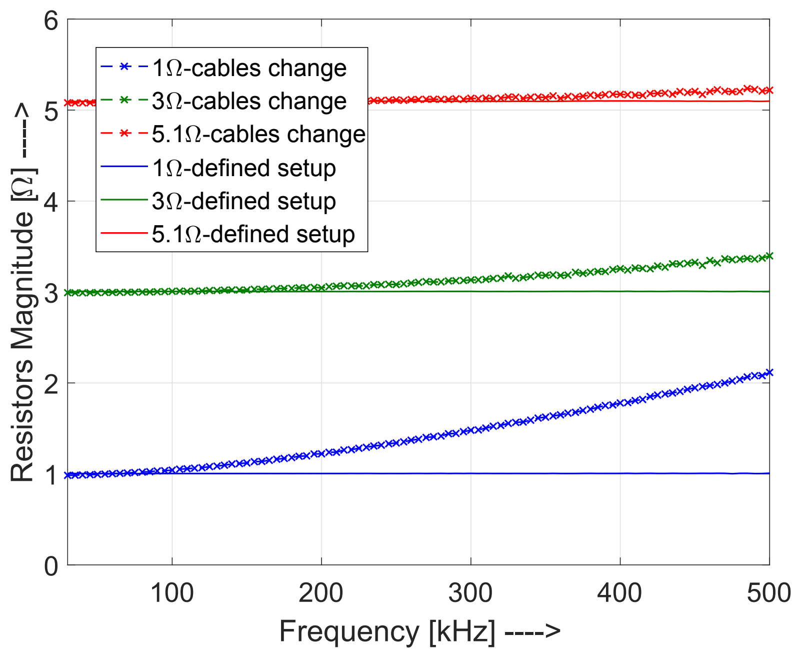

FIGURE A.3: Measurement cables lay setup errors [87]

Appendix B

Comparison Between Isolation Transformer Types

We compare different available isolation transformer types to determine the highest impedance between them. As isolation transformer types, we consider the VOLTCRAFT IT-1500, VOLTCRAFT VIT 1000 with regulation area 1-250 V/AC [111], and Thalheimer LTS 604-K with regulation area 2-250 V/AC [112].

Fig. B.1 shows the impedance of the VOLTCRAFT VIT 1000 and the Thalheimer LTS 604 with regulation output of 230 V/AC. The impedance of these two isolation transformer is lower than the presented impedance of VOLTCRAFT IT-1500 in Fig. 5.4.

Furthermore, we change the output regulation of the VOLTCRAFT VIT 1000 to 150 V/AC and 100 V/AC, respectively, and measure its impedance on the power line. Fig. B.2 shows that the impedance has been increased (2.2KΩ at the resonance point) compared to the case of regulation output of 230 V/AC. However, this regulation areas (100-150 V/AC) can not be used for the in stock available equipment.

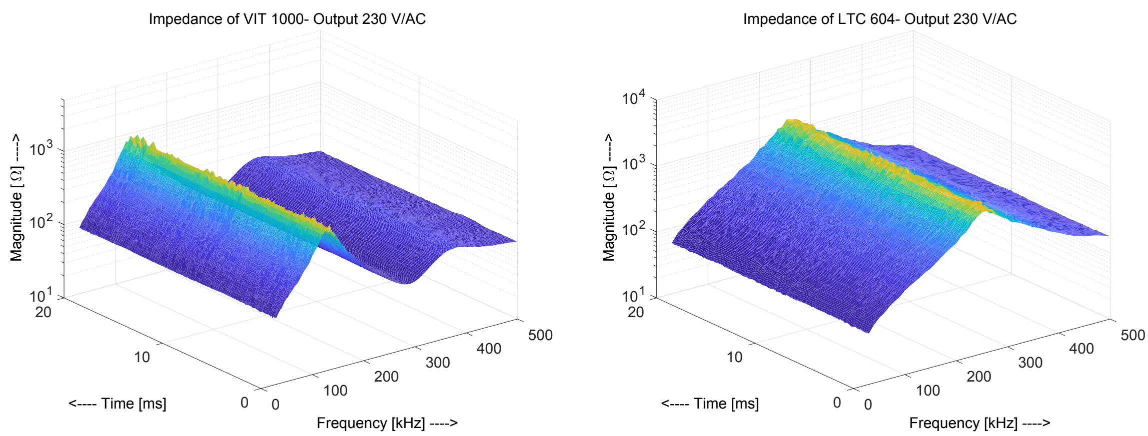

FIGURE B.1: Impedance comparison between different isolation transformer types

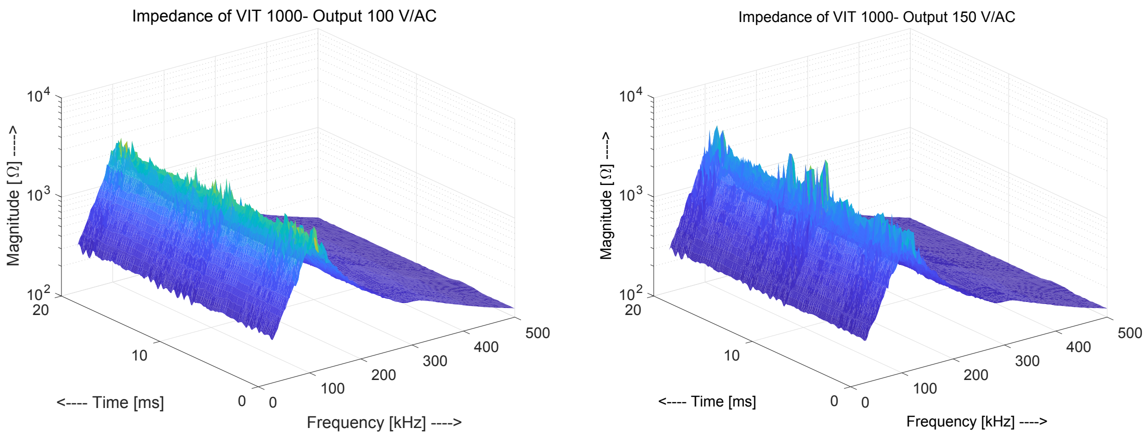

Figure B.2: Impedance of VOLTCRAFT VIT 1000 with different output ranges

Bibliography

[1] M. Schwartz, “Carrier-wave telephony over power lines: Early history [history of communications]”, *IEEE Communications Magazine*, vol. 47, no. 1, pp. 14–18, 2009.

[2] H. C. Ferreira, L. Lampe, J. Newbury, and T. G. Swart, *Power line communications: theory and applications for narrowband and broadband communications over power lines*. John Wiley & Sons, 2011.

[3] S. Galli, A. Scaglione, and Z. Wang, “For the grid and through the grid: The role of power line communications in the smart grid”, *Proceedings of the IEEE*, vol. 99, no. 6, pp. 998–1027, 2011.

[4] D. E. Nordell, “Communication systems for distribution automation”, in *Transmission and Distribution Conference and Exposition, 2008. T&D. IEEE-PES*, IEEE, 2008, pp. 1–14.

[5] S. T. Mak and D. L. Reed, “TWACS, a new viable two-way automatic communication system for distribution networks. Part I: Outbound communication”, *IEEE Transactions on Power Apparatus and systems*, no. 8, pp. 2941–2949, 1982.

[6] S. T. Mak and T. G. Moore, “TWACS, A New viable two-way automatic communication system for distribution networks. Part II: Inbound Communication”, *IEEE transactions on power apparatus and systems*, no. 8, 1984.

[7] D. Dzung, I. Berganza, and A. Sendin, “Evolution of powerline communications for smart distribution: From ripple control to OFDM”, in *Power Line Communications and Its Applications (ISPLC), 2011 IEEE International Symposium on*, IEEE, 2011, pp. 474–478.

[8] EN50065-1, “Signalling on low-voltage electrical installations in the frequency range 3 kHz to 148.5 kHz: General requirements, frequency bands and electromagnetic disturbances”, 2011. [Online]. Available: www.cenelec.eu.

[9] FCC, “Federal communications commission (FCC) rules and regulations regarding unlicensed transmissions”, *Title 47 CFR Part 15*, Nov. 2017. [Online]. Available: www.fcc.gov/wireless/bureau-divisions/technologies-systems-and-innovation-division/rules-regulations-title-47.

[10] ARIB, “Association of radio industries and businesses (ARIB), "power line communication equipment (10kHz-450kHz)"”, *sTD-T84, Ver. 1.0*, Nov. 2002. [Online]. Available: www.arib.or.jp/english/.

[11] S. Galli and O. Logvinov, “Recent developments in the standardization of power line communications within the IEEE”, *IEEE Communications Magazine*, vol. 46, no. 7, 2008.

[12] A Sanz, P. Pinero, J. Idiago, S Esteban, and J. Garcia, “Narrowband power line communications evaluation in complex distribution networks”, in *Smart Grid Communications (SmartGridComm), 2014 IEEE International Conference on*, IEEE, 2014, pp. 266–271.

[13] C. R. Paul, *Introduction to electromagnetic compatibility*. John Wiley & Sons, 2006, vol. 184.

[14] M. Sigle and W. Liu, “On the impedance of the low-voltage distribution grid at frequencies up to 500 kHz”, in *Power Line Communications and Its Applications (ISPLC), 2012 16th IEEE International Symposium on*, IEEE, 2012, pp. 30–34.

[15] ETSI, “Power line telecommunications (PLT) narrow band transceivers in the range 9 kHz to 500 kHz power line performance test method guide”, *TS 103 909 - V1.1.1*, December 2012. [Online]. Available: www.etsi.org/deliver/etsi_ts/103900_103999/103909/01.01.01_60/ts_103909v010101p.pdf.

[16] G. Hallak, G. Bumiller, and C. Nieß, “Measurement setup for notch evaluation of narrowband plc devices”, in *Global Communications Conference (GLOBECOM), 2017 IEEE*, IEEE, 2017.

[17] D. Liu, E Flint, B Gaucher, and Y Kwark, “Wide band AC power line characterization”, *IEEE Transactions on Consumer Electronics*, vol. 45, no. 4, pp. 1087–1097, 1999.

[18] F. C. Corripio, L. D. del Río, and J. E. Munoz, “A time variant model for indoor power-line channels”, in *Proceedings of the International Symposium on Power Line Communications (ISPLC’01)*, 2001, pp. 85–90.

[19] I. H. Cavdar, “Performance analysis of FSK power line communications systems over the time-varying channels: Measurements and modeling”, *IEEE Transactions on Power delivery*, vol. 19, no. 1, pp. 111–117, 2004.

[20] F. C. Corripio, J. A. C. Arrabal, L. D. Del Río, and J. E. Munoz, “Analysis of the cyclic short-term variation of indoor power line channels”, *IEEE Journal on Selected Areas in Communications*, vol. 24, no. 7, pp. 1327–1338, 2006.

[21] S. Barmada, A. Musolino, and M. Raugi, “Innovative model for time-varying power line communication channel response evaluation”, *IEEE journal on selected areas in communications*, vol. 24, no. 7, pp. 1317–1326, 2006.

[22] M. Nassar, A. Dabak, I. H. Kim, T. Pande, and B. L. Evans, “Cyclostationary noise modeling in narrowband powerline communication for smart grid applications”, in *Acoustics, Speech and Signal Processing (ICASSP), 2012 IEEE International Conference on*, IEEE, 2012, pp. 3089–3092.

[23] J. A. Cortés, L. Diez, F. J. Canete, and J. J. Sanchez-Martinez, "Analysis of the indoor broadband power-line noise scenario", *IEEE Transactions on electromagnetic compatibility*, vol. 52, no. 4, pp. 849–858, 2010.

[24] Y. Hirayama, H. Okada, T. Yamazato, and M. Katayama, "Noise analysis on wide-band PLC with high sampling rate and long observation time", 2003.

[25] G. Chu, J. Li, and W. Liu, "Narrow band power line channel characteristics for low voltage access network in China", in *Power Line Communications and Its Applications (ISPLC), 2013 17th IEEE International Symposium on*, IEEE, 2013, pp. 297–302.

[26] O. G. Hooijen, "On the relation between network-topology and power line signal attenuation", in *ISPLC*, vol. 98, 1998, pp. 24–26.

[27] T. Banwell and S. Galli, "A new approach to the modeling of the transfer function of the power line channel", in *Proceedings of the 5th International Symposium on Power-Line Communications and its Applications (ISPLC)*, 2001, pp. 4–6.

[28] M. Bauer, W. Liu, and K. Dostert, "Channel emulation of low-speed PLC transmission channels", in *Power Line Communications and Its Applications, 2009. ISPLC 2009. IEEE International Symposium on*, IEEE, 2009, pp. 267–272.

[29] W. Liu, *Emulation of narrowband powerline data transmission channels and evaluation of PLC systems*. KIT Scientific Publishing, 2013, vol. 7.

[30] C. J. Kikkert, "An on-line plc frequency impedance analyzer", in *Smart Grid Communications (SmartGridComm), 2013 IEEE International Conference on*, IEEE, 2013, pp. 606–611.

[31] N. Pavlidou, A. H. Vinck, J. Yazdani, and B. Honary, "Power line communications: State of the art and future trends", *IEEE Communications magazine*, vol. 41, no. 4, pp. 34–40, 2003.

[32] A. Mengi, "On combined coding and modulation", PhD thesis, Universität Duisburg-Essen, Fakultät für Ingenieurwissenschaften» Informatik und Angewandte Kognitionswissenschaft» Informatik» Mathematische Methoden der Datenübertragung, 2010.

[33] C. Cano, A. Pittolo, D. Malone, L. Lampe, A. M. Tonello, and A. G. Dabak, "State of the art in power line communications: From the applications to the medium", *IEEE Journal on Selected Areas in Communications*, vol. 34, no. 7, pp. 1935–1952, 2016.

[34] F. Canete, J. Cortes, L Diez, J. Entrambasaguas, and J. Carmona, "Fundamentals of the cyclic short-time variation of indoor power-line channels", in *Power line communications and its applications, 2005 international symposium on*, IEEE, 2005, pp. 157–161.

[35] S. Galli and T. C. Banwell, "A deterministic frequency-domain model for the indoor power line transfer function", *IEEE Journal on Selected Areas in Communications*, vol. 24, no. 7, pp. 1304–1316, 2006.

[36] T. Sartenaer and P. Delogne, "Deterministic modeling of the (shielded) outdoor power line channel based on the multiconductor transmission line equations", *IEEE Journal on Selected areas in Communications*, vol. 24, no. 7, pp. 1277–1291, 2006.

[37] A. M. Tonello and F. Versolatto, "Bottom-up statistical PLC channel modeling—part i: Random topology model and efficient transfer function computation", *IEEE Transactions on Power Delivery*, vol. 26, no. 2, pp. 891–898, 2011.

[38] ——, "Bottom-up statistical PLC channel modeling—part ii: Inferring the statistics", *IEEE Transactions on Power Delivery*, vol. 25, no. 4, pp. 2356–2363, 2010.

[39] F. J. Canete, L. Diez, J. A. Cortes, and J. T. Entrambasaguas, "Broadband modelling of indoor power-line channels", *IEEE Transactions on Consumer Electronics*, vol. 48, no. 1, pp. 175–183, 2002.

[40] T. Esmailian, F. R. Kschischang, and P Glenn Gulak, "In-building power lines as high-speed communication channels: Channel characterization and a test channel ensemble", *International Journal of Communication Systems*, vol. 16, no. 5, pp. 381–400, 2003.

[41] A. M. Tonello, F. Versolatto, B. Béjar, and S. Zazo, "A fitting algorithm for random modeling the plc channel", *IEEE Transactions on Power Delivery*, vol. 27, no. 3, pp. 1477–1484, 2012.

[42] S. Galli, "A simplified model for the indoor power line channel", in *Power Line Communications and Its Applications, 2009. ISPLC 2009. IEEE International Symposium on*, IEEE, 2009, pp. 13–19.

[43] ——, "A novel approach to the statistical modeling of wireline channels", *IEEE Transactions on Communications*, vol. 59, no. 5, pp. 1332–1345, 2011.

[44] Y. Xiaoxian, Z. Tao, Z. Baohui, Y. Fengchun, D. Jiandong, and S. Minghui, "Research of impedance characteristics for medium-voltage power networks", *IEEE Transactions on Power Delivery*, vol. 22, no. 2, pp. 870–878, 2007.

[45] M. Raugi, T. Zheng, M. Tucci, and S. Barmada, "On the time invariance of PLC channels in complex power networks", in *Power Line Communications and Its Applications (ISPLC), 2010 IEEE International Symposium on*, IEEE, 2010, pp. 56–61.

[46] F. Versolatto, A. M. Tonello, C. Tornelli, and D. Della Giustina, "Statistical analysis of broadband underground medium voltage channels for plc applications", in *Smart Grid Communications (SmartGridComm), 2014 IEEE International Conference on*, IEEE, 2014, pp. 493–498.

[47] A. Cataliotti, D. Di Cara, R. Fiorelli, and G. Tine, "Power-line communication in medium-voltage system: Simulation model and onfield experimental tests", *IEEE transactions on power delivery*, vol. 27, no. 1, pp. 62–69, 2012.

[48] A. G. Lazaropoulos and P. G. Cottis, "Broadband transmission via underground medium-voltage power lines—part ii: Capacity", *IEEE Transactions on Power Delivery*, vol. 25, no. 4, pp. 2425–2434, 2010.

[49] P. Reynolds and B. Dyner, "Safety aspects of high voltage power line fault location techniques", in *Electrical Insulation Conference, 1973 EIC 11th*, IEEE, 1973, pp. 178–180.

[50] J. Bridges, "The biological significance of power line and high voltage switchyard environments", in *Electromagnetic Compatibility, IEEE 1976 International Symposium on*, IEEE, 1976, pp. 1–7.

[51] J. G. Proakis, *Digital Communications*. McGraw-Hill, 3rd Edition, 1995.

[52] S. P. Davis, M. C. Abrams, and J. W. Brault, *Fourier transform spectrometry*. Academic Press, 2001.

[53] L. Lampe, *Power Line Communications: Principles, Standards and Applications from Multimedia to Smart Grid*. John Wiley & Sons, 2016.

[54] J. Cortes, F. Canete, L Diez, and J. Entrambasaguas, "Characterization of the cyclic short-time variation of indoor power-line channels response", in *Power Line Communications and Its Applications, 2005 International Symposium on*, IEEE, 2005, pp. 326–330.

[55] M. H. Chan and R. W. Donaldson, "Attenuation of communication signals on residential and commercial intrabuilding power-distribution circuits", *IEEE Transactions on Electromagnetic compatibility*, vol. 28, no. 4, pp. 220–230, 1986.

[56] J. Bausch, T. Kistner, M. Babic, and K. Dostert, "Characteristics of indoor power line channels in the frequency range 50-500 kHz", in *Power Line Communications and its Applications, 2006 IEEE International Symposium on*, IEEE, 2006, pp. 86–91.

[57] K. Dostert, M. Zimmermann, T. Waldeck, and M. Arzberger, "Fundamental properties of the low voltage power distribution grid used as a data channel", *Transactions on Emerging Telecommunications Technologies*, vol. 11, no. 3, pp. 297–306, 2000.

[58] V. Degardin, M. Lienard, A. Zeddam, F. Gauthier, and P Degauquel, "Classification and characterization of impulsive noise on indoor powerline used for data communications", *IEEE Transactions on Consumer Electronics*, vol. 48, no. 4, pp. 913–918, 2002.

[59] M. Katayama, T. Yamazato, and H. Okada, "A mathematical model of noise in narrowband power line communication systems", *IEEE Journal on Selected areas in Communications*, vol. 24, no. 7, pp. 1267–1276, 2006.

[60] M. Nassar, K. Gulati, Y. Mortazavi, and B. L. Evans, "Statistical modeling of asynchronous impulsive noise in powerline communication networks", in *Global Telecommunications Conference (GLOBECOM 2011), 2011 IEEE*, IEEE, 2011, pp. 1–6.

[61] M. A. Sonmez and M. Bagriyanik, "Statistical model study for narrowband power line communication noises", in *Electrical and Electronics Engineering (ELECO), 2013 8th International Conference on*, IEEE, 2013, pp. 539–543.

[62] O. G. Hooijen, "A channel model for the residential power circuit used as a digital communications medium", *IEEE transactions on electromagnetic compatibility*, vol. 40, no. 4, pp. 331–336, 1998.

[63] T. Claasen and W Mecklenbrauker, "On stationary linear time-varying systems", *IEEE transactions on circuits and systems*, vol. 29, no. 3, pp. 169–184, 1982.

[64] S. Kasturia, J. T. Aslanis, and J. M. Cioffi, "Vector coding for partial response channels", *IEEE transactions on Information Theory*, vol. 36, no. 4, pp. 741–762, 1990.

[65] S Weinstein and P. Ebert, "Data transmission by frequency-division multiplexing using the discrete fourier transform", *IEEE transactions on Communication Technology*, vol. 19, no. 5, pp. 628–634, 1971.

[66] H. Rohling, *OFDM: concepts for future communication systems*. Springer Science & Business Media, 2011.

[67] M. Hoch, "OFDM-verfahren für die schmalbandige datenübertragung im elektrischen energieversorgungsnetz", 2011.

[68] I. S. Association, "IEEE 1901.2-2013 for low-frequency (less than 500 kHz) narrowband power line communications for smart grid applications", *Active Standard IEEE 1901.2-2013*, Dec. 2013. [Online]. Available: www.standards.ieee.org/findstds/standard/1901.2-2013.html.

[69] G Hallak and G Bumiller, "PLC for home and industry automation", *Power Line Communications: Principles, Standards and Applications from Multimedia to Smart Grid*, p. 449, 2016.

[70] J. Burroughs, "X-10® home automation using the PIC16F877A", *Lamp*, vol. 10, no. 10, 2010.

[71] KNX Association, "KNX system specifications", *Tech. Rep.*, 2009. [Online]. Available: www.knx.org.

[72] E. Corporation, "Introduction to the lonworks system", *United States of America*, [Online]. Available: www.echelon.com/support/documentation/manuals/general/078-0183-01A.pdf.

[73] L. Lampe, A. Tonello, and D. Shaver, "Power line communications for automation networks and smart grid [guest editorial]", *IEEE Communications Magazine*, vol. 49, no. 12, pp. 26–27, 2011.

[74] ITU-T, "Narrowband orthogonal frequency division multiplexing power line communication transceivers for itu-t g.hnem networks", *Recommendation G.9902*, Oct. 2012. [Online]. Available: www.itu.int/rec/T-REC-G.9902.

[75] ——, "PRIME specification revision v1.3, specification for powerline intelligent metering evolution", *Recommendation G.9904*, Oct. 2012. [Online]. Available: www.prime-alliance.org.

[76] ——, "Narrowband orthogonal frequency division multiplexing power line communication transceivers for G3-PLC networks", *Recommendation G.9903*, Oct. 2012. [Online]. Available: www.itu.int/rec/T-REC-G.9903.

[77] G. Hallak and G. Bumiller, "Throughput optimization based on access impedance of PLC modems with limited power consumption", in *Global Communications Conference (GLOBECOM), 2014 IEEE*, IEEE, 2014, pp. 2960–2965.

[78] ——, "Data rate optimization on PLC devices with current controller for low access impedance", in *Power Line Communications and its Applications (ISPLC), 2016 International Symposium on*, IEEE, 2016, pp. 144–149.

[79] ——, "Time variant voltage and current modeling corresponding to access impedance measurements", in *Power Line Communications and its Applications (ISPLC), 2018 IEEE International Symposium on*, IEEE, 2018, pp. 1–6.

[80] D. Anastasiadou and T. Antonakopoulos, "Multipath characterization of indoor powerline networks", *IEEE Transactions on Power Delivery*, vol. 20, no. 1, pp. 90–99, 2005.

[81] Texas Intruments, "Power Line Communications Analog Front End AFE031", [Online]. Available: www.ti.com/lit/ds/sbos531d/sbos531d.pdf.

[82] S. AG, "PLC Kanalmessungen am Niederspannungsnetz", in *Internal report from Austria*, 2015.

[83] G. Hallak and G. Bumiller, "Coexistence analysis of impedance modulating transmitters", in *Power Line Communications and Its Applications (ISPLC), 2013 17th IEEE International Symposium on*, IEEE, 2013, pp. 279–284.

[84] K. M. Dostert, "Power lines as high speed data transmission channels-modelling the physical limits", in *Spread Spectrum Techniques and Applications, 1998. Proceedings., 1998 IEEE 5th International Symposium on*, IEEE, vol. 2, 1998, pp. 585–589.

[85] O. Georg, "Elektromagnetische wellen auf leitungen", in *Elektromagnetische Wellen*, Springer, 1997, pp. 155–200.

[86] EN50065-7, "Signalling on low-voltage electrical installations in the frequency range 3 kHz to 148.5 kHz: Equipment impedance", June 2002. [Online]. Available: www.cenelec.eu.

[87] G. Hallak, G. Bumiller, and C. Nieß, "Accurate access impedance measurements on the power line with optimized calibration procedures", in *Instrumentation and Measurement Technology Conference (I2MTC), 2017 IEEE International*, IEEE, 2017, pp. 1–6.

[88] G. Hallak, C. Nieß, and G. Bumiller, "Accurate low access impedance measurements with separated load impedance measurements on the power-line network", *IEEE Transactions on Instrumentation and Measurement*, 2018.

[89] T Fischer, M Albach, and G Schubert, "Accurate impedance characterization with a vector network analyzer", in *Electromagnetic Compatibility and Electromagnetic Ecology, 2007 7th International Symposium on*, IEEE, 2007, pp. 216–219.

[90] F. Passerini and A. M. Tonello, "Analysis of high-frequency impedance measurement techniques for power line network sensing", *IEEE Sensors Journal*, vol. 17, no. 23, pp. 7630–7640, 2017.

[91] P. Technology, "Picoscope 4424", [Online]. Available: www.picotech.com/oscilloscope/4224-4424/picoscope-4224-4424-specifications.

[92] S. D'Alessandro, A. M. Tonello, and L. Lampe, "Adaptive pulse-shaped OFDM with application to in-home power line communications", *Telecommunication Systems*, vol. 51, no. 1, pp. 3–13, 2012.

[93] H. W. Schüßler, *Netzwerke, Signale und Systeme: Theorie kontinuierlicher und diskreter Signale und Systeme*. Springer-Verlag, 2013.

[94] M. Zimmermann, *Energieverteilnetze als Zugangsmedium für Telekommunikationsdienste*. Shaker, 2000.

[95] Omicron-lab, "Bode 100", [Online]. Available: www.omicron-lab.com/bode-100.

[96] M. A. O. Kharraz, P Jensen, V Audebert, A Jeandin, C Lavenu, D Picard, and M Serhir, "Experimental characterization of outdoor low voltage cables for narrowband power line communication", in *Power Line Communications and its Applications (ISPLC), 2016 International Symposium on*, IEEE, 2016, pp. 138–143.

[97] A. Cataliotti, V. Cosentino, D. Di Cara, and G. Tine, "Oil-filled MV/LV power-transformer behavior in narrow-band power-line communication systems", *IEEE Transactions on Instrumentation and Measurement*, vol. 61, no. 10, pp. 2642–2652, 2012.

[98] S Barmada, A Musolino, and M Raugi, "Upper and lower bounds for frequency response of PLC channels in presence of load variations", in *Power Line Communications and Its Applications, 2006 IEEE International Symposium on*, IEEE, 2006, pp. 12–15.

[99] J. Anatory, N. Theethayi, R. Thottappillil, M. Kissaka, and N. H. Mvungi, "The influence of load impedance, line length, and branches on underground cable power-line communications (PLC) systems", *IEEE transactions on power delivery*, vol. 23, no. 1, pp. 180–187, 2008.

[100] D. Hirata, N. Kuwabara, Y. Akiyama, and H. Yamane, "Influence of appliance state on transmission characteristics of indoor ac mains lines in frequency range used power line communication", in *Electromagnetic Compatibility, 2005. EMC 2005. 2005 International Symposium on*, IEEE, vol. 3, 2005, pp. 715–720.

[101] M. Antoniali and A. M. Tonello, "Measurement and characterization of load impedances in home power line grids", *IEEE Transactions on Instrumentation and Measurement*, vol. 63, no. 3, pp. 548–556, 2014.

[102] M. Antoniali, "Experimental activity and analysis of PLC technology in various scenarios", 2013.

[103] L Angrisani, A Baccigalupi, and A Pietrosanto, "A digital signal-processing instrument for impedance measurement", *IEEE transactions on instrumentation and measurement*, vol. 45, no. 6, pp. 930–934, 1996.

[104] I. Yokoshima, "RF impedance measurements by voltage-current detection", *IEEE Transactions on Instrumentation and measurement*, vol. 42, no. 2, pp. 524–527, 1993.

[105] G. Hallak and G. Bumiller, "Impedance measurement of electrical equipment loads on the power line network", in *Power Line Communications and its Applications (ISPLC), 2017 IEEE International Symposium on*, IEEE, 2017, pp. 1–6.

[106] VOLTCRAFT, "VOLTCRAFT IT-1500", [Online]. Available: `www.conrad.de/de/voltcraft-it-1500-universal-labor-trenn-transformator-1500-va-230-vac-trenntrafo-511606`.

[107] Z. Zhang and K. T. Chong, "Comparison between first-order hold with zero-order hold in discretization of input-delay nonlinear systems", in *Control, Automation and Systems, 2007. ICCAS'07. International Conference on*, IEEE, 2007, pp. 2892–2896.

[108] Texas Intruments, "Power Line Communications Analog Front End AFE032", [Online]. Available: `www.ti.com/lit/ds/symlink/afe032.pdf`.

[109] G. Hallak and G. Bumiller, "TX-Signal optimization in current control state of PLC transmitter by low access impedance", in *Power Line Communications and its Applications (ISPLC), 2018 IEEE International Symposium on*, IEEE, 2018, pp. 1–6.

[110] G. Bumiller and L. Lampe, "Fast burst synchronization for PLC systems", in *Power Line Communications and Its Applications, 2007. ISPLC'07. IEEE International Symposium on*, IEEE, 2007, pp. 65–70.

[111] VOLTCRAFT, "VOLTCRAFT VIT 1000 ", [Online]. Available: `www.conrad.de/de/voltcraft-einstellbarer-labor-regel-trenntraformator-vit-1000-1000-va-230-vac-1-250-vac-512767`.

[112] Thalheimer, "Thalheimer LTS 604-K 1000 VA 2 - 250 V/AC", [Online]. Available: `www.conrad.de/de/labor-trenntrafo-einstellbar-thalheimer-lts-604-k-1000-va-2-250-vac-kalibriert-nach-werksstandard-ohne-zertifikat-1195478`.